Diagnostics of Plasma Chemistry in Atmospheric Pressure Plasmas Operated in Humid Feed Gas

Master Thesis

in the
Degree Program
“Master of Science”
in Physics

at the Faculty of Physics and Astronomy
of the Ruhr-Universität Bochum

by

Maike Kai

from
Duisburg

Bochum 2023

Abstract

Atmospheric pressure plasma jets offer the possibility of environmentally friendly hydrogen peroxide production due to their pronounced production of reactive species, which is advantageous in the field of biosynthesis, among others. In this work, the production of hydrogen peroxide (H_2O_2) via the hydroxyl radical (OH) in the gas phase of a helium-fuelled RF atmospheric pressure plasma jet with a dielectric capillary was investigated. For this purpose, temperature measurements, Fourier-transformed infrared spectroscopy (FT-IR) and laser-induced fluorescence (LIF) were conducted. It was found that the gas temperature increases linearly with the plasma power in the range of 1 W to 12 W from $(62 \pm 7)\,^{\circ}\mathrm{C}$ to $(232 \pm 18)\,^{\circ}\mathrm{C}$, independent of low water admixtures. Extrapolation of the temperatures determined in the effluent as well as rotational temperatures of OH determined from optical emission spectra show high agreement. Using spatially resolved LIF, it was shown that the fluorescence in the effluent is not homogeneous, but is broadened along the sheaths. The fluorescence signal decreases exponentially with increasing distance and corresponds in its extension to the dimensions of the capillary of the plasma source. In the centre of the effluent, there is no air near the capillary exit. With increasing distance, the air admixture increases while the total expansion of the gas flow remains constant. At (6400 ± 250) ppm feed gas humidity, 6 W plasma power and 1 slm gas flow rate, an OH density of $1.08 \times 10^{15}\,\mathrm{cm}^{-3}$ was measured by LIF 4 mm from the capillary exit. At a distance of 14 mm, the density is reduced to $3.19 \times 10^{14}\,\mathrm{cm}^{-3}$. H_2O_2 was measured in the far field of the effluent by FT-IR in a multipass cell. A density of $1.38 \times 10^{14}\,\mathrm{cm}^{-3}$ was measured at the same settings. With increasing water admixture up to (6400 ± 250) ppm, the OH density runs into saturation, whereas the H_2O_2 density further increases. An increase in plasma power leads to an increase in OH density and flattening density of H_2O_2. Frequency modulation of the power does not decrease the densities of either species at suitably high duty cycle settings. For low duty cycles, a significant decrease is observed. With increasing gas flow rate, the OH density reaches a plateau above 1 slm. The trends determined in the gas phase show close agreement with measurements carried out in plasma-treated liquids in project B11 of the CRC 1316 and thus indicate a close transfer of the species from gas phase to liquid.

Abstract

Atmosphärendruckplasmajets bieten aufgrund ihrer ausgeprägten Produktion reaktiver Spezies die Möglichkeit einer umweltfreundlichen Wasserstoffperoxidproduktion, die unterer anderem auf dem Gebiet der Biosynthese vorteilhaft ist. In dieser Arbeit wurde die Produktion von Wasserstoffperoxid (H_2O_2) über das Hydroxyl-Radikal (OH) in der Gasphase eines mit Helium betriebenen RF-Atmosphärendruckplasmajets mit dielektrischer Kapillare untersucht. Zu diesem Zweck wurden Temperaturmessungen, Fourier-transformierte Infrarotspektroskopie (FT-IR) und laserinduzierte Fluoreszenz (LIF) durchgeführt. Es wurde ermittelt, dass die Gastemperatur unabhängig von niedrigen Wasserbeimischungen linear mit der Plasmaleistung ansteigt. Extrapolation der im Effluenten ermittelten Temperaturen sowie aus optischen Emissionsspektren bestimmte Rotationstemperaturen weisen eine hohe Übereinstimmung auf. Über ortsaufgelöste LIF wurde gezeigt, dass die Fluoreszenz im Effluenten nicht homogen verläuft, sondern entlang der Randschichten verbreitert ist. Das Fluoreszenzsignal nimmt mit wachsendem Abstand exponentiell ab und entspricht in seiner Ausdehnung den Dimensionen der Kapillare der Plasmaquelle. Im Zentrum des Effluenten befindet sich nahe des Kapillarenausgangs keine Luft. Mit wachsender Distanz erhöht sich die Luftbeimischung bei gleichbleibender Gesamtausdehnung des Gasstroms. Bei (6400 ± 250) ppm Wasserbeimischung, 6 W Plasmaleistung und 1 slm Gasflussrate wurde eine OH-Dichte von $1.08 \times 10^{15}\,\mathrm{cm}^{-3}$ über LIF 4 mm vom Kapillarausgang gemessen. In einem Abstand von 14 mm reduziert sich die Dichte auf $3.19 \times 10^{14}\,\mathrm{cm}^{-3}$. H_2O_2 wurde im Fernfeld des Effluenten mittels FT-IR in einer Multipass-Zelle gemessen. Bei identischen Einstellungen wurde eine Dichte von $1.38 \times 10^{14}\,\mathrm{cm}^{-3}$ gemessen. Mit steigender Wasserbeimischung bis (6400 ± 250) ppm läuft die OH-Dichte in eine Sättigung, wohingegen die H_2O_2-Dichte weiter ansteigt. Eine Erhöhung der Plasmaleistung führt zu einem Anstieg der OH-Dichte und abflachender Dichte von H_2O_2. Frequenzmodulierung der Leistung verringert bei geeignet langen Zykluseinstellungen nicht die Dichten beider Spezies. Bei niedrigen Zyklen wird ein deutlicher Rückgang beobachtet. Mit zunehmender Gasflussrate erreicht die OH-Dichte ein Plateau oberhalb von 1 slm. Die in der Gasphase ermittelten Trends zeigen eine enge Übereinstimmung mit Messungen in plasmabehandelten Flüssigkeiten, die in Projekt B11 des SFB 1316 durchgeführt wurden, und weisen somit auf eine enge Übertragung der Spezies von Gasphase in die Flüssigkeit hin.

Contents

1. Introduction

Atmospheric pressure plasmas are an effective tool in a wide range of applications. Promising results have been reported in healthcare [1–6] and alteration of material surfaces by surface treatments and modifications [7–11]. In addition, atmospheric pressure plasmas contribute significantly to environmental [12–14] as well as chemical applications and biochemistry [15–17].

Within the field of plasma chemistry of atmospheric pressure plasmas, the influence of water has been studied by several research groups [18–20]. Water-containing discharges produce a variety of reactive species such as oxygen (O), hydroxyl radicals (OH) and hydrogen peroxide (H_2O_2) that are crucial for many applications [21]. The latter one is of special interest as it is an important oxidant due to its highly active oxygen content [22]. Thus, H_2O_2 is a sustainable alternative to industrial oxidants, as it only produces water as a by-product of oxidising reactions [21, 23].

The production and loss processes of H_2O_2 still lack understanding and quantitative explanation as the production efficiency is highly dependent on the discharge character and reactor geometry [19]. Low gas temperatures, known residence time and homogeneous discharge behaviour are key factors of the discharge design which facilitate the investigation of the plasma chemistry [19]. Extensive research has been performed over the last years by models [24, 25], experiments [26–28] and their combination [19, 29–31].

The setup used in this work has been designed based on the COST reference jet by the European Cooperation in Science and Technology [32]. It has been shown that the discharge produced by the COST-jet is both stable and reproducible but is limited in its parameters. The COST-jet can only be operated at low input powers as arching sets in at higher input powers which is harmful to the device. By utilising a capillary between the electrodes, the range of plasma power is significantly increased and therefore offers higher variability for application [33].

This work is embedded in project B11 of the SFB 1316 which is stationed within the field of biocatalysis. The project aims at creating a stable, controllable design for a sustainable and resource-efficient biological and chemical synthesis. To achieve this target, a capillary plasma source has been designed and constructed to investigate a large range of operating parameters. This enhances the development of a deeper understanding and therefore reasonable improvement of the

capillary jet to achieve the best results for biological and chemical synthesis.

An interdisciplinary collaboration between biotechnology, computational plasma science and experimental plasma science enables direct comparisons of the different perspectives on the jet and encourages a comprehensive characterisation of the device. Within the group of plasma physics, the focus has previously been on the investigation of the effects of the plasma treatment on liquids [34–36] and sheath effects and electron densities within the plasma [37].

This thesis lays its focus on selected chemical reaction partners within the gas phase. As the effluent is in direct contact with the liquid, understanding the system with regard to the effluent is crucial to gain a comprehensive overview of the processes in the plasma-driven biocatalysis system.

Measurements of the OH density can be performed by various diagnostics. While UV absorption [38] and ring-down spectroscopy [39] have shown to be successful, laser-induced fluorescence (LIF) has the further advantage of offering high sensitivity and spatio-temporal resolution [40]. Comparison of LIF with other diagnostics highlights the benefits of LIF, especially when working with gas admixtures and unknown reaction partner densities. Calibration by Rayleigh scattering has been found to be promising and will be applied in this thesis [40].

Fourier-transform infrared (FT-IR) absorption spectroscopy is especially suitable to detect H_2O_2 in the effluent, as it has prominent absorption bands in the spectral range of $1200\,\mathrm{cm}^{-1}$ to $1300\,\mathrm{cm}^{-1}$ [27]. As H_2O_2 is a long-living species, it can be detected in the far-field. Using a multipass cell, even small fractions of H_2O_2 can be detected.

This work aims at expanding the knowledge on the OH and H_2O_2 densities in the effluent of an atmospheric pressure plasma capillary jet with regard to the variation of the dissipated plasma power, added feed gas humidity, gas flow and power modulation. Additionally, diagnostics are evaluated with regard to their potential and challenges for further work. The temperature of the system with regard to gas, effluent and components is determined by thermal probes and optical emission spectroscopy. The density and distribution of OH, the air admixture in the effluent and the H_2O_2 densities are by the aforementioned diagnostics. For both, absolute values and trends are compared with the concentration of reactive species measured in the liquid phase and simulations performed within the project [34, 36]. Finally, conclusions regarding potential future development are drawn based on the knowledge gained from this work to contribute to the project's goal to evolve the setup towards a sustainable and competitive solution for biological and chemical synthesis.

2. Theoretical Background

Plasma discharge characteristics exhibit strong dependence on the operating pressure. Thus, classification of plasmas based on their working pressure has proven useful, with low pressure, atmospheric pressure and high pressure plasmas being the three categories commonly employed.

Atmospheric pressure plasmas are ideal for applications that require mild working conditions, particularly those involving biological organisms such as enzymes used in biocatalysis [15–17]. Plasma sources operating at atmospheric pressure can be designed to make either direct or indirect contact with samples and surfaces [21]. In the case of indirect contact, an intermediate medium such as air is typically employed. Furthermore, atmospheric pressure plasma sources can be installed without the need for surrounding chambers or complex setups, thereby enhancing their versatility for a wide range of applications [41].

Hence, atmospheric pressure plasmas are currently the approach of choice for applications in the field of biocatalysis in interaction with plasmas. Several design concepts have been investigated by various research groups in recent years [15–17].

2.1 Atmospheric pressure plasmas and RF-plasmas

As atmospheric pressure plasmas are the focus of research on plasma-driven biocatalysis [15], this discharge type will be further categorised in the following.

Paschen's law provides the criterion for ignition of plasmas, specifying that the breakdown voltage depends on the pressure p, the distance d between the electrodes, and the working gas [42]. For small pd, where the electrons' mean free path is greater than the distance between the electrodes, a large breakdown voltage is required for ion acceleration to release secondary ions. When pd is large, collisions with neutrals cause the electrons to lose energy, leading to a rise in the breakdown voltage. Therefore, a minimum breakdown voltage is observed between the two regimes [42]. In atmospheric pressure plasmas, the pressure is fixed, and the electrode distance is varied to minimise the breakdown voltage.

In this work, a micro-scaled atmospheric pressure plasma jet (µAPPJ) is utilised, with its design based on the well-studied COST Reference Microplasma Jet [32]

that has also been studied in the context of biocatalysis [17].

Plasma jet configurations utilising dielectric barrier discharges are among the most commonly used atmospheric pressure plasma jet configurations [43]. Typically, a noble gas is introduced into a dielectric capillary, and an alternating voltage is applied through electrodes, which can be situated both inside and outside the capillary. Upon applying a suitable time-varying voltage, often in the radio-frequency (RF) regime at a frequency of 13.56 MHz, breakdown occurs, and a discharge forms within the capillary. Helium is often used as the working gas in µAPPJs due to the easily ignitable and homogeneous discharge it creates [44]. Application of an alternating voltage and placing the dielectric between the electrodes reduces the risk of arcing, which is the formation of a constricted discharge channel at higher powers, significantly and allows operation at higher powers than in setups without a dielectric [32, 33].

Two distinct electron power absorption regimes for RF-µAPPJs before switching to arcing are described in literature [45–47]. Specifically, the two modes, denoted as α- and γ-mode, are characterised by their respective emission characteristics. Bischoff et al. [48] suggest the terminology Ω-mode and Penning-mode, respectively, referring to the main heating mechanisms to avoid confusion with their low-pressure counterparts.

The Ω-mode is characterised by a high level of ionisation in the bulk, resulting from ohmic heating. Notably, local ionisation maxima are observed at the outer bulk regions, near the expanding and collapsing sheaths around the electrodes. Given the atmospheric pressure conditions, this mode is characterised by high collisionality and low bulk conductivity and is thus driven by a high bulk electric field [48].

In contrast, the Penning-mode is dominated by Penning ionisation in the sheath region. Here, the ionisation maxima occur near the instantaneous sheath edge when the sheath voltage reaches its maximum [48]. Specifically, Penning ionisation is a collisional process involving an excited (A^*) and a ground state (B) species, resulting in relaxation of the excited species and excitation of the ground state species, accompanied by the emission of an electron [49].

Plasmas are further classified into two categories based on their thermodynamic state: local and non-local thermal equilibrium. In local thermodynamic equilibrium (LTE), the electron and heavy particle temperatures are approximately equal, whereas, in non-local thermal equilibrium (non-LTE), there is no uniform temperature for all particles. In non-LTE, electrons have higher temperatures than heavy particles, which are usually at a temperature close to room tempera-

ture. This state is typically observed in µAPPJs, where the electron temperature is high, and the gas temperature is relatively low, which makes them suitable for applications involving heat-sensitive biological materials.

At the same time, the non-equilibrium state enhances chemical reactions and the production of various reactive species. This can be further altered by adjusting the gas mixture or bringing the capillary jet into contact with liquids.

2.2 Plasma chemistry

Water-containing plasmas typically produce atomic oxygen (O), hydroxyl radicals (OH), and hydrogen peroxide (H_2O_2) [21]. The chemistry involved in these discharges has been investigated by various research groups in the past. Of particular interest is H_2O_2, which is considered an important oxidant due to its high content of active oxygen [19, 22]. In current industrial development, there is a move towards environmentally friendly alternatives to conventional chemical processes, and H_2O_2 is viewed as a "green" alternative for a wide range of applications [21]. This is because the by-product of oxidising reactions with hydrogen peroxide is only water [23]. OH, as one of the primary precursors of H_2O_2, is also of significant interest. It believed to play a crucial role in several applications of atmospheric pressure plasmas and is one of the strongest oxidative species produced [40].

Moreover, both H_2O_2 and OH exhibit interactive behaviour with biological probes, emphasising the need to understand the production and distribution of both species in the effluent.

2.2.1 General chemical reactions

Chemical reactions inside a plasma depend on various processes. As outlined by Lieberman and Lichtenberg [50], these interactions predominantly involve reactions between species A and B and an electron e. Radical production is based on the process $e + AB \rightarrow e + A + B$ and is the main mechanism observed in the plasma source. Furthermore, electron-ion pair production ($e + AB \rightarrow AB^+ + 2e$), negative ion production ($e + AB \rightarrow A^- + B$), as well as gas-phase chemical reactions ($A + B \rightarrow C + D$) and transport to surfaces and surface-phase reactions can occur. The discharge power source must supply the absorbed net energy by the plasma reactions [50].

In plasmas operating under non-equilibrium conditions, the kinetics of reactions

are determined by the collisions between the species present in the plasma. Therefore, the reaction rates and steady-state distribution of species inside the reactor must be taken into consideration [50]. The rate coefficients are highly dependent on the energy distributions of the reactants, and for Maxwellian energy distributions, temperature can serve as a measure [51].

As atmospheric pressure discharges operate under non-equilibrium conditions, the reactions of gas-phase species s (here: A, B, C) can be determined from the rate constants k_s, their densities n_s, and their time derivatives. Due to the complexity of many reactions, rate equations are typically solved numerically, and often the set of equations is simplified to obtain insights [50].

For consecutive, time-varying first-order reactions without sources or sinks, the following applies [50]:

$$\mathrm{A} \xrightarrow{\mathrm{k_A}} \mathrm{B} \xrightarrow{\mathrm{k_B}} \mathrm{C} \tag{2.1}$$

Subsequently, the corresponding rate equations can be written in the form of a set of differential equations, given as follows:

$$\frac{dn_\mathrm{A}}{dt} = -k_\mathrm{A} n_\mathrm{A} \tag{2.2}$$

$$\frac{dn_\mathrm{B}}{dt} = k_\mathrm{A} n_\mathrm{A} - k_\mathrm{B} n_\mathrm{B} \tag{2.3}$$

$$\frac{dn_\mathrm{C}}{dt} = k_\mathrm{B} n_\mathrm{B} \tag{2.4}$$

In terms of association mechanisms, three-body association represents one such mechanism for the association reaction along with bimolecular association involving photon emission. This involves the associating bodies colliding with a third body, denoted as M, that can be any molecule in the system:

$$\mathrm{A} + \mathrm{B} + \mathrm{M} \rightarrow \mathrm{AB} + \mathrm{M} \tag{2.5}$$

Simultaneous collisions between three bodies are rare at low pressures. However, they become important at atmospheric pressure [50].

2.2.2 Main generation and loss mechanisms

While the previous section focused on general chemical reactions, now the focus shifts to the specific generation and loss mechanisms of the produced reactive species, particularly OH and H_2O_2.

It has been found that OH and H_2O_2 are mainly formed in the plasma and travel through the effluent [36]. While H_2O_2 is a long-living species, OH is highly reactive [27]. Vasko et al. [19] investigated the generation and loss mechanisms of OH and H_2O_2 and provide an overview of the main reactions.

OH is primarily formed through the interaction between an electron e and a water molecule H_2O.

$$\mathrm{e} + \mathrm{H_2O} \rightarrow \mathrm{H} + \mathrm{OH} + \mathrm{e} \tag{2.6}$$

For atmospheric pressure plasmas with humid feed gas at temperatures between 300 K to 400 K, the main loss mechanism for the hydroxyl radical is three-body recombination with a heavy collisional partner M to form H_2O_2. This process also dominates the generation of H_2O_2 [19].

$$\mathrm{OH} + \mathrm{OH} + \mathrm{M} \rightarrow \mathrm{H_2O_2} + \mathrm{M} \tag{2.7}$$

Reducing the chemistry to this first-order approximation, the production of one H_2O_2 molecule consumes two OH molecules and is therefore linearly correlated. But OH does not only determine the production but also becomes important in the destruction of H_2O_2 at higher OH concentrations as they react to

$$\mathrm{OH} + \mathrm{H_2O_2} \rightarrow \mathrm{H_2O} + \mathrm{HO_2} \tag{2.8}$$

Further losses of OH and H_2O_2 are contributed to radial losses, electrode losses and other minor mechanisms. A full overview of the set of reactions in water-containing plasmas is given in [51].

2.3 Diagnostics

Optical diagnostics of the plasma can be performed in-situ and offers both non-invasive and invasive methods for several applications. The plasma chemistry is strongly determined by the prevailing temperature and species. In the following,

diagnostics for the thermal and chemical analysis are therefore outlined.

2.3.1 Optical emission spectroscopy

Optical emission spectroscopy (OES) is a non-invasive, real-time diagnostics that is used for various purposes [52]. It is of special interest for plasmas that are of small scale and are difficult to access as it provides insight into various plasma parameters from outside the plasma and can be performed through glass. In addition, the implementation of diagnostics is simple, as commercially available spectrometers are available for this purpose, which collect and evaluate the emitted radiation via a lens system and optical fibre. Furthermore, it is not disturbed by RF-fields in proximity to the setup.

OES makes use of the electromagnetic radiation emitted by plasmas. The emitted photons can be measured spectrally resolved by a spectrometer and a wavelength-dependent analysis of the spectra allows the determination of several plasma parameters. Some of those are the determination of components of the gas admixture, electron dynamics for time-resolved measurements and determination of temperature from rotational spectra. All of these are based on the radiation emitted by the atoms and molecules in the plasma.

The plasma particles are excited from level q to level p by electron impact. The decay by spontaneous emission to level k with transition probability A_{pk} causes monoenergetic line emission ϵ_{pk} [52]. The electron energy levels are characteristic for each species, therefore the photon that is emitted when the particle relaxes is clearly assignable to the species by its wavelength. The central wavelength of the emission line is determined by the energy gap $E = E_p - E_k$ that corresponds to the photon energy.

As only photons emitted from the excited state are detected, no information on the ground state is given. Instead, only information on the excited state is gathered.

Rotational temperature of diatomic molecules

Temperature measurements inside the discharge of APPJs are challenging due to the narrow discharge channel and limited accessibility. Furthermore, inserting a probe into the discharge channel may alter the discharge characteristics as for example gas flow, volume and conductivity inside the channel are changed [53].

Optical emission spectroscopy offers a solution for temperature measurements.

Non-LTE plasmas can often be characterised by three temperatures where the *electronic temperature* characterises the portion of electronically excited molecules, the *vibrational temperature* represents the population distribution among vibrational levels and the *rotational temperature* represents the population distribution among rotational levels [54].

Optical analysis of the rotational emission lines allows conclusions about the rotational temperature and vibrational temperature of the species. The gas temperature is approximately equal to the rotational temperature if occupation of the rotational states is at equilibrium. In detail, according to the Franck-Cordon principle, the rotational quantum number has to be conserved during electron impact excitation processes and the internuclear distance must be constant at all times. If this condition accounts, excited state and ground state hold the same rotational temperature. Additionally, in the ground state, the rotational levels must be populated by heavy particle collisions [52].

While this assumption is often believed to be true, it has been found that the description of some systems by their vibrational and rotational distribution by the Boltzmann function is not possible [54]. Often, dissociation or recombination result in such non-Boltzmann, or nascent, distributions [54].

The rotational temperature as a measure of the gas temperature is usually determined from the N_2^+ (391 nm) and OH (309 nm) and has been a widely established and validated method [53]. In helium plasmas, the temperature is often overestimated via the N_2^+ bands, as nitrogen and helium interact [55]. Also, the emission of the $OH(A^2\Sigma^+ \rightarrow X^2\Pi)$ (OH(A-X)) bands is very intense in most discharges operated with water admixture or impurities due to plasma operation in open air [55]. The OH(A-X) transition has been extensively studied and all constants are available in the LIFBASE database [56] allowing a precise analysis. Also, band heads are clearly distinguishable even at lower resolutions as the reduced mass involved in the rotational constant of OH is small in comparison to N_2 [53].

The OH(A-X) is one example of a system that often features a non-Boltzmann distribution. It is well studied and therefore standardised determination of the gas temperature from this molecular system is possible [53, 57–59]. In many cases, non-thermalised systems have been found to be thermalised for low rotational levels N, therefore analysis is still successful regarding the lowest levels [53].

The observed spectrum is not only determined by the structure of the vibrational bands but its shape is heavily influenced by the spectral resolution of the detection system [52]. Therefore, line broadening must be applied to obtain accurate fits.

The rotational temperature can be determined both from comparison with simulations of the observed spectra or from a Boltzmann plot. Determination of the gas temperature from a Boltzmann plot is beneficial when working with non-Boltzmann distributions [54]. A Boltzmann plot is "a semilogarithmic plot of populations in individual quantum levels divided by their degeneracy vs their potential energy" [54]. Here, a linear trend is observed for thermalised distributions. From the slope, the temperature is deduced. Deviation from a straight line clearly indicates a deviation from an equilibrium distribution.

2.3.2 Resonant Fluorescence

Resonant fluorescence uses active perturbation of the species in the excited state to gain information about species densities [60]. It has the advantage of localisation of the measurement region and therefore allows for spatial resolution.

In resonant fluorescence, intense electromagnetic radiation is used to irradiate a sample at the resonant frequency of the species of interest [60]. The radiation at the frequency is generally produced by a tunable laser as those are able to operate at correct frequency and sufficient intensity [60]. By exciting the species at the resonant frequency, transitions between the corresponding atomic levels are induced. Therefore, the population of states is altered towards stronger population of higher states causing a change in the emitted radiation [60].

Radiation observed at the same transition as the one that was excited is called fluorescent. In this case, the observed radiation is induced by spontaneous transitions from the higher level [60].

Laser-induced fluorescence (LIF) has been studied since the 1970s [61]. In low temperature plasmas, ground state atoms are the most populated state. LIF can be used to determine the density in ground state and is therefore suitable for the diagnostics of plasma jets.

LIF is based on the excitation of a selected atom or molecule by single photons. Laser radiation is absorbed at a frequency corresponding to a suitable transition from ground to excited state. Suitable transitions are mostly found to be those with the largest cross-section. After a time of typically a few nanoseconds to microseconds, the exited species de-excites emitting a photon at a wavelength higher than the excitation wavelength. This fluorescent light can then be detected by a camera, photomultiplier or photodiode through a filter [62].

For the detection of OH, the transitions of the OH($X^2\Pi - A^2\Sigma^+$) system is used. This is favourable, as collisional phenomena are well known in this regime due

to extensive research. In addition, its rotational structure features weakly overlapped branches as well as widely spaced rotational lines. It is therefore easy to isolate the rotational-vibronic lines using lasers operating at medium bandwidth [63]. The transition is then characterised as

$$\mathrm{OH}(X^2\Pi_i, \nu, N) + h\nu_L \rightarrow \mathrm{OH}(A^2\Sigma^+, \nu', N') \rightarrow \mathrm{OH}(X^2\Pi_i, \nu'') + h\nu_F. \tag{2.9}$$

The fluorescence signal is directly proportional to the trace gas concentration The species densities are determined by calibration of the signal [62].

One challenge of LIF is the separation of the fluorescence signal from Rayleigh scattered exciting radiation.

Rayleigh scattering is a predominately elastic collisional process of electromagnetic radiation with a scatterer of a smaller magnitude than the exciting wavelength [64]. The scatterer can be both an atom or a molecule. During the process, there is no energy transfer, so that scattered light has the same frequency as its origin [65]. Due to the Doppler effect, there may be a small shift in energy though [66]. For the scattering with molecules, the energy of the incident photons is conserved no matter which molecule acts as the scatterer. Therefore, Rayleigh scattering itself is not suitable to determine the mixture components. Rayleigh scattering from molecules must be applied in a very clean environment, as the elastically scattered signal is otherwise not primarily caused by Rayleigh scattering but scattering from drops and particles in the surrounding [66].

The intensity I of Rayleigh scattering is highly dependent on the laser energy E_L and laser wavelength λ_L as

$$I \propto E_L \cdot L_{ij} \cdot N \cdot \left(\frac{1}{\lambda_L}\right)^4 \cdot \alpha_0^2, \tag{2.10}$$

where L_{ij} is the local field, N is the number of scattering molecules and α_0 the polarisability [66].

Quenching further influences the detected LIF signal as decreases the intensity of the LIF signal. In quenching, any process that reduces the fluorescence intensity is regarded [67]. Regarding the decay of an excited species, the fluorescence decays exponentially with the excited state population. The lifetime τ of the excited species is then a result of various processes with rate k.

$$\frac{1}{\tau} = k_{\mathrm{f}} + k_{\mathrm{q}} + k_{\mathrm{nf}} \tag{2.11}$$

where k_{f} indicates the radiative decay of the fluorescent species, k_{q} decay due to quenching and k_{nf} all other non-fluorescent decay phenomena. Quenching then leads to a reduction of the lifetime of the fluorescent species.

2.3.3 Absorption spectroscopy

On the contrary to OES and LIF, absorption spectroscopy relies on the absorption of electromagnetic radiation by molecules. It offers determination of ground-state species densities of molecules which absorb in the spectral infrared regime and is therefore of high interest for chemical composition analysis [26]. Each molecule has a characteristic spectrum which yields information on the concentration and rotational- and vibrational state.

The number of molecules N_j at energy E_j and temperature T in a gas mixture can be expressed by a Boltzmann distribution. This distribution is given by

$$N_j = N_0 g_j \exp\left(-\frac{E_j}{k_B T}\right) \tag{2.12}$$

with the particle number in ground state N_0, statistical weight g_j of the energy state j and Boltzmann constant k_B [68].

In quantum mechanics, absorption is interpreted as the transition from energy level j to a higher level k with regard to the Einstein coefficient B_{jk} that determines the absorption probability. The change of particles at energy level k is then given by

$$\frac{dN_k}{dt} = -N_k B_{jk} \rho(\nu). \tag{2.13}$$

where $\rho(\nu)$ denotes Planck's law, which defines the spectral density of the absorbed electromagnetic radiation [69]. Planck's law is expressed via the frequency ν of the radiation, the speed of light c and Planck's constant h as

$$\rho(\nu) = \frac{8\pi h\nu^3}{c^3} \cdot \frac{1}{e^{\frac{h\nu}{k_B T}} - 1}. \tag{2.14}$$

The decrease of the intensity of the absorbed radiation is expressed by Beer-Lambert law as

$$I = I_0 e^{-\alpha l} \tag{2.15}$$

with intensity I_0 of the incident radiation, absorption coefficient α and path length of the light beam inside the absorbing medium l. The absorption coefficient is determined by the concentration of the absorbing molecule c and the molar absorption coefficient ϵ.

$$\alpha = \epsilon c \tag{2.16}$$

Comparison of the radiation intensity before and after passing the gas mixture then yields information on the concentration of the absorbing molecule in the mixture [70].

Fourier-transform infrared spectroscopy

Fourier-transform infrared (FT-IR) spectroscopy utilises radiation in the infrared region to perform absorption spectroscopy. In water-containing plasmas, several species are infrared active, such as H_2O and H_2O_2 [27]. Molecules need to feature a net change in their dipole moment to be infrared active. As this is not the case for molecules like N_2, nitrogen can be used as a "transparent" ambient gas for FT-IR spectroscopy.

An FT-IR spectrometer is based on the principle of the Michelson interferometer. Its basic setup consists of a beam splitter and two mirrors, one of whom is movable. The radiation intensity $I(z)$ after passing the sample is then measured depending on the position of the mirror z. The wavenumber-dependent intensity distribution $I(\nu)$ is then obtained by performing a Fourier transformation on the data [68].

$$I(\nu) = \sum_{n=0}^{N-1} I(z) e^{-2\pi i n k/N} \tag{2.17}$$

The transformation is performed over the total number of mirror positional steps N and $k \in \mathbb{Z}$. The concentration of the analysed species is then deduced from equation 2.15.

3. Experimental Setup, Procedure and Data Analysis

In this chapter, the plasma source including gas and power supply is described below. The diagnostics and models used to evaluate the data are then presented for temperature measurement, laser-induced fluorescence and Fourier-transform infrared spectroscopy.

3.1 Plasma setup

The setup consists of three major elements, namely the plasma source, gas supply and power supply and control. The whole setup is shown in figure 3.1.1. The plasma source is provided with feed gas by the gas supply and is driven by the power supply and controlled by in-situ power measurements. These elements are described in detail in the following sections. The adjustment of the plasma source is outlined subsequently.

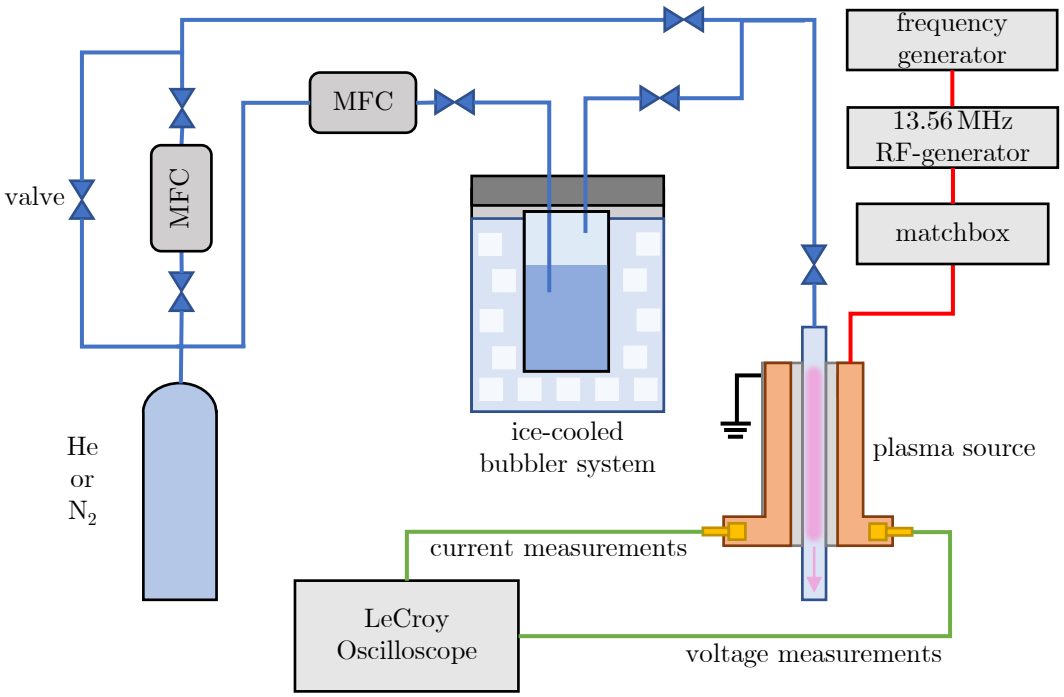

Figure 3.1.1: Setup with plasma source (bottom right), gas supply (top left) and power supply (top right) and power measurements (bottom centre).

3.1.1 Capillary jet

The capillary jet used in this work offers similar discharge behaviour and geometry to the COST-jet [32]. The range of variability of the parameters such as input power and discharge volume is expanded by igniting the plasma inside a capillary between the electrodes which acts as a dielectric. Winzer et al. [33] have provided a first characterisation of the jet as well as first evidence that the new design meets the requirements of an extended parameter variability.

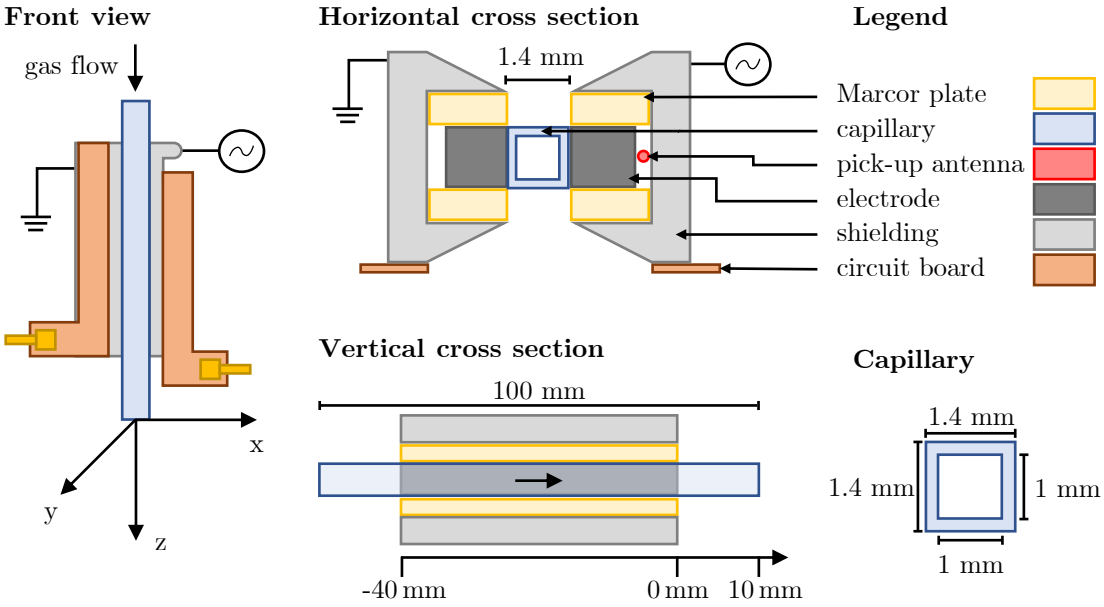

Figure 3.1.2: Schematic sketch of the plasma source from different perspectives. Detailed sketch of the plasma source in front view with coordinate system (left), horizontal cross section with view of interior components (top central), vertical cross section with positional nomenclature (bottom central), cross section of capillary with dimensions (top right) and legend for colour-coded components (bottom right).

Sketches of the plasma source are shown in figure 3.1.2. The figure features the plasma source in front view and once in a horizontal and once in a vertical cross-section. In addition, the capillary is shown with its dimensions. Also, the coordinate system applied for spatially resolved measurements and the nomenclature for positions along the gas stream are shown.

The jet is designed as a modular system that allows for precise adjustment of the components by means of a rod system and easy interchangeability of the single components of the plasma source.

The capillary jet consists of a borosilicate glass capillary (CM Scientific) with a quadratic inner cross-section of 1 mm and 0.2 mm wall thickness with $\pm 10\,\%$ tolerance. The total length of the capillary is 100 mm.

Two parallel stainless steel electrodes (itec Automation & Laser) of 40 mm length are placed on either side of the capillary in 1.4 mm distance from each other. The distance between the end of the electrodes and the end of the capillary is set to (10.0 ± 0.5) mm. For reference, the nomenclature of the coordinate system is depicted in the bottom centre of figure 3.1.2. Marcor plates separate the electrodes from the grounded shielding. The resulting electric field between the electrodes is closely confined [33].

The capillary is connected with Viton tubing (Keller Elastomere), which has a diameter of 1 mm, to the gas supply by a Swagelok adapter. Ceramic glue (T-E-Klebetechnik) is used to connect the tubing and the capillary and seal the transition between both.

3.1.2 Gas supply

The gas supply of the setup is shown in the top left of the setup in figure 3.1.1. The helium and nitrogen feed gas of the capillary jet is supplied via 10 L gas bottles (5.0 purity, Air liquide). A gas panel with a 2 slm mass flow controller (MFC, Analyt MTC) is used for the main feed gas. A bubbler system is also equipped with a 2 slm MFC (Analyt MTC). The borosilicate glass bubbler reservoir (Evac) is filled with 70 mL of distilled water to add water vapour to the feed gas. The reservoir sits inside a 946 mL double-walled stainless steel isolating vessel (Klean Kanteen) filled with 400 mL of cold water at 6 °C and 900 mL of ice cubes. The system is sealed with a polystyrol lid and temperature controlled by a type-K thermocouple attached to the outside of the bubbler reservoir.

Valves ensure secure operation of the MFCs and controlled admixture of water vapour into the feed gas. All tubing up to the joint to the capillary is made of stainless steel to avoid impurities penetrating the gas flow. A change to Viton tubing to connect the capillary to the gas supply is necessary to allow for flexibility in the adjustment of the setup and reduce the forces on the fragile capillary [33].

The temperature of the cooled bubbler is at (1.4 ± 0.5) °C. It is assumed to be constant over all measurements, as the bubbler temperature does not change over several hours and the ice-water coolant is replaced every day before starting the measurements. Measurements are taken earliest one hour after replacing the coolant to ensure the system is at steady-state. The error of the bubbler temperature does not account for a potential increase in feed gas temperature while passing the uncooled tubing between the bubbler and plasma source.

The calculation of the humidity of the feed gas is derived from the partial pressure of the water vapour based on the Antoine equation. The full calculation and error estimation is given in the appendix (section A). The gas flow parameters and corresponding feed gas humidity are given in table 3.1.

Table 3.1: Gas flow and added feed gas humidity at $(1.4 \pm 0.5)\,^{\circ}\mathrm{C}$ water temperature inside the bubbler.

fraction of bubbler flow to total flow	feed gas humidity	percentage of water vapour in feed gas
0 %	0 ppm	0 %
10 %	(640 ± 30) ppm	0.064 %
30 %	(1900 ± 80) ppm	0.19 %
50 %	(3200 ± 130) ppm	0.32 %
100 %	(6400 ± 250) ppm	0.64 %

3.1.3 Power supply and control

The system is powered by a 150 W 13.56 MHz RF-generator (Coaxial Power Systems: RFG 150-13) coupled to a matching system (Coaxial Power Systems: MMN 150-13). The generator can be either controlled via the panel on the device or by a computing device (Arduino). The Arduino is connected to a computer and the input settings are submitted via a Labview program. The schematic diagram for the electrical setup including power supply and power measurements is given in figure 3.1.3.

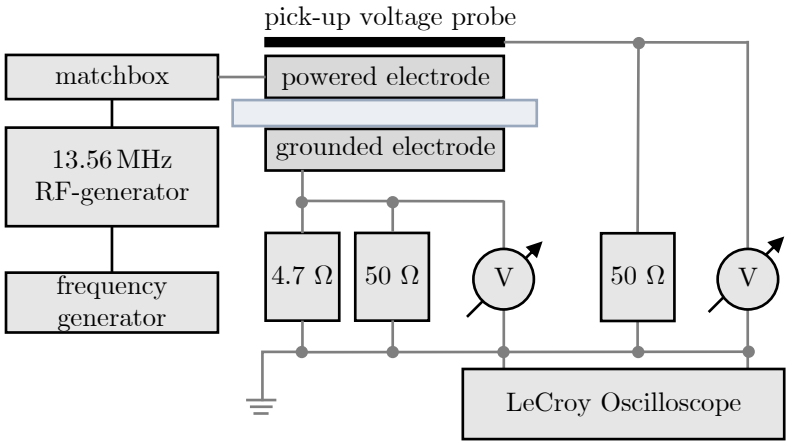

Figure 3.1.3: Schematic diagram of the electrical setup implemented for power supply and measurements. Figure adapted from [33].

The power output from the generator is always higher than the deposited power in the plasma due to losses in the matching system, cables and electrodes. Winzer

et al. [33] have found, that less than 10 % of the generator power transfers to the plasma power. Therefore, power measurements are necessary to obtain comparable data for the plasma power.

The plasma power is determined from simultaneous current and voltage measurements at the jet. The voltage is measured using a pick-up antenna behind the powered electrode (see figure 3.1.2). As this setup does not directly measure the voltage but measures the voltage induced into the cable, calibration is performed using a high voltage probe (Tektronix P5100A) connected to the powered electrode at 30 W generator power without gas flow. Calibration is performed after each readjustment of the setup.

For current measurements, a second voltage over a 4.7 Ω resistor between electrode and ground is measured. 50 Ω terminating resistors are used to connect the BNC cables for voltage and current measurements to the oscilloscope to minimise distortion of the signal and standing wave effects. The current is then directly proportional to the voltage drop U_I via Ohm's law as

$$I = \frac{R_\mathrm{I} + R_\mathrm{T}}{R_\mathrm{I} R_\mathrm{T}} \cdot U_\mathrm{I} \tag{3.1}$$

with measuring resistor R_I and terminating resistor R_T [32].

The voltage signal is read out by an oscilloscope (Teledyne Lecroy: Waverunner 8404M-MS or HDO6104A) with a sampling rate of at least 1 GHz, allowing for high resolution detection of the voltage signals.

The reference phase $\Delta\varphi_0$ is measured at 30 W generator power without gas flow to take system-specific phase shifts in the power measurements into account. The system-specific phase shift is determined by components like cables, connectors and resistors. The reference phase shift is calculated as

$$\Delta\varphi_0 = \Delta\varphi_{\mathrm{U,Ref}} - \Delta\varphi_{\mathrm{I,Ref}} \tag{3.2}$$

The dissipated plasma power then calculates to

$$P = U_\mathrm{rms} \cdot I_\mathrm{rms} \cdot \cos\left(-\frac{\pi}{2} + \Delta\varphi - \Delta\varphi_0\right) \tag{3.3}$$

where $U_\mathrm{rms} = \frac{U_0}{\sqrt{2}}$ and $I_\mathrm{rms} = \frac{I_0}{\sqrt{2}}$ are the effective values of voltage and current respectively and $\Delta\varphi_0$ is the reference phase shift. $\Delta\varphi$ is the phase shift between voltage and current that is determined by applying a fit function.

For in-situ power measurements, the Python program COST power monitor [71]

is used. The power is determined according to the method described in [72]. Random comparison between manually calculated dissipated power from the raw voltage signal of the oscilloscope and the power calculated by the COST power monitor is in good agreement.

Power modulation

The power supply can be operated in **power modulated operational mode** to modify the plasma-on and plasma-off time and therefore excitation mechanisms. For this, a frequency generator (Tektronix: AFG 3011) is attached to the power generator. Pulses are always set to a rectangular shape, duty cycle and frequency can be set individually. The generator takes about 10 ns to reach the signal voltage.

Power measurements are not possible during pulsing. As the electrodes cool down during the plasma off-time, the power decreases for low duty cycle values. To account for this, the power is set to the desired value before turning on the frequency generator and measured again after the measurement to determine the error of the dissipated plasma power.

The number of pulses per residence time N_{ppr} of the particles in the plasma are determined via

$$N_{\mathrm{ppr}} = \frac{T_{\mathrm{pulse}}}{t_{\mathrm{res}}} = f_{\mathrm{pulse}} \cdot t_{\mathrm{res}} \tag{3.4}$$

with the residence time t_{res} of the particles in the plasma, pulsing period T_{pulse}, pulsing frequency f_{pulse}. The residence time is geometry dependent as

$$t_{\mathrm{res}} = \frac{l_{\mathrm{plasma}}}{v} = \frac{l_{\mathrm{plasma}} \cdot A}{\phi_{\mathrm{total}}}. \tag{3.5}$$

where l_{plasma} is the length of the discharge which is, if not otherwise stated, 40 mm, v is the particle velocity, A the capillary cross-section and ϕ_{total} the total gas flow. For a square capillary at a gas flow rate of 1 slm, for example, a residence time of 2.4 s is the result. The parameters used are listed in table A.1 in the appendix.

3.1.4 Adjustment of the capillary jet

Adjustment of the jet is performed according to the following criteria to ensure comparability of the measurements, high conversion rate of generator to plasma

power and high discharge stability. The electrodes are aligned along the capillary and their position is optimised so that the power coupling corresponds to about 6.5 W dissipated plasma power at 30 W generator power for 1 slm dry helium. In addition, the discharge must burn homogeneously along the discharge channel. The criterion for this is, on the one hand, a uniform discharge at high powers and, on the other hand, a uniform decrease in intensity over the entire discharge as the power decreases. At low powers, the plasma must contract centrally between the electrodes and decay under 3 W generator power.

3.2 Temperature measurements

The characterisation of the heating of the plasma source is performed by identifying the effluent and gas temperature as well as the temperature of selected components of the plasma source in proximity to the plasma, explicitly the capillary and electrodes. The measurements to determine the gas and components' temperature as well as the routine applied for their analysis will be outlined in the following.

Direct temperature measurements are not possible inside the plasma due to the narrow discharge channel and limited accessibility of the capillary. Thus, the temperature must be determined from the outside. Two diagnostics for the gas temperature determination are applied to verify the obtained temperatures. The measurements are performed using a thermocouple and via the determination of the rotational temperature of OH based on the methodology in [33].

3.2.1 Gas temperature extrapolation from effluent temperature

A NiCr-Ni thermocouple type K (B+B Thermo-Technik) suitable for temperatures from $-50\,^{\circ}\mathrm{C}$ to $260\,^{\circ}\mathrm{C}$ connected to a two-channel thermometer (Voltcraft) is placed in the effluent. The tip is positioned 1 mm from the capillary end at the position with maximum temperature to ensure the measurements are performed centrally in the gas stream. Plastic tubing is placed behind the capillary end to reduce the influence of turbulence in the ambient air on the measurements. The tube is sealed to hinder cold, ambient air from being pulled into the flow channel.

Extrapolation from effluent to gas temperature

Thermocouple measurements are performed 11 mm from the plasma. Extrapolation is performed to account for the temperature drop along the way. The

distance-dependent temperature drop is determined from temperature measurements in 2 mm steps in the range of 11 mm to 23 mm from the plasma.

The effluent's temperature features a linear behaviour in proximity to the capillary end. The temperature measured in the effluent at varied distance is fitted by equation 3.6 and yields the increase factor f which gives the ratio between the extrapolated gas temperature $T_{ex}(0)$ at the end of the plasma and the measured temperature 11 mm from the plasma.

$$T_{ex}(z) = a \cdot (z - 10\,\text{mm}) + b \tag{3.6}$$

$$f = \frac{T_{ex}(0)}{T_{\text{eff},\,11\,\text{mm}}} \tag{3.7}$$

The decrease for the minimum and maximum investigated plasma power was measured in 2 mm steps in the range of 11 mm to 23 mm from the plasma. This provides an approximation of the variability of the temperature decrease in the effluent. In addition, the decrease at 6 W is determined for a wider range of distance of 10 mm to 30 mm to check the linearity of the decrease. For the measurements, the mean increase is used and the deviation of increase at low and high powers is taken into account for in the error. The error of the increase is obtained from error propagation.

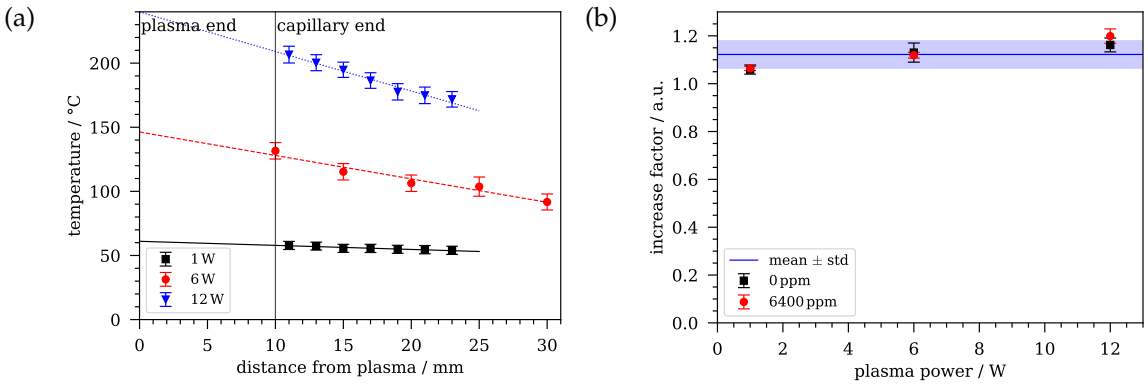

Figure 3.2.1: Calibration of gas temperature from thermocouple measurement of effluent temperature from (a) linear fit of temperature at varied distance at 0 ppm feed gas humidity and (b) increase factor deduced from linear fit depending on plasma power for 0 ppm and 6400 ppm feed gas humidity.

An example of the calibration and linear fit for 0 ppm feed gas humidity is shown in figure 3.2.1a. The temperature decreases linearly for all plasma powers. The increase factor for 0 ppm and 6400 ppm is shown in figure 3.2.1b with the mean increase factor and standard deviation over all values. The increase factor rises

with increasing plasma power. A complete overview of the results of the parameters of the linear fit of the data at 1 W, 6 W and 12 W at 0 ppm and 6400 ppm feed gas humidity and the deduced increase factors is given in table A.2 in the appendix. For the extrapolation, a mean increase of (1.12 ± 0.06) is used.

Uncertainty estimation

The thermocouple is positioned at the maximum temperature. Manual positioning of the thermocouple in the effluent causes uncertainty of 3 °C for plasma powers from 1 W to 4 W and 5 °C for 6 W to 12 W resulting from a slight offset of the fibre from the point with maximum temperature when fixing the position of the fibre. The statistical error of the effluent's temperature is determined from the standard deviation of the mean value obtained from measurements over the course of 2 min. The total uncertainty of the effluent's temperature is then obtained from the sum of statistical uncertainty and uncertainty from positioning the fibre.

The error of the extrapolated gas temperature results from Gaussian error propagation with regard to the error of the effluent's temperature, which is determined individually for each data point, and the error resulting from the extrapolation with a mean temperature increase for all plasma powers and feed gas humidity levels.

3.2.2 Rotational temperature by optical emission measurements

A schematic sketch of the setup used for optical emission spectroscopy is shown in figure 3.2.2. A 600 µm optical fibre (Ocean Insight) is connected to a UV/VIS collimating lens (Ocean Insight) to collect the emission. The collimator is placed (33 ± 2) mm from the capillary at central vertical position where the detected emission signal is at its maximum and no significant increase in the ambient temperature due to radiation from the capillary jet is measured.

The optical fibre is coupled to a second optical fibre (Ceram Optec) that is connected to the entrance slit of the spectrograph (Acton: Research Spectra Pro 750). The emitted light enters the spectrograph through a (15.00 ± 0.25) µm entrance slit and is directed by mirrors onto the grating. The incident light beam is diffracted by the grating and is split according to the wavelength. The fanned-out beam is then reflected by a third mirror onto a camera (Princeton Instruments: PI-MAX) which is mounted to the spectrograph.

The spectrograph is set to a central wavelength of 308 nm. The triple grating

is set to 1800 grooves mm^{-1} for high resolution at a narrow spectral window. Measurements are performed in gate mode at 4 ms acquisition time, gain of 255 and are accumulated over 100 scans. The spectral resolution of the system is (184 ± 5) pm pixel^{-1}. Spectra are taken 5 min after changing the parameters to allow the system to stabilise.

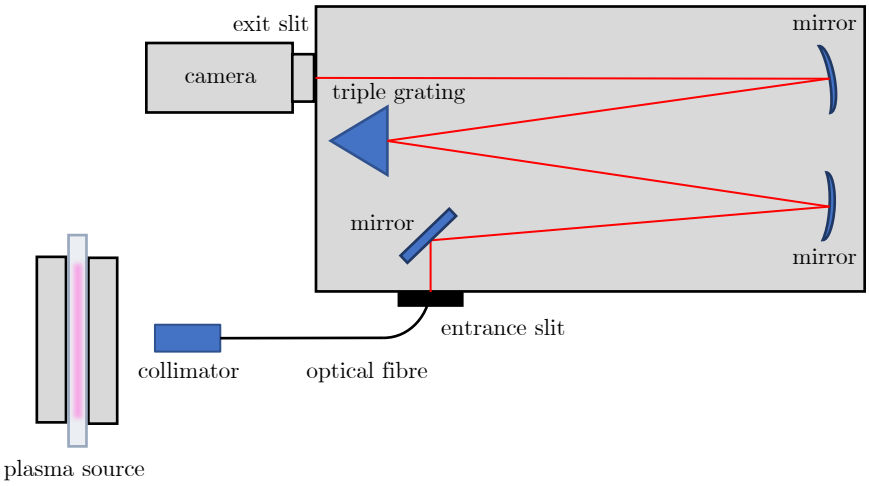

Figure 3.2.2: Schematic sketch of setup used for optical emission spectroscopy of the active plasma zone.

Calibration and fit of spectra

Precise wavelength and intensity calibration is necessary to obtain accurate results from fitting the spectra.

Wavelength calibration is performed by comparison of the wavelength positions of a simulated spectrum (LIFBASE) and an experimental reference spectrum taken at the settings used for the measurements. The shift in wavelength $\Delta\lambda$ is then plotted against the experimental peak position (figure 3.2.3a). A linear fit has turned out to yield the highest accuracy of the fitting parameters with an R^2 value of 0.98405 in comparison to higher polynomials and a sinusoidal fit. The obtained parameters are a slope a of (-0.0341 ± 0.0010) and an intercept b of (10.78 ± 0.29) nm. The corrected wavelength λ is then calculated from the measured wavelength λ_{meas}

$$\lambda = \lambda_{\mathrm{meas}} + a \cdot \lambda_{\mathrm{meas}} + b. \tag{3.8}$$

The comparison of the peak positions of a simulated spectrum and a wavelength-calibrated spectrum is shown in figure 3.2.3b. No shift between the peaks can be observed anymore. The residual mostly results from deviation between the am-

plitude in the spectra, partly due to overlap of the lines resulting from broadening of the experimental spectrum.

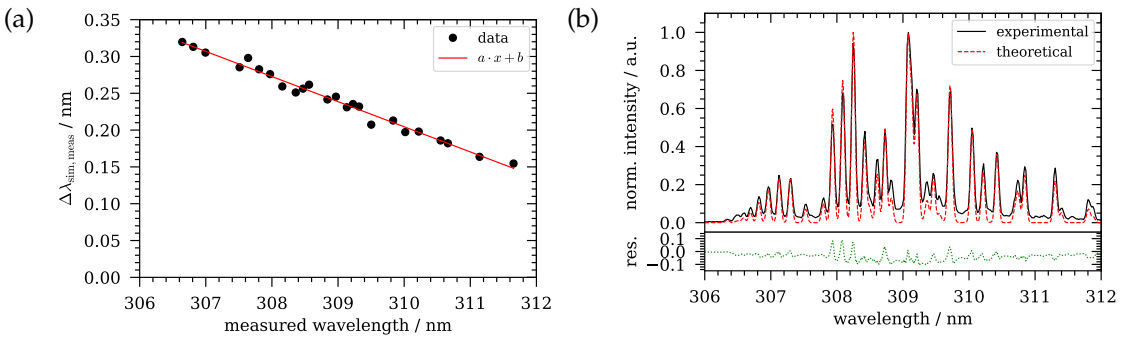

Figure 3.2.3: Wavelength calibration of optical emission spectra from comparison with simulated spectrum. (a) Shift in wavelength between experimental and simulated theoretical spectrum plotted against the experimental peak wavelength. Data fitted with linear model. (b) Validation of peak agreement of simulated (LIFBASE) and wavelength shifted experimental spectrum (top) and residual of fit (bottom). Experimental reference spectrum taken at 1 slm He gas flow rate, 640 ppm feed gas humidity and 6 W dissipated plasma power.

Relative intensity calibration of the spectrum is performed with a Deuterium Tungsten-Halogen Calibration Light Source (Ocean Optics: DH-3 plus). A cosine-corrector is connected to the 600 µm optical fibre and placed directly at the exit of the lamp. After a warm-up of the lamp, a calibration spectrum is measured at 308 nm central wavelength with the 1800 grooves mm^{-1} grating. The measured calibration spectrum $I_{cal,meas}$ is then compared to the interpolated theoretical calibration spectrum $I_{cal,theo}$ of the lamp to obtain a wavelength-dependent intensity scaling factor c_I. The intensity calibrated spectrum I then equates from the experimental spectrum I_{exp} to

$$I = \frac{I_{cal,theo}(\lambda)}{I_{cal,meas}(\lambda)} \cdot I_{exp} = c_I(\lambda) \cdot I_{exp} \tag{3.9}$$

The **fitting routine** is performed by massiveOES [54, 57, 58]. It is used to batch process and fit the spectra. The rotational temperature can then be determined from the rotational spectrum as the relative intensity of the Q, P and R-branches which are simulated by the software.

Figure 3.2.4 displays a normalised example spectrum taken at a gas flow of 1 slm helium and 6 W generator power. From this, the major rotational transitions, their branches and quantum numbers are determined and shown in the spectrum. From the total twelve branches, only six, namely P_1, P_2, Q_1, Q_2, R_1 and R_2, are found to be dominating in the area and temperature range of interest. Also, the major spectral lines correspond to quantum numbers up to $K = 7$. The

transitional data is taken from LIFBASE [56].

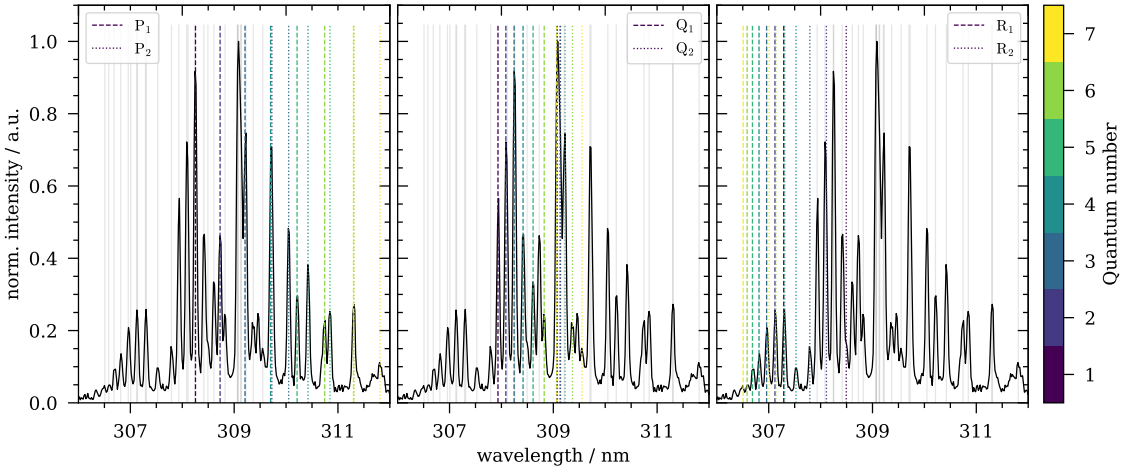

Figure 3.2.4: Normalised spectrum of OH(A-X) with quantum branches of P_1, P_2 (left), Q_1, Q_2 (centre), R_1 and R_2 (right) for quantum numbers up to 7 [56]. Branches are indicated with opaque grey line in all spectra for better visibility. The spectrum is taken for 1 slm helium gas flow, 0 ppm feed gas humidity and 6 W plasma power.

The dominance of lower quantum numbers justifies the assumption of thermal equilibrium for the fitting routine. Even in the case of non-thermalised systems, research has shown that many are still thermalised for low rotational levels enabling analysis of the spectra based on these systems [53]. The gas temperature has then to be determined only from rotational states with $J \leq 7$ to determine the gas temperature adequately [73] which matches the branches present in the spectrum.

Uncertainty estimation

For each setting, 20 accumulated spectra are taken. The statistical uncertainty is determined for each setting individually. The uncertainty of the fits given by the software ranges from 2.5 °C to 11 °C. The statistical uncertainty is then determined from the standard deviation of the mean temperature over all 20 spectra which is higher than the mean fit error given by the software. An example of the uncertainty estimation of the fitted rotational temperature for 1 slm helium and 640 ppm feed gas humidity with the fitting uncertainty, mean value and standard deviation is shown in figure A.0.1 in the appendix. Uncertainty resulting from the optics used such as positioning of the lens is not taken into consideration here.

3.2.3 Temperature of jet components

The temperature of the **capillary wall** is measured by placing a type-K thermocouple centrally between the electrodes touching the glass. The temperature is measured at the end of the plasma (0 mm) and at the end of the capillary (10 mm). The powered electrode is positioned so that the voltage supply is attached at the top to reduce any influence of the thermocouple by the electric field. The difference between the temperature with and without applied voltage is below 1 °C for the investigated range of power.

The **electrode temperature** is measured by a Luxtron which is based on fibre-optical temperature determination and therefore insensitive to electric fields. The fibre tip is placed at the bottom side of the electrode next to the capillary.

For all component temperature measurements, the temperature is measured until equilibrium is reached. The mean temperature is then obtained by averaging the measurements over a course of 2 min and the uncertainty is estimated from the standard deviation.

3.3 Laser-induced fluorescence spectroscopy

Laser-induced fluorescence is used to obtain spatial information on the OH density in the effluent. Laser-induced fluorescence spectrometry (LIF) requires calibration of the data to obtain absolute values of densities. Following the setup, the calibration and model used to obtain absolute values are outlined.

3.3.1 Setup for laser-induced fluorescence spectroscopy

The LIF setup consists of two essential components - the laser system, which generates the light at the required wavelength, and the optical system to detect the LIF signal.

Laser system

A laser system consisting of two consecutive lasers is used as a light source.

A neodymium-doped yttrium aluminium garnet (Nd:YAG) laser (Continuum: Powerlite PL9010) is used as a pump laser. It operates at 1064 nm in the infrared regime. The laser runs in Q-Switch mode, which allows for pulse energies of up to 140 mJ at a frequency of 20 Hz and pulse length of (11.5 ± 2.2) ns. The beam

is frequency-doubled by a doubling crystal to generate linearly polarised laser light at 532 nm. Both beams are coupled out of the laser individually, allowing for operation at a 532 nm only which is needed to pump the dye laser.

The laser beam is coupled into a dye laser (Radiant Dyes: Narrowscan) by two mirrors set at an angle of 45° and a 1 cm large blend between both. The dye laser is operated with Rhodamin 6G as a dye which has its maximum efficiency of 30 % at 570 nm and is therefore well suited to generate laser light around 566 nm and frequency-doubled to 283 nm to excite OH molecules to fluorescence. The laser energy of the beam can be adjusted by shifting the delay between the two amplifiers of the Nd:YAG laser. The laser's warm-up time is set to a minimum of 3 h to obtain a stable laser profile.

An external triggering system is implemented for synchronised plasma and laser operation when the plasma is frequency modulated. A schematic sketch of the triggering system is shown in figure 3.3.1. The direction of signal transmission is indicated by arrows.

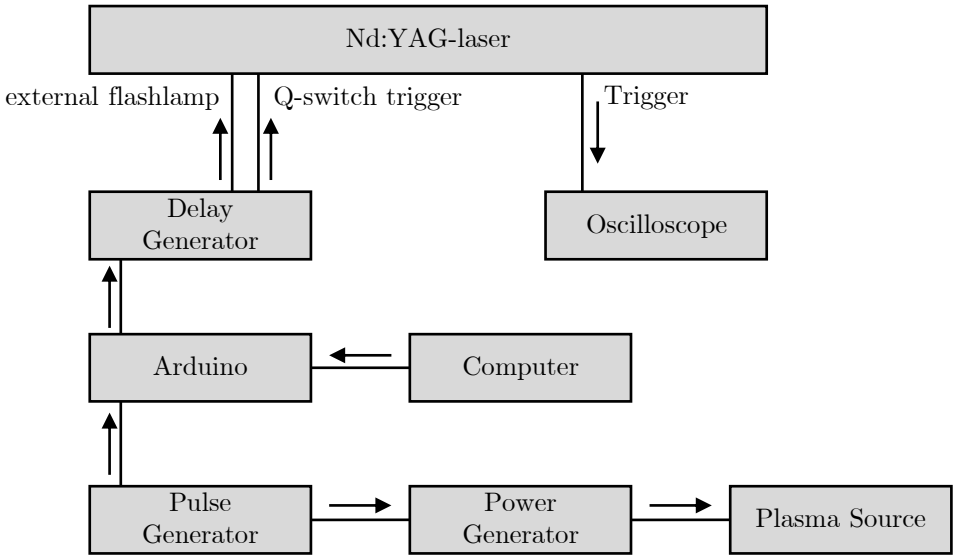

Figure 3.3.1: Schematic sketch of triggering system. Direction of signal transmission is indicated by arrows.

The pulse generator used for frequency modulation of the plasma is connected to an Arduino Duo. The frequency applied to the pulse generator is then modulated to the fixed frequency of 20 Hz of the laser. Therefore, the pulsing frequency slightly deviates from the ones listed in table A.1 and is set to the closest multiple of 20 Hz. The Arduino then gives out a signal to the delay generator (Stanford Research Systems: DG535) at a frequency of 20 Hz with its start time synchronised to the pulse generator pulse. The delay generator then gives out a pulse to the

external flashlamp and Q-Switch trigger. The fixed Sync-Out triggering signal of the laser is used to trigger the oscilloscope for LIF measurements.

Optical system

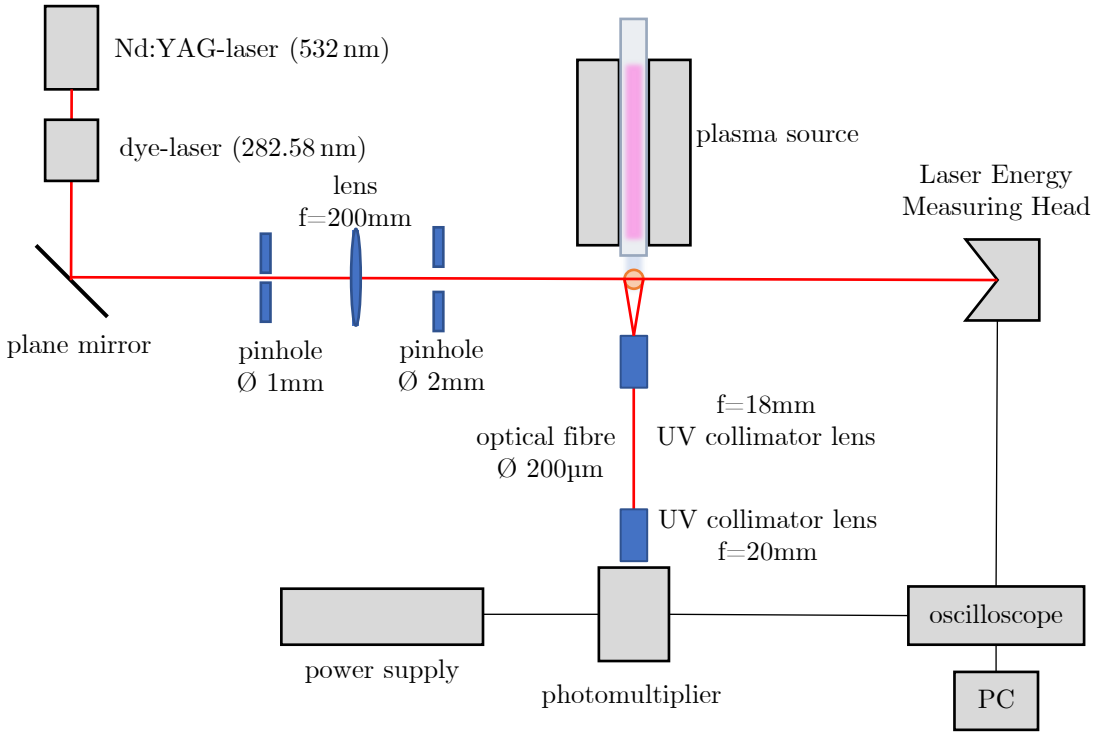

Figure 3.3.2: Schematic sketch of LIF setup.

The setup used for LIF measurements is shown in figure 3.3.2. The laser is projected onto a high reflectance (HR) 250 nm to 320 nm / 45° plane mirror. The beam is cut through a 1 mm round pinhole and hits a BK-7 plano-convex lens with a focal length of 200 mm. A second circular pinhole with a diameter of 2 mm is used to reduce the stray signal. The optics are placed under a closed cover with two holes for the incident and outgoing laser beam to reduce the stray signal of the beam in the laboratory.

The laser energy is measured in the far field of the laser beam with a laser energy measuring head (Sensor- und Lasertechnik: PEM 11) with a calibration factor of $541\,\mathrm{V\,J^{-1}}$. For LIF measurements, the laser energy is held constant at 7.4 µJ corresponding to a voltage signal of the laser energy measuring head of 4 mV. The energy of the laser beam coupled out of the laser is approximately double the amount. Therefore, approximately 50 % of the laser energy is cut off by blends or absorbed by mirrors and lenses.

The capillary jet is mounted to digitally controllable stages (Zaber: X-LSM100A) to allow for precise adjustment of the position of the capillary jet in all three dimensions. The maximum range is 100 mm which is further limited to prevent collisions between the components.

The LIF signal is detected by a 10 mm Aperture Collimator (Edmund Optics) for the UV and visible spectrum with a focal length of 18 mm. The fluorescence signal is projected by the aperture onto a 200 µm UV-VIS optical fibre (Ocean Insight) connected to a UV/VIS Collimating Lens (Ocean Insight) with a focal length of 20 mm suited for wavelengths between 200 nm to 2500 nm. No filter is used to avoid additional corrections for transmission of filter [40]. A photomultiplier is coupled to a power supply (Hamamatsu: C3830) set to -950 V. Matt black textile is used around the setup to reduce reflection of the laser light towards the aperture.

The **alignment of the system** is performed based on the observation of the LIF signal. The capillary jet is adjusted so that the gas flow is perpendicular to the ground. The offset between the position of the peak intensity in the x-y-plane determined 4 mm from the nozzle may not vary more than 0.1 mm over a 10 mm increase in distance. The positioning of the system is readjusted in the x-y-plane by determining the position with maximum LIF signal 4 mm from the capillary end and setting the central position $(0/0)$ here.

Additionally, the Rayleigh signal in pure nitrogen must be in the range of 35 mV to 45 mV peak intensity at (7.4 ± 0.4) µJ which corresponds to the maximum detected signal at the selected settings. If the intensity is lower, the positioning of the collimator lenses and photomultiplier is readjusted. The stray signal in pure helium with plasma turned off is reduced to under 4 mV peak intensity of the photomultiplier signal.

3.3.2 Calibration

The procedure suggested by Verreycken et al. [40] and Morabit et al. [43] to obtain absolute OH densities from LIF intensities via calibration using Rayleigh scattering is performed to calibrate the LIF signal. Determination of absolute densities requires information of the laser parameters as well as setup specific optical parameters. In addition, estimation of the helium-air mixture is required to determine the coefficients of the excitation scheme adequately.

Temporal profile of the laser pulse

The laser pulse length is measured with a diode (AEPX 65) and features a full-width half maximum of (11.5 ± 2.2) ns (see figure 3.3.3). The FWHM is obtained by fitting the curve with a Gaussian curve.

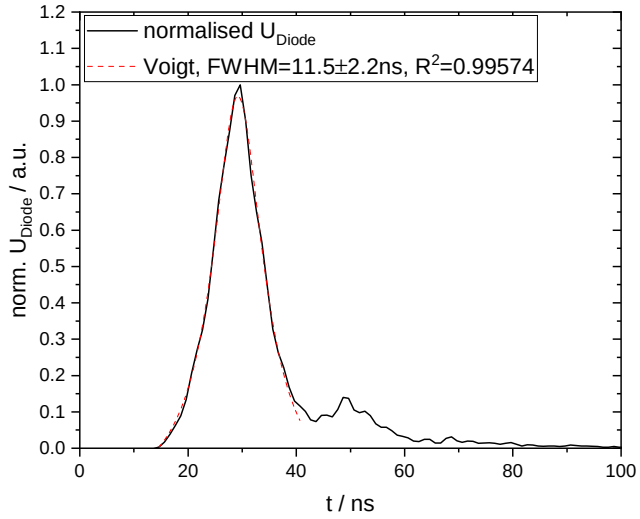

Figure 3.3.3: Laser pulse of Nd:YAG laser measured with AEPX 65 diode fitted with Gaussian curve. Signal averaged over 64 scans.

Spectral profile of laser pulse

The laser is set to a central wavelength $\lambda_{L,0}$ of 282.58 nm as suggested by the aforementioned groups "to excite the $P_1(2)$ transition from the $f_1(2)$ rotational level of OH $X(\nu'' = 0)$ to the $f_1(1)$ rotational level of OH $X(\nu' = 1)$" [43]. This wavelength is favourable as it features one of the largest relative populations regarding all rotational levels in a low temperature regime. In addition, it is clearly separated from neighbouring lines, which is why it does not overlap with other rotational lines [40].

The bandwidth $\Delta\nu_L$ of the laser is $<0.06\,\mathrm{cm}^{-1}$ at 580 nm according to the manufacturer. The maximum estimate of $(0.06 \pm 0.02)\,\mathrm{cm}^{-1}$ was taken for further calculation. The bandwidth of the laser is usually around $0.04\,\mathrm{cm}^{-1}$ according to the manufacturer which is regarded in the uncertainty. The linewidth $\Delta\lambda_L$ of the laser is then 2 pm from the conversion $\Delta\nu_L = \frac{\Delta\lambda_L}{\lambda_{L,0}^2}$ [40]. After frequency doubling, the linewidth is diminished by a factor $2\sqrt{2}$ [40] yielding a linewidth of (0.71 ± 0.24) pm or bandwidth of $(0.089 \pm 0.029)\,\mathrm{cm}^{-1}$.

Overlap Integral

The overlap integral is a measure for the overlap of the spectral profile of the laser $L_{\mathrm{L}}(\nu)$ and the spectral profile of the absorption line $Y_{\mathrm{A}}(\nu)$ depending on the wavenumber ν. When both are normalised to unity, the dimensional overlap integral calculates to [74]

$$g = \int_{-\infty}^{\infty} Y_{\mathrm{A}}(\nu) L_{\mathrm{L}}(\nu)\, \mathrm{d}\nu. \tag{3.10}$$

To obtain the dimensionless overlap integral, the dimensional overlap integral is multiplied by the linewidth of the laser [74] as

$$\Gamma = \Delta\nu_L g \tag{3.11}$$

The spectral profile of the absorption line at wavelength λ can be calculated under the assumption of a Voigt profile from the Doppler ($\Delta\lambda^G$) and van der Waals ($\Delta\lambda^L$) width [75, 76].

$$\Delta\lambda^{\mathrm{G}}(\mathrm{pm}) = 7.16 \cdot 10^{-7} \lambda \sqrt{\frac{T}{M}} \tag{3.12}$$

$$\Delta\lambda^{\mathrm{L}}(\mathrm{pm}) = 1.71 \cdot 10^{-3} \cdot \frac{\lambda^2}{c} \left(\frac{T}{296}\right)^{-0.7} \tag{3.13}$$

The temperature T in Kelvin is obtained from gas temperature measurements (section 4.1) and the atomic mass M of OH is 17 amu.

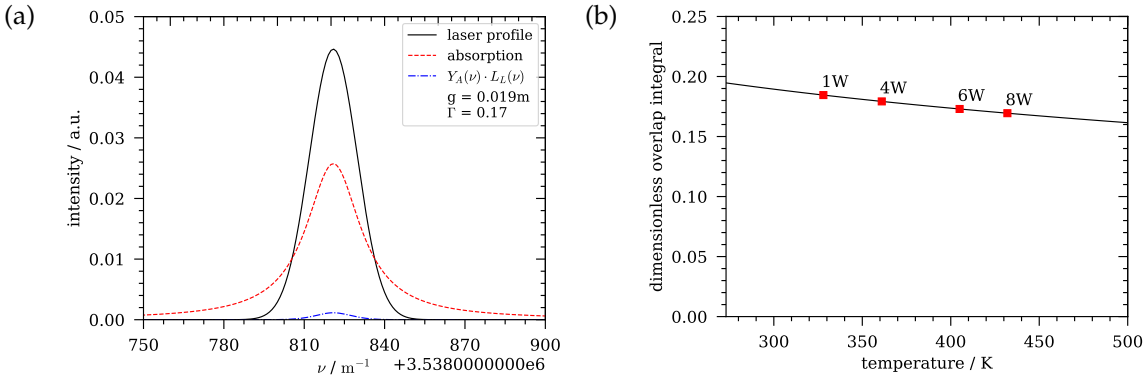

Figure 3.3.4: (a) Laser profile (solid black), absorption profile (dashed red) and overlap (dash dotted blue) depending on the wavenumber for gas temperature of 405 K (measured at 6 W) and (b) dimensionless overlap integral determined from laser and absorption profile for varied gas temperature for central wavenumber of 3 538 820 m^{-1} and 8.9 m^{-1} laser bandwidth.

The absorption and laser profile and the temperature-dependent dimensionless overlap integral are shown in figure 3.3.4. Figure 3.3.4a shows the laser profile, absorption profile and the overlap of both depending on the wavenumber for a temperature of 405 K which was measured at 6 W plasma power. Note that the wavenumber in the plot is given in m^{-1} as the overlap integral is determined in m. The overlap according to equation 3.10 is then 0.019 m. The dimensionless overlap integral (eq. 3.11) then yields a value of 0.17.

The overlap integral is temperature dependent as the absorption profile depends on the gas temperature. It decreases linearly with increasing temperature. The temperature dependence and values for plasma powers in the range of 1 W to 8 W is shown in figure 3.3.4b. In the investigated temperature region, the dimensionless overlap integral decreases from 0.18 to 0.17.

The plasma at 6 W is taken as a reference and the value of 0.17 is a minimum estimate of the overlap integral applied for all plasma settings. Uncertainty is caused by the laser linewidth and temperature change with spatial variation of the observation point in the gas stream.

A change of $0.02\,cm^{-1}$ leads to a decrease of the dimensionless overlap integral to 0.13. Assuming that the laser bandwidth at 580 nm is $(0.06 \pm 0.02)\,cm^{-1}$, this results in a 24 % uncertainty of the dimensionless overlap integral with regard to the uncertainty of the laser bandwidth.

Spatial profile of the laser beam in point of observation

The spatial profile of the laser beam in the point of observation is measured with a camera (Gentec: Beamage-4M) connected to a UV beam converter (Gentec: BSF23RS11.3N) in the focal point of the LIF setup to obtain the spatial FWHM and area of the laser beam. In addition, this allows control of the beam profile which is aimed to be Gaussian [63]. The measurements are shown in figure 3.3.5

The Gaussian fit yields a full width half maximum of (58.13 ± 0.28) nm in y-direction ($R^2 = 0.9995$) and (62.4 ± 0.6) nm in z-direction ($R^2 = 0.9983$). The uncertainty given here is the one resulting from the fit. Taking into consideration the adjustment of the camera around the focal point and the resolution of the camera of $7.7\,\mu m\,pixel^{-1}$, the uncertainty of the spatial FWHM is expected to be in the order of 10 µm. For further calculations, the mean FWHM of both directions and the uncertainty resulting from spatial resolution and adjustment are regarded, resulting in a spatial FWHM of (60 ± 10) µm.

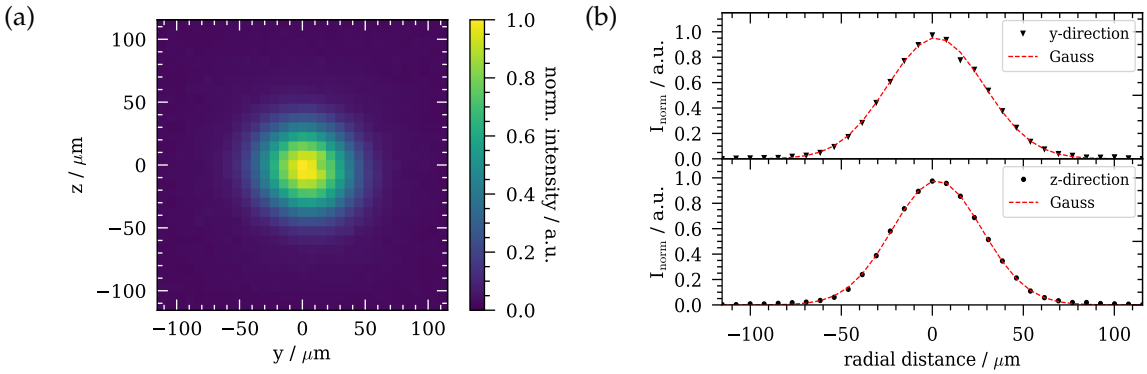

Figure 3.3.5: Spatial imaging (a) of the laser spot in the yz-plane and (b) of the profile of the laser spot in y- and z-direction with Gaussian fit for (7.4 ± 0.4) µJ laser energy in the focal point of the LIF setup with a spatial resolution of 7.7 µm pixel^{-1}.

Laser energy

The mean laser energy averaged over 128 pulses is set to (7.4 ± 0.4) µJ during the measurement. The laser energy of the single pulses varies by up to 25 % in the investigated laser energy region.

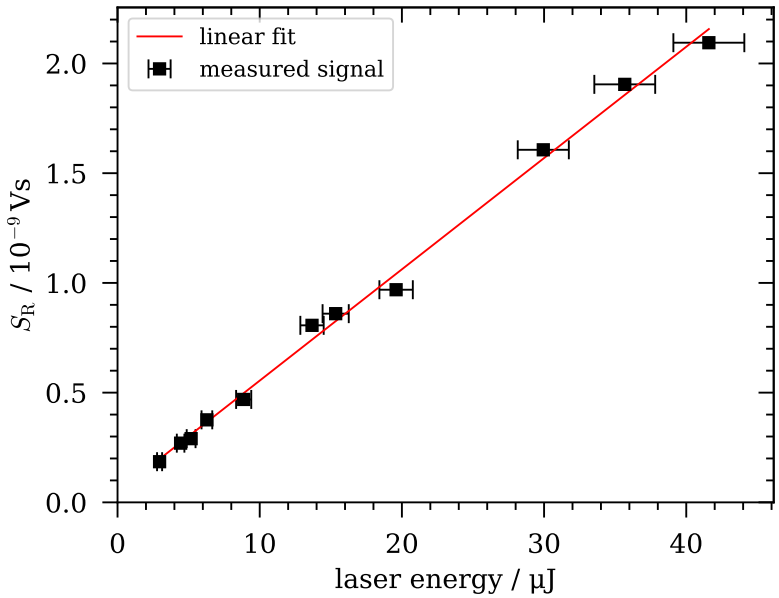

Figure 3.3.6: Rayleigh signal for varied laser energy with a linear fit.

The system may not be operated in saturation. To check for saturation effects, the intensity of the Rayleigh signal is detected up to 40 µJ and a linear fit is applied to the temporally integrated signal depending on the laser energy (figure 3.3.6. No deviation from the linear behaviour can be observed and the linear fit yields an R^2 value of 0.995. Typically, laser energies up to 10 µJ are used in LIF measurements. Therefore, operation at (7.4 ± 0.4) µJ in the linear regime is in good agreement with literature [43, 63].

Detection volume

The spatial resolution of the system and thus width of the detection volume is determined by the optical fibre used in the setup. In this case, the length and width of the detection volume are both (200 ± 4) µm. Preliminary measurements performed in the master thesis of Pia Pottkämper have verified the correspondence between optical resolution and diameter of the optical fibre [77].

Efficiency of the optics' fluorescence detection

The calibration factor for the LIF measurements accounting for the efficiency of the optics' fluorescence detection is estimated from the Rayleigh signal [40]. Molecular nitrogen (N_2) is used for the calibration as the Rayleigh cross-section is known from literature.

The measured Rayleigh scattering intensity is determined by a calibration constant η depending on the solid angle and efficiency of the detector used, the density of scatterers N_n, the differential cross-section for Rayleigh scattering of the surrounding gas $\partial^{\beta=0}\sigma_0/\partial\Omega$, the volume V_R from which the signal is collected, the laser irradiance I_L and the temporal length of the laser pulse t_L [40]. The Rayleigh signal then calculates to

$$S_\mathrm{R} = \eta \cdot N_\mathrm{n} \cdot \frac{\partial^{\beta=0}\sigma_0}{\partial\Omega} V_\mathrm{R} I_\mathrm{L} t_\mathrm{L}. \tag{3.14}$$

At room temperature, the density of the scattering particles can be calculated from the ideal gas law to

$$N_\mathrm{n} = \frac{p}{k_\mathrm{B}T}. \tag{3.15}$$

Here, p is the pressure and $k_\mathrm{B}T$ is the product of the Boltzmann constant and temperature [K]. The differential cross-section for Rayleigh scattering in molecular nitrogen has been found to be $8.8\,\mathrm{m^2\,sr^{-1}}$ [40].

The laser irradiance can be expressed in terms of laser energy E_L as

$$I_\mathrm{L}(y,z,t) = \frac{E_\mathrm{L}}{\tau_\mathrm{L}\Delta s^2} \cdot f_\mathrm{s}(y,z) f_\mathrm{t}(t) \tag{3.16}$$

where τ_L is the temporal full width at half maximum (FWHM) of the laser pulse and s the spatial FWHM in the observation point. Assuming a non-uniformity in space and time of the laser, the spatial distribution $f_\mathrm{s}(y,z)$ of the energy density

and time variation $f_t(t)$ of the energy are taken into consideration [40]. Accordingly, equation 3.14 becomes

$$\begin{aligned} S_R &= \eta \cdot N_n \cdot \frac{\partial^{\beta=0}\sigma_0}{\partial\Omega} E_L \frac{1}{\tau_L \Delta s^2} \cdot \int_0^{\Delta x} \int_{-\infty}^{+\infty} \int_{-\infty}^{+\infty} \int_0^{\infty} f_s(y,z) f_t(t)\, \mathrm{d}x\, \mathrm{d}y\, \mathrm{d}z\, \mathrm{d}t \\ &= \eta \cdot N_n \cdot \frac{\partial^{\beta=0}\sigma_0}{\partial\Omega} E_L \Delta x. \end{aligned} \tag{3.17}$$

Here, Δx is the length of the detection volume.

The calibration constant η then is a factor that takes the solid angle and the detector efficiency into account [40, 78]. It calculates to

$$\eta = \alpha k_B T \frac{\partial^{\beta=0}\sigma_0}{\partial\Omega} \Delta x. \tag{3.18}$$

It can be obtained from the slope α of the linear fit $f(E_L) = \alpha E_L p + S_0$ of the Rayleigh signal plotted against the product of laser energy E_L and pressure p. The offset S_0 of the linear fit results from the detected stray signal.

For experiments in atmosphere, the laser energy is varied. Comparisons between Rayleigh calibration with varied pressure and varied energy were in good agreement for measurements performed on the COST-jet in an enclosed vacuum chamber using the same optical setup [private communication with Sebastian Burhenn].

1 slm nitrogen is used to obtain a pure nitrogen atmosphere for calibration. The signal is measured centrally in the gas stream 4 mm underneath the capillary end where there is neither any scattered signal nor any quenching partners from ambient air inside the gas stream. Validation of the positioning is performed by checking the LIF signal in 1 slm helium with plasma turned off. As helium has a negligible Rayleigh cross section, no Rayleigh signal should be detectable. A signal close to zero is therefore used as validation that no ambient air is present in the gas stream.

The Rayleigh signal is then measured for laser energies varying from (2.7 ± 0.4) µJ to (44.4 ± 1.8) µJ. The calibration has been performed several times. The pressure is assumed to be constant at 1 bar. Daily air pressure fluctuations occur but are around 20 mbar and have minor influence on the calibration.

The Rayleigh calibration data is shown in figure 3.3.7. The Rayleigh signal S_R is calculated by integration over the whole signal to account both for signal intensity and signal decay time. An exemplary calibration curve is shown in figure

3.3.7a. The fit with a linear function yields a R^2 value of 0.998 indicating that saturation has not been reached yet.

The day-to-day comparison is shown in figure 3.3.7b. Each calibration is performed from data taken from at least ten different laser energies. Except for calibration number 2, the calibration yields very similar results, even after readjusting the setup. Therefore, the system is considered to be both stable and reliable and does not depend on minor pressure or humidity changes in the atmosphere. Calibration number 2 was measured after a weekend. The deviation could result from humidity in the gas supply that accumulated over the time the setup was not in use and was not sufficiently removed during flushing the setup.

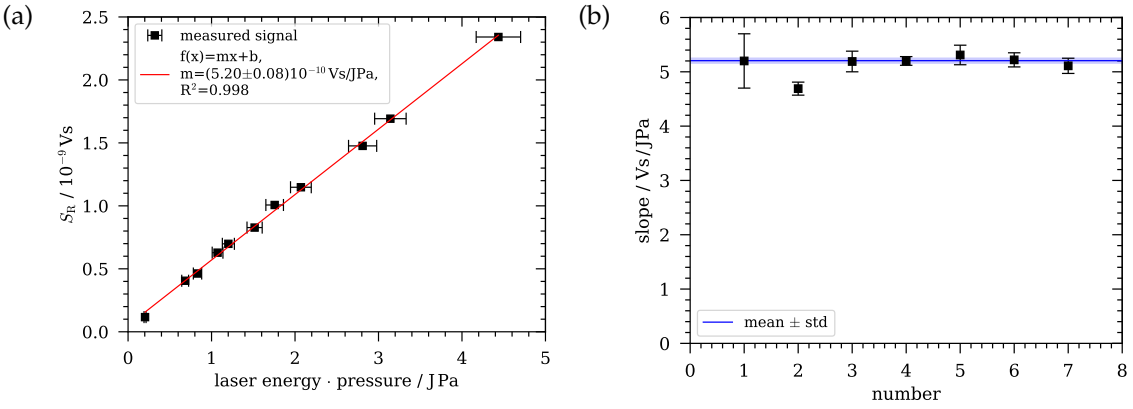

Figure 3.3.7: Rayleigh calibration performed in pure nitrogen at a gas flow rate of 1 slm at central position of the gas stream 4 mm from the nozzle. (a) Calibration of LIF signal by means of the Rayleigh signal taken for varied laser energy at constant pressure of 1 bar. (b) Day-to-day comparison of slope obtained from Rayleigh calibration. Second calibration is not taken into consideration for mean slope (grey line).

The mean calibration factor without taking the value of calibration number 2 into consideration is $(5.20 \pm 0.07) \times 10^{-10}\,\mathrm{V\,s\,J^{-1}\,Pa^{-1}}$. The calibration constant η (equation 3.18) then equates to

$$\eta = (12000 \pm 500)\,\mathrm{V\,sr\,J^{-1}} \tag{3.19}$$

at a room temperature of $(21.4 \pm 0.5)\,^{\circ}\mathrm{C}$, differential Rayleigh cross section of $8.8 \times 10^{-31}\,\mathrm{m\,sr^{-2}}$ [40] and length of the detection volume of $(200 \pm 4)\,\mu\mathrm{m}$.

3.3.3 Calculation of absolute values

An overview of the setup-specific parameters needed for absolute calibration is given in table A.3 in the appendix.

The measured LIF signal intensity can be expressed in terms of the integral [79]

$$S_{\mathrm{LIF}} = \frac{1}{4\pi} \int \eta \frac{hc}{\lambda} n_{\mathrm{exc}}(x, y, z, t) A \, \mathrm{d}x \, \mathrm{d}y \, \mathrm{d}z \, \mathrm{d}t \tag{3.20}$$

with the density of OH radicals in the excited state $n_{\mathrm{exc}}(x, y, z, t)$ at wavelength λ and Einstein coefficient A of the observed transition [40]. The normalised density N_{i} is then obtained from the ratio of the density in the excited state i and density in the ground state n_{OH} via

$$N_{\mathrm{i}} = \frac{n_{\mathrm{exc,i}}}{n_{\mathrm{OH}}} \tag{3.21}$$

and calculated from a model for the different levels.

For laser energies in the linear regime, rotational energy transfer (RET) reactions can be neglected [63]. RET is assumed to be infinitely fast in comparison to vibrational energy transfer (VET), quenching and emission. For this case, Verreycken et al. [40] suggest a 4-level model of differential equations including laser excitation from ground level to stimulated emission, vibrational energy transfer (VET) as well as electronic energy transfer (Q) reactions. Comparison to a 6-level model including RET has shown, that this assumption is valid for the regarded parameters [40].

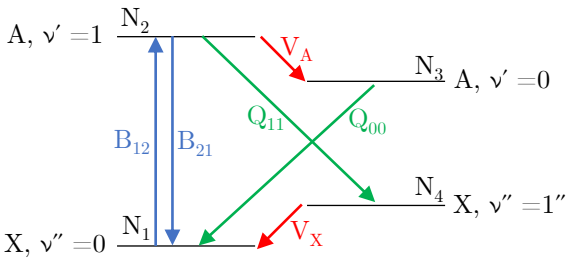

Figure 3.3.8: Scheme of radiative and collisional processes regarded in 4-level model [40].

The transitions that are included in the model are shown in figure 3.3.8. As only the vibrational levels $\nu = 0{,}1$ are taken into consideration, VET from $\nu = 1$ to $\nu = 0$ is implemented in the model. Stimulated emission originating from the $F_1(1)$ level is expressed by the Boltzmann factor $f_B^{\nu'=1,J'=1.5}$ [40].

For absolute densities, the correct representation of the level structure of the OH($X^2\Pi$) state must be considered [80]. In this state, Λ-doubling occurs re-

sulting in splitting of the rotational levels to f_1, f_1', f_2 and f_2'. If Λ-doubling is neglected, this results in an underestimation of factor two in the densities. The concentration of the OH radicals in the ground state is then determined from the OH radicals in the rotational level J'' as

$$N = \frac{N_{J''}}{f_{J''}} = N_{J''} \left(\frac{(2J''+1)}{2Q_{\mathrm{rot}}(T)} \exp\left(-\frac{E_i}{kT}\right)\right)^{-1} \tag{3.22}$$

with energy $E_{J''}$ of rotational level J'', the rotational partition function $Q_{\mathrm{rot}}(T)$, Boltzmann constant k and rotational temperature T [80, 81].

The following system of ordinary differential equations describes the model [40]:

$$\begin{aligned}\frac{dN_1}{dt} = {} & f_{\mathrm{t}}(t) I_{\mathrm{S}} \left(-B_{12} f_{\mathrm{B}}^{\nu''=0,J''=2.5} N_1 + B_{21} f_{\mathrm{B}}^{\nu'=1,J'=1.5} N_2 \right) \\ & + A_{10} N_2 + L_0 N_3 + V_{\mathrm{X}} N4\end{aligned} \tag{3.23}$$

$$\begin{aligned}\frac{dN_2}{dt} = {} & f_{\mathrm{t}}(t) I_{\mathrm{S}} \left(B_{12} f_{\mathrm{B}}^{\nu''=0,J''=2.5} N_1 - B_{21} f_{\mathrm{B}}^{\nu'=1,J'=1.5} N_2 \right) \\ & - L_1 N_2\end{aligned} \tag{3.24}$$

$$\frac{dN_3}{dt} = V_{\mathrm{A}} N_2 - L_0 N_3 \tag{3.25}$$

$$\frac{dN_4}{dt} = (A_{11} + Q_{11}) N_2 - V_{\mathrm{X}} N_4 \tag{3.26}$$

where N_{i} is the population of level i, B_{ij} the Einstein coefficient B from level i to j and $f_B^{\nu,J}$ the temperature-dependent Boltzmann factor of the level with vibrational level ν and total angular momentum J. Energy transfer is determined by vibrational energy transfer rate in ground rate V_{A} and vibrational energy transfer rate in excited state V_{X}. A_{ij} is the Einstein coefficient from vibrational level and Q_{ij} the quenching rate in ground state.

Regarding collisional quenching, it is assumed that both rotational and vibrational number are conserved. Other spontaneous emission than A_{11}, A_{10} and A_{00} are not considered as they are more than two orders smaller in magnitude [40].

The loss processes at vibrational level ν are determined by L_ν.

$$L_0 = Q_{00} + A_{00} \tag{3.27}$$

$$L_1 = Q_{11} + A_{11} + A_{10} + V_{\mathrm{A}} \tag{3.28}$$

The gas admixture in the effluent must be regarded in the loss processes. While the feed gas consists of helium and water vapour, intrusion of ambient air into the effluent also brings N_2, O_2 and additional H_2O into the effluent which then adds to the loss processes by additional quenching [78].

The feed gas mixture is known from the settings of the bubbler. In the laboratory, a mean temperature of $(21.4 \pm 0.2)\,^{\circ}\mathrm{C}$ and relative humidity of $(25 \pm 5)\,\%$ is given. This results in about 0.76 % water vapour in the ambient atmosphere. A fraction of 78.24 % N_2 and 21 % O_2 is assumed for the air mixture. All other trace gases are neglected.

The admixture can then be determined from the decay time τ of the measured LIF signal after the decay of the laser pulse as

$$Q_{ij} = \frac{1}{\tau_{ij}} \tag{3.29}$$

$$L_i = \frac{1}{\tau_i} \tag{3.30}$$

As the fitted decay time τ of the measured data results from the superposition of the 1-1 and 0-0 decay, an analytical approximation of the decay time is performed. Minimisation of the residual between normalised measured LIF signal and normalised modelled signal after the decay of the laser pulse is used to determine quenching. From the best fit, the amount of air in the admixture is deduced.

The loss processes (eq. 3.27 and 3.28) with regard to the particles n in the regarded volume then compute to

$$\begin{aligned} L_0 = {} & n \cdot F_{\mathrm{fg}} \cdot (Q_{00,\mathrm{He}} \cdot f_{\mathrm{He}} + Q_{00,\mathrm{H_2O,fg}} \cdot f_{\mathrm{H_2O,fg}}) \\ & + n \cdot F_{\mathrm{air}} \cdot (Q_{00,\mathrm{N_2}} \cdot f_{\mathrm{N_2}} + Q_{00,\mathrm{O_2}} \cdot f_{\mathrm{O_2}} + Q_{00,\mathrm{H_2O,air}} \cdot f_{\mathrm{H_2O,air}}) \\ & + A_{00} \end{aligned} \tag{3.31}$$

$$\begin{aligned} L_1 = {} & n \cdot F_{\mathrm{fg}} \cdot (Q_{11,\mathrm{He}} \cdot f_{\mathrm{He}} + Q_{11,\mathrm{H_2O,fg}} \cdot f_{\mathrm{g}}) \\ & + n \cdot F_{\mathrm{air}} \cdot (Q_{11,\mathrm{N_2}} \cdot f_{\mathrm{N_2}} + Q_{11,\mathrm{O_2}} \cdot f_{\mathrm{O_2}} + Q_{11,\mathrm{H_2O,air}} \cdot f_{\mathrm{H_2O,air}}) \\ & + A_{11} + A_{10} \\ & + n \cdot F_{\mathrm{fg}} \cdot (V_{\mathrm{A,He}} \cdot f_{\mathrm{He}} + V_{\mathrm{A,H_2O,fg}} \cdot f_{\mathrm{H_2O,fg}}) \\ & + n \cdot F_{\mathrm{air}} \cdot (V_{\mathrm{A,N_2}} \cdot f_{\mathrm{N_2}} + V_{\mathrm{A,O_2}} \cdot f_{\mathrm{O_2}} + V_{\mathrm{A,H_2O,air}} \cdot f_{\mathrm{H_2O,air}}) \end{aligned} \tag{3.32}$$

At room temperature and 1 bar atmospheric pressure, the particle density accounts to $2.4 \times 10^{25}\,\mathrm{m}^{-3}$ according to the ideal gas law $pV = nk_{\mathrm{B}}T$.

The quenching rate coefficients Q_{ii} and VET rates V_A for the collision partners are listed in table A.4 in the appendix. Further coefficients used in the model are listed in table A.5 in the appendix.

The laser spectral irradiance is calculated as

$$I_S = \frac{E_L \cdot \Gamma}{\Delta\nu_L \tau_L A_L}. \tag{3.33}$$

The LIF signal (equation 3.20) equates to

$$S_{LIF} = \underbrace{\frac{1}{4\pi}\eta hc\Delta x\Delta y\Delta s}_{k} n_{OH} \cdot \int \left(N_2(t) \left(\frac{A_{11}}{\lambda_{11}} + \frac{A_{10}}{\lambda_{10}} \right) + N_3(t) \frac{A_{00}}{\lambda_{00}} \right) \mathrm{d}t \tag{3.34}$$

according to [40].

As the only unknown is n_{OH} now, the absolute density is obtained from comparison of the measured LIF signal S_{LIF} and modelled LIF signal with the setup-dependent constant k.

$$n_{OH} = \frac{S_{LIF}}{k \cdot \int \left(N_2(t) \left(\frac{A_{11}}{\lambda_{11}} + \frac{A_{10}}{\lambda_{10}} \right) + N_3(t) \frac{A_{00}}{\lambda_{00}} \right) \mathrm{d}t} \tag{3.35}$$

The intensity of the measured and modelled LIF signal is calculated from integration over the signal after the laser pulse determined from the Rayleigh signal has decayed under 5 %.

The measured photomultiplier LIF signal is fitted with two overlapping extreme value distribution functions for the LIF signal and noise. Only the fit of the LIF signal is further used to determine the absolute values of the OH density and obtain the air admixture. An example of the normalised fitted OH LIF signal and normalised modelled LIF signal at 6 W plasma power, 640 ppm feed gas humidity and 1 slm gas flow rate 4 mm from the capillary end is shown in figure 3.3.9. Air intrusion is neglected at this point in the gas stream. The time point where the laser signal has decayed below 5 % is named t_{start}. One can clearly see that the modelled LIF signal matches the fit of the measured signal very well. Slight deviation is only present during excitation by the laser.

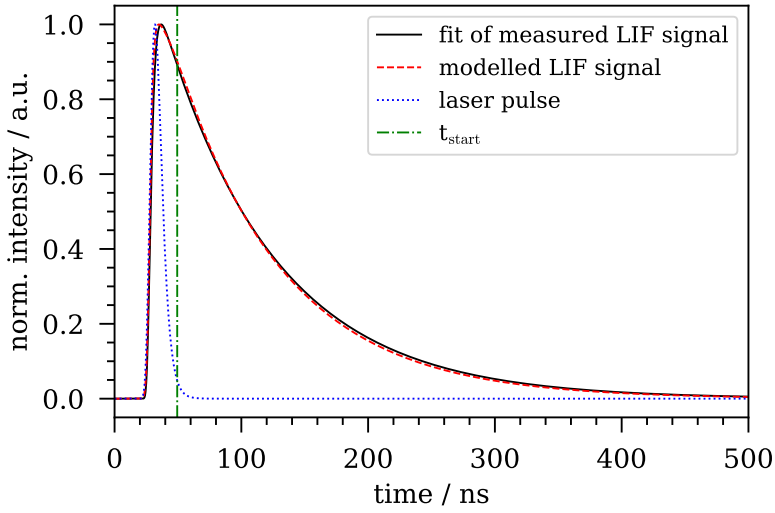

Figure 3.3.9: Normalised fit of measured LIF signal (black solid) and modelled LIF signal (red dashed) at (640 ± 30) ppm feed gas humidity, 6 W plasma power and 1 slm gas flow rate 4 mm from the capillary end without air intrusion at observation point. Laser pulse (blue dotted) obtained from Rayleigh signal.

Uncertainty estimation

The uncertainty of the measurements is dependent on the LIF signal's stability at a constant setting and on the uncertainty of the individual parameters going into the calibration of the signal for absolute values. In addition, uncertainty about the gas admixture causes uncertainty of the quenching and VET rates in the model. The model itself is an additional simplification of the process, which also adds to the total uncertainty.

For the uncertainty estimation, the uncertainty of the experimentally determined parameters is estimated. The uncertainty of the laser spectral irradiance is calculated from propagation of uncertainty which causes a total uncertainty of 91 %.

The laser spectral irradiance mostly influences the shape of the modelled signal before the decay. The intensity of the modelled signal is not heavily influenced by the uncertainty of the laser spectral irradiance. The uncertainty of the model is highly dependent on the measured LIF signal and varies with the varied parameters which also influence quenching. For a high LIF intensity and long fluorescence decay time, the signal is large. In this case, the parameters influencing the spectral irradiance only have a slight impact ($<$2 %) on the calculated OH density. Instead, the uncertainty of quenching is the dominating factor. For low LIF signals, especially for short decay times, the effect of the uncertainty of the laser spectral irradiance increases. Thus, a global uncertainty estimation of the model is challenging as a set of coupled differential equations is used to determine the modelled LIF signal. Only parameters that are included in the calibration factor

k and not in the ODEs have a set influence on the OH density. Instead of a global uncertainty estimation, the estimation in the following is to set out a frame within which uncertainty ranges.

The uncertainties of the individual parameters of the values and their impact on the OH density are listed in table 3.2. The exemplary evaluation is based on the analysis of the impact of the uncertainty of the individual parameters on the OH density obtained for 6 W plasma power, 1 slm gas flow rate and 640 ppm and 6400 ppm feed gas humidity for comparison.

Table 3.2: Experimentally determined parameters with uncertainty and impact of uncertainty on the OH density for low and high feed gas humidity.

Parameter	Uncertainty	Impact on n_{OH}	
		640 ppm	6400 ppm
τ_L	20 %	<1 %	2.8 %
$\Delta\nu$	30 %	1 %	5 %
Γ	24 %	1.2 %	5 %
E_L	6 %	<1 %	<1 %
A_L	18 %	1 %	4 %
I_s	91 %	1.8 %	7 %
Δx, Δy	<1 %	2 %	
Δs	17 %	15 %	
η	5 %	5 %	
$F_{fg,4mm}$	0.1 %	20 %	6 %
$S_{LIF,4mm}$	3 %	3 %	
$S_{LIF,14mm}$	12 %	12 %	

The largest impact on the OH density results from the laser spectral irradiance with laser pulse length, overlap integral and laser bandwidth such as laser energy for high admixtures to the helium feed gas. Moreover, the amount of feed gas at the point of observation causes significant uncertainty in the absolute number density, which becomes more important for low admixtures to the helium flow.

In addition to the discussed experimental parameters, further uncertainty is caused by the accuracy of the quenching and VET coefficients. Furthermore, the Boltzmann factor was assumed to be constant for simplification. In reality, it is temperature-dependent and thus causes additional uncertainty. Potential nonlinear effects can also add to the accuracy of the calibration [40]. Verreycken et al. [40] estimate these two to 20 % and 10 %. As a similar temperature range and working parameters are used in this work, these values are taken as a reference. In addition, the uncertainty increases with decreasing OH density and increasing air admixture [78]. In total, the accuracy of the absolute OH density due to the LIF calibration is expected to be in the order of a factor of 2. For reference, Verreycken

et al. [82] have found an accuracy of 170 % for the absolute OH density.

The reproducibility of the OH LIF signal is determined from three measurements on different days at 6 W plasma power, 640 ppm feed gas humidity and 1 slm gas flow rate. The calculated OH density 4 mm from the capillary end accounts to $9.27 \times 10^{14}\,\mathrm{cm}^{-3}$, $9.53 \times 10^{14}\,\mathrm{cm}^{-3}$ and $9.94 \times 10^{14}\,\mathrm{cm}^{-3}$. The mean value and standard deviation are then $(9.58 \pm 0.28) \times 10^{14}\,\mathrm{cm}^{-3}$ which corresponds to an uncertainty of 3 %. The calculated OH density 14 mm from the capillary end accounts to $4.5 \times 10^{14}\,\mathrm{cm}^{-3}$, $5.8 \times 10^{14}\,\mathrm{cm}^{-3}$ and $5.6 \times 10^{14}\,\mathrm{cm}^{-3}$. The mean value and standard deviation are then $(5.3 \pm 0.6) \times 10^{14}\,\mathrm{cm}^{-3}$ which corresponds to an uncertainty of 12 %. Reproducibility is given at both distances but uncertainty increases with distance. The discussion of the calculated absolute values of the OH densities is performed in the results.

3.4 Fourier-transform infrared spectroscopy

In the following, the setup will be described first. Subsequently, the fitting routine and uncertainty estimation is presented.

3.4.1 Setup for Fourier-transform infrared spectroscopy

Fourier-transform infrared spectroscopy is used to detect infrared-active species in the far-field of the effluent. As the H_2O_2 signal is very weak, a multipass cell based on White's optics is used to increase the absorption length.

A schematic sketch of the setup used for FT-IR measurements is shown in figure 3.4.1. The capillary is connected to the White multipass cell via a 300 mm long Viton tube sealed with Ceramabond (T-E-Klebetechnik) to the capillary end. The tubing is connected to a stainless steel tube that leads to the multipass cell using a Swagelok adapter. The Viton tube reduces the drag on the capillary and allows for correct adjustment of the setup. The length of the Viton tubing is chosen to be just long enough to allow for reduction of any drag or pull on the capillary that could cause breakage and allow for strain-relieved adjustment. Stainless steel tubing (1 m) is chosen for the rest of the connection as it reduces the risk of interaction with the walls and can easily be connected to the multipass cell.

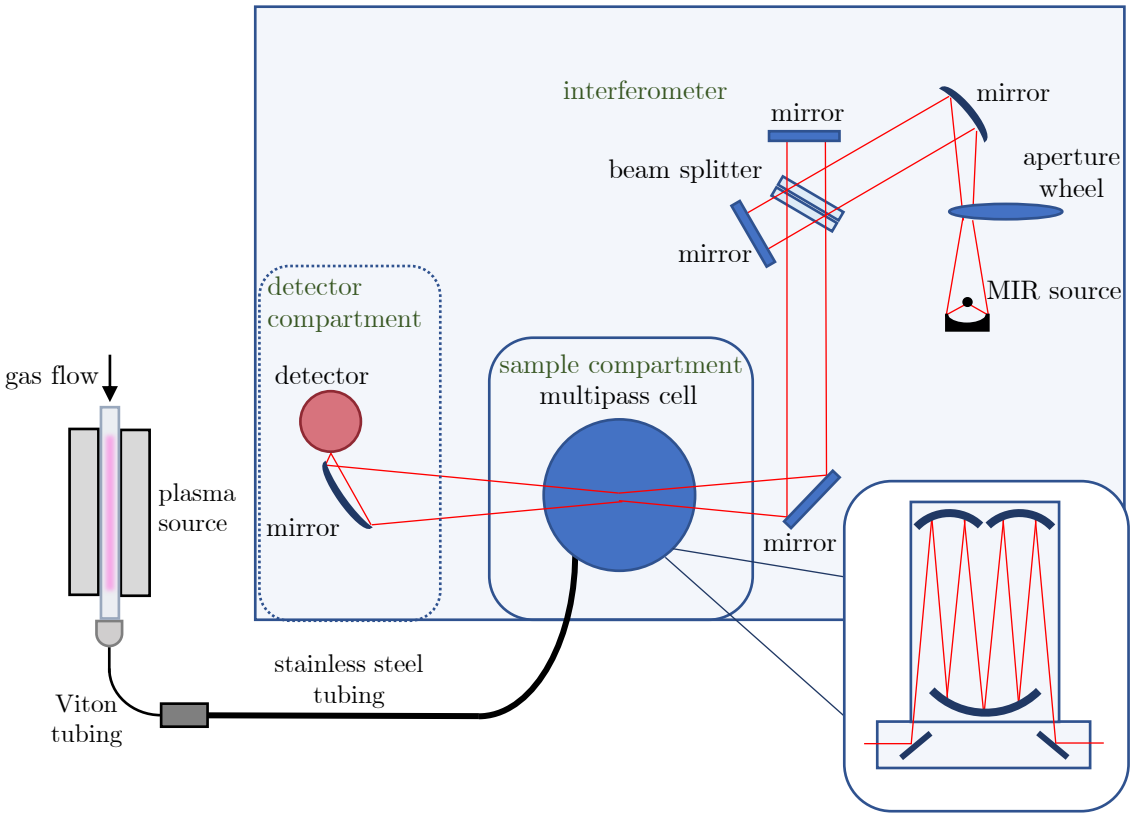

Figure 3.4.1: Schematic sketch of FT-IR setup with optical beam path in FT-IR (Bruker V70) equipped with multipass cell in sample compartment. Detailed view of beam path in multipass cell shown in zoom window (bottom right). Figure of FT-IR and detailed multipass cell adapted from [83].

The FT-IR spectrometer (Bruker: Vertex 70v) is based on a Michelson interferometer. The light is provided by a mid-infrared source. The beam passes an aperture and hits a mirror. The interferometer consists of a fixed and movable mirror as well as a beam splitter. The beam passes the interferometer and is reflected by a third mirror into the multipass cell (Bruker Optics) which is fitted into the sample compartment of the FT-IR spectrometer. The multipass cell consists of two plane mirrors to couple the beam into and out of the cell. In the cell, one mirror is fixed at the bottom and two variable mirrors are placed at the top. By tilting the top mirrors with a micrometer screw, the absorption length is adapted. The beam coupled out from the multipass cell is then reflected by a mirror onto the liquid nitrogen cooled detector.

The absorption length can be varied from 0.8 m to 8 m and is set to 7.2 m (11.97 mm screw position) for all measurements. Here, the signal is strong and optical transmission is not reduced to the point where the total signal is too small.

The space between FT-IR and multipass cell is sealed with double-layered foil and continuously flushed with 500 sccm nitrogen to reduce any residue and back-

ground noise. Additionally, silica gel is placed in three containers inside the sample compartment to absorb any left moisture. Therefore, the beam path is mainly filled with infrared inactive nitrogen. A heating blanket set to 60 °C is used around the multipass cell to reduce the number of species sticking to the walls. As the cell is also used for measurements with ammonia, this is important to reduce any residue and obtain a constant background. The cooling of the detector is refilled every 4.5 h to ensure a constant signal.

In preparation for the measurements, the heating blanket is turned on one hour before measurements. The surrounding chamber was filled with nitrogen for a minimum of 20 min before taking the background scan. Also, the chamber was flushed with helium to reduce any residue and background noise. The signal was continuously checked until the absorption signal was stable. Then, a background scan with the examined gas mixture was performed without plasma. Background scans are taken after every change in the gas composition. A wait time of a minimum of 10 min is regarded after changing the gas composition.

All measurements are performed with 300 accumulations if not otherwise stated. A wait time of 12 min for the scans is ensured to reach steady-state.

3.4.2 Fitting routine

The transmission spectra are fitted based on the spectral data in the HITRAN database [84]. Fitting is performed automatically based on error minimisation. A reference spectrum is altered in terms of density and wavelength shift to fit the data. Fitting of H_2O_2 is performed in the region of 1100 cm^{-1} to 1350 cm^{-1}.

An example of a measurement of the H_2O_2 absorption signal at 6 W plasma power, 6400 ppm feed gas humidity and 1 slm gas flow rate with simulated H_2O_2 signal and underlying Gaussian curve is shown in figure 3.4.2. The residual is shown in the bottom graph. Only the regarded data points are considered in the residual. One can see that the fit matches the measured H_2O_2 signal very well.

Baseline correction is performed prior to the spectrum fit to reduce the tilt of the baseline. A linear fit is applied to the data based on the mean baseline values in the region of 950 cm^{-1} to 1000 cm^{-1} and 2450 cm^{-1} to 2550 cm^{-1} as no absorption lines are present here. The baseline is then tilted to horizontal over the whole spectral range. An additional distortion of the baseline in the region of the H_2O_2 signal is present which has a Gaussian distribution. This may originate from deposition on surfaces as several molecules with C-O bonds feature C-O stretching vibrations here.

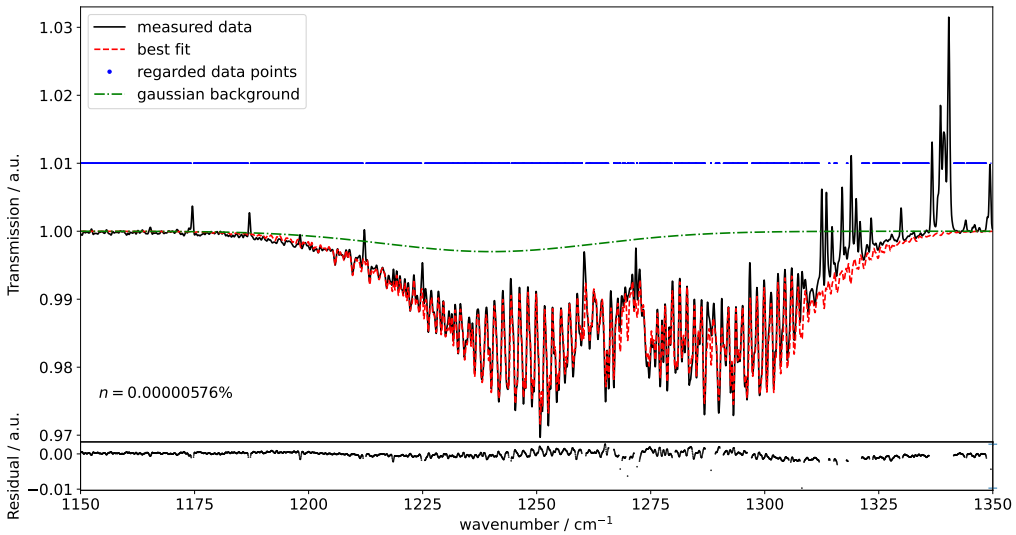

Figure 3.4.2: Measured H_2O_2 FT-IR spectrum (black solid) with fitted spectrum (red dashed), Gaussian baseline (green dash-dotted) and regarded data point of measured spectrum without H_2O lines (blue dots). Spectrum taken for 6400 ppm feed gas humidity, 6 W plasma power and 1 slm gas flow rate.

The Gaussian-shaped signal underneath the H_2O_2 signal is fitted simultaneously with the spectrum. Line broadening is held constant during the fitting routine to improve computation.

As the absorption signal of water interferes with the signal of H_2O_2 in the spectrum, selection of regarded data points is performed. The spectral lines of the water signal are obtained from a reference spectrum. If spectral lines in the transmission spectrum pass a threshold of 2 % of the line intensity of the reference spectrum in positive direction, the data points in this region are not regarded in the fitting process.

The fitting routine then yields the concentration c relative to 100 % of the particles in the gas for an absorption length of 720 cm. The density ρ at room temperature is then calculated from the relation

$$\rho = c \cdot 2.4 \cdot 10^{25} \mathrm{m}^{-3}. \tag{3.36}$$

Uncertainty estimation

The uncertainty of the FT-IR fits depends on several parameters. The pressure inside the multipass cell is assumed to be constant at atmospheric pressure and fluctuations of the pressure are regarded negligible. The absorption length is one major determinant. It is determined by the settings of the screw and given by the calibration sheet. Widening of the beam may lead to additional loss of intensity

leading to a slight underestimation of the species density inside the multipass cell. As the optics are not changed, this causes a constant factor in the species densities, the trends are not influenced by this underestimation.

Additionally, adsorption of H_2O_2 on the walls of the multipass cell can significantly lower the number of H_2O_2 molecules in the beam path. Thus, this adds to the reduction of the measured density in the multipass cell. At a constant gas flow, equilibrium between flux of H_2O_2 to the walls contributing to adsorption and flux through the multipass cell sets in. Thus, the measured H_2O_2 density is diminished by a constant factor at a constant gas flow rate. The trend is not influenced by this. For varied gas flow rate, the equilibrium between flux to wall and through multipass cell changes and hence, no constant factor can be assumed anymore and the trend can be significantly altered.

The reproducibility of the H_2O_2 density at a constant plasma setting is determined by measuring the H_2O_2 density three times with plasma turned off in between and the chamber flushed with helium to recreate a comparable starting point. The measured H_2O_2 densities equate to $6.34 \times 10^{13}\,\mathrm{cm}^{-3}$, $6.26 \times 10^{13}\,\mathrm{cm}^{-3}$ and $6.70 \times 10^{13}\,\mathrm{cm}^{-3}$. The mean and standard deviation are then $(6.43 \pm 0.20) \times 10^{13}\,\mathrm{cm}^{-3}$ which corresponds to an uncertainty of 4 %. The absolute densities are discussed in the results.

4. Results and Discussion

While studies on the COST-jet have shown that here, a "significant portion of power manifests as heat on the plasma dynamics timescale (ñs) via electron impact reactions [...] and ion heating" [85], inelastic collisions drive chemical reactions via dissociation and ionisation [33].

In the following chapter, heating of the gas and plasma source such as some of these chemical reactions should be further investigated. For this, a characterisation of the plasma source in terms of temperature is presented first. Then, the focus is set on the formation of OH and H_2O_2. Here, spatially resolved measurements of OH are presented first to get a first impression of the distribution of OH in the effluent. Then, air entrainment is investigated for the calculation of absolute OH densities. These are investigated together with the H_2O_2 density for a variation of several parameters. The chapter is concluded with a discussion of possible adaptions of the experiment for future needs.

4.1 Temperature characterisation of the source

Knowledge of the gas and effluent temperature, as well as heating of the components of the source gives information on the distribution of energy into the system. Also, the temperature is an important factor in the reaction rates for several chemical reactions [51]. Therefore, the characterisation of the thermal behaviour of the setup is essential for further analysis and is presented in the following.

The temperature of the gas in the plasma zone is determined by two diagnostics. This approach is taken to validate the diagnostics as both do not measure the temperature directly. Thermocouple measurements in the effluent are extrapolated to the end of the plasma to obtain the gas temperature (section 3.2.1). Optical emission spectroscopy determines the temperature from the emission of excited OH inside the plasma (section 3.2.2).

A comparison of the results from both diagnostics is shown in figure 4.1.1. All temperatures are given in °C (left) and Kelvin (right) to allow for better comparability with known temperature ranges and values used for chemical reaction rates.

The temperatures obtained from both methods are in good agreement. Tem-

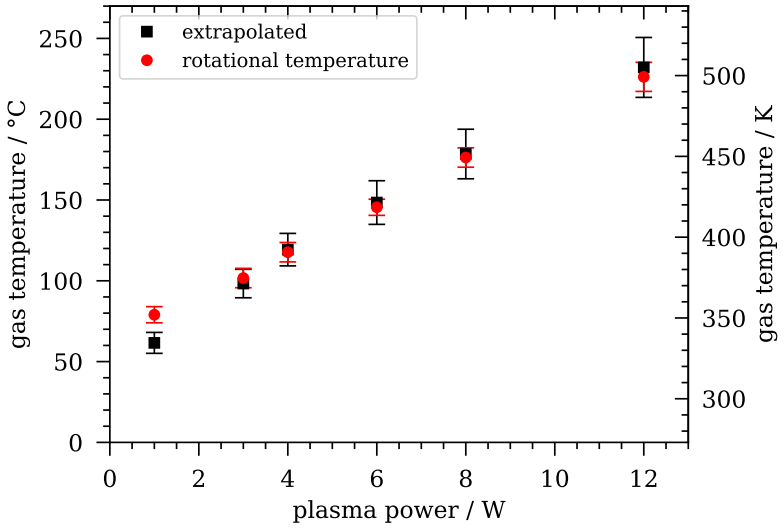

Figure 4.1.1: Gas temperatures obtained from extrapolation of the temperature of the effluent (black squares) and rotational temperature (red circles). Measurements are taken for a gas flow rate of 1 slm and dry helium.

peratures measured with the thermocouple increase linearly with the dissipated plasma power from $(62 \pm 7)\,°C$ at 1 W to $(232 \pm 18)\,°C$ at 12 W.

The rotational temperature increases linearly from $(79 \pm 5)\,°C$ at 1 W plasma power to $(226 \pm 9)\,°C$. The error is determined from multiple measurements, a potential systematic error is not regarded in this case.

In the range of 3 W to 12 W, the diagnostics yield the same temperature with regard to their error. The temperatures only deviate for 1 W plasma power. This may be caused by a slight offset of the thermocouple in the gas stream and error propagation through the extrapolation. As the extrapolation would ideally be performed for each power individually, as the heat exchange with the surrounding gets more effective with increasing temperature, this also influences the precision of the extrapolated gas temperature. Just under 1 W plasma power, the plasma transitions into Penning-mode and may therefore be less stable here. Also, the uncertainty of the rotational temperature is rather small and does not reflect the systematic error of the setup but only the uncertainty of the fitting routine. Considering potential uncertainty due to the setup, the total uncertainty is expected to be higher. Nevertheless, temperature measurements with both methods are regarded as trustworthy based on their agreement in temperature.

While the presence of H_2O is the prerequisite for H_2O_2 production in the plasma and an increase in the H_2O concentration is associated with an initial increase in the H_2O_2 production, the dissipated plasma power serves to drive chemical processes. Thus, both variations of the feed gas humidity and plasma power are performed.

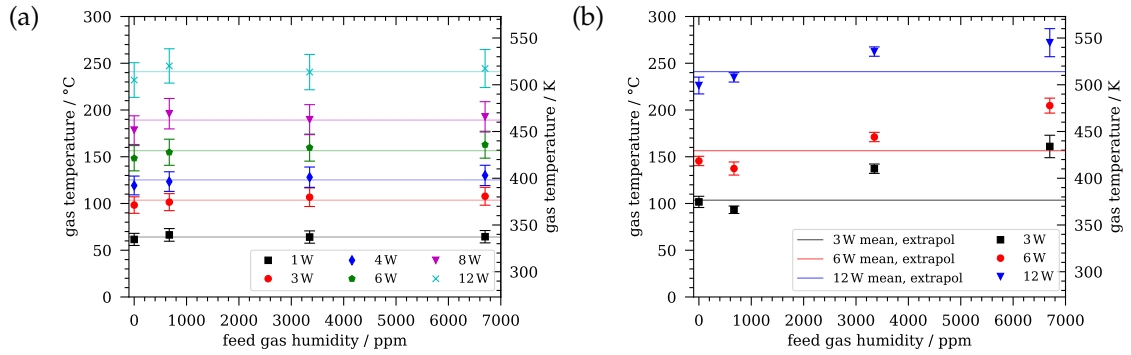

Figure 4.1.2: Gas temperature obtained from (a) thermocouple measurements and (b) rotational temperature depending on the feed gas humidity. Measurement at a gas flow rate of 1 slm helium. The mean temperature obtained from the extrapolated thermocouple measurements at constant plasma power is indicated by a horizontal line in both plots.

The dependence of the temperature on the dissipated plasma power and feed gas humidity is shown in figure 4.1.2a. The temperatures show a slight increase from 0 ppm feed gas humidity to feed gas with added humidity. The temperature then does not change significantly in a feed gas humidity range up to 6400 ppm but only increases linearly with the dissipated plasma power. The investigated feed gas humidity levels are below 1 %. Therefore, it is deduced that helium still predominantly determines the thermal behaviour of the plasma, the fraction of humidity does not influence the temperature significantly.

A comparison of the mean temperature obtained from thermocouple measurements and rotational temperatures depending and feed gas humidity for 3 W, 6 W and 12 W is shown in figure 4.1.2b. As shown in figure 4.1.1 and discussed for dry helium, the temperatures match with regard to the uncertainty for feed gas humidity levels up to 640 ppm. At higher feed gas humidity, the temperature exceeds the extrapolated temperature by up to 50°.

Consequently, the results of temperature measurements performed by optical emission spectroscopy may overestimate the rotational temperature for higher feed gas humidity. A possible cause of this phenomenon is the overpopulation of higher rotational states in He-H_2O plasmas. The overpopulation has been found to cause an overestimation of the temperature when applying a single temperature distribution [73]. The authors have also found that a single temperature Boltzmann distribution yields a good fit of the OH(A-X) spectrum for a feed gas humidity up to 1000 ppm. This limit found by Bruggeman et al. [73] matches the observations in this work. While temperatures obtained from both diagnostics are in good agreement at feed gas humidity levels under 1000 ppm, rotational temperatures then increase with increasing feed gas humidity. Therefore, the

thermocouple measurements are used as an estimate of the gas temperature.

The conducted mean gas temperatures are in the range of 64 °C to 241 °C for 1 W to 12 W. Here, significant heating of the plasma source is expected. Therefore, measurements of the heating of the plasma source are taken to gather information for a more comprehensive thermal characterisation of the source.

An overview of the temperatures of the individual components of the plasma source operated with dry helium at a gas flow of 1 slm and 6 W plasma power is shown in figure 4.1.3. The temperature of the capillary is determined at the end of the plasma zone as well as the capillary end. The electrode temperature is determined as representative of the housing temperature in proximity to the discharge.

The temperature of the effluent 1 mm from the capillary end is lower than the gas temperature but still significantly elevated. The temperate increases from (55 ± 4) °C to (207 ± 6) °C. Especially at high plasma powers, the temperature of the effluent is too high to work with biological enzymes in liquids. Even if the enzymes were resistant to high temperatures, evaporation of the liquid would require constant refilling of the solution.

The temperature of the capillary in the plasma zone rises linearly from (40.0 ± 0.8) °C at 1 W to over (141.3 ± 2.5) °C at 12 W plasma power. The temperature at the capillary end is significantly lower ranging from (36.2 ± 0.6) °C to (109.0 ± 2.3) °C and is similar to the electrode temperature which was measured at 1 W, 6 W and 12 W. At 1 W, the electrode temperature was measured to be approximately (34.5 ± 0.6) °C and rises to (105.2 ± 1.4) °C at 12 W plasma power. The temperature of the plasma source is therefore expected to rise to a steady state temperature that results from heating and cooling by ambient air. Only components in direct contact with the plasma exceed this temperature. For low plasma powers, the temperature of the setup approaches room temperature.

To avoid thermal stress on the component and remain in a feasible temperature range for application, the plasma power should be limited below 12 W. The power is therefore limited to 8 W in the further course of the work. Therefore, the range of the gas temperature narrows down to approximately 60 °C to 180 °C or 333 K to 453 K respectively.

Estimation of the percentage of the dissipated plasma power that is deposited as gas heating can be obtained using equation 4.1, which assumes that a fraction $p \in [0,1]$ of the plasma power is converted into gas heating [55].

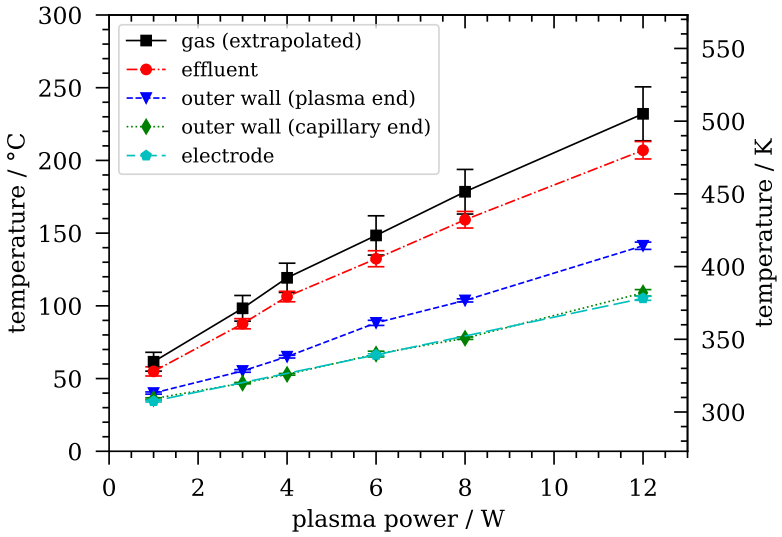

Figure 4.1.3: Thermal characterisation of the plasma source. The temperature of the effluent and capillary wall is measured with a thermocouple. The electrode temperature is determined by a Luxtron. The gas temperature is extrapolated from the effluent temperature.

$$P = p \cdot \frac{\Delta m}{\Delta t} c \cdot \Delta T \tag{4.1}$$

Here, P denotes the plasma power, $\frac{\Delta m}{\Delta t}$ represents the mass flow, c is the heat capacity, and ΔT is the increase in gas temperature. For a flow of 1 slm pure helium, the heat capacity is $5194\,\mathrm{J\,kg^{-1}\,K^{-1}}$ [86] and the mass flow is $2.97 \times 10^{-6}\,\mathrm{kg\,s^{-1}}$. For a plasma power of 6 W, the maximum temperature is estimated to be 682 K. However, Winzer et al. [33] have found that the fraction of about 60 % of the dissipated plasma power is deposited as gas heating for the setup used in this work, leading to a maximum gas temperature of 527 K.

In this work, the measured temperatures are significantly lower than the expected temperature based on the plasma power deposited as gas heating, indicating that only a fraction of the power (>30 %) is transferred to the gas phase. As an example, the gas temperature is estimated to be at (421 ± 14) K at 6 W plasma power and dry helium. As temperatures obtained from extrapolation of the effluent temperature corrected by a factor of (1.12 ± 0.06) from the mean temperature increase and temperatures obtained from the OH(A-X) rotational bands show good agreement both in this work and the work of Winzer et al. [33], reliability in terms of the diagnostics is assumed for both.

Winzer et al. [33] have not measured the temperature in dry helium but used an admixture of 2 % O_2 to their feed gas. However, they have shown that the temperature does not strongly vary with oxygen admixtures up to 2 %. Therefore,

a comparison of the temperature is assumed to be feasible even though the gas admixture deviates slightly.

Assuming the reliability of the measured temperatures, a factor 2 in the dissipated plasma is present between this work and the study by Winzer et al. [33]. As both works are performed on the same design of plasma source, power measurements are a likely cause for the deviation. Based on the explanation of the power calculation, the same approach was taken (see section 3.1.3). The oscilloscope raw data was checked and the power was manually calculated for some reference values. No significant difference between the power calculated by hand and by the COST power monitor [71] was found. The programme used in [33] was a self-programmed Labview program that does not run with the oscilloscopes that are available here in the lab. Therefore, parallel measurements are still open for investigation.

Concluding, it was found that 30 % of the dissipated plasma power goes into gas heating. The temperature rises linearly with the temperature for all feed gas humidity levels from 0 ppm to 6400 ppm. The temperature does not vary significantly with the feed gas humidity in the investigated range.

4.2 Analysis of OH and H_2O_2 in the effluent

Production of H_2O_2 mainly relies on OH as its precursor. The production and loss of both species is therefore closely linked and will be regarded simultaneously in this section. Laser-induced fluorescence offers spatial resolution of the OH distribution while Fourier-transform infrared spectroscopy only yields average values in the far-field of the effluent. Therefore, a spatially resolved characterisation of OH in the effluent along with quantification of air entrainment is presented first. For the subsequent parameter-variant analysis of OH and H_2O_2, the density of OH is only considered close to the capillary end (4 mm) and 14 mm from the capillary end, which corresponds to the value of the settings used for liquid treatment [36].

4.2.1 Spatially resolved characterisation of OH

Spatially resolved LIF gives first information on the distribution of OH in the effluent and is therefore conducted and discussed in the following section. Comparison of the LIF signal at different parameters must be performed carefully though as the LIF signal is dependent on several parameters with the gas admix-

ture being one of the most important ones.

Maps of the LIF signal in the xy-plane were taken at varied distance from the capillary end to get an impression of the spatial distribution along the z-axis. These maps are shown in figure 4.2.1 with increasing distance from top to bottom. The left column shows the maps scaled to the individual maximum of the map to identify the spatial profile of the signal. In the right column, all maps are scaled to the overall maximum LIF signal for comparability of the signal at varied distance. Asymmetry in the signal can clearly be seen close to the capillary end (figure 4.2.1a and 4.2.1c). The signal is elliptical and widens with increasing distance. The LIF signal is broader in x-direction. This corresponds to a higher signal at the electrodes which are placed at $x = \pm 0.5\,\text{mm}$. Regarding the relative values, the OH distribution increases both in x- and y-direction whereas the increase in y-direction is faster so that the area of the LIF signal becomes circular (figure 4.2.1e and 4.2.1g).

The area of the ellipse obtained from the FWHM in x- and y-direction increases by 340 % from 4 mm to 14 mm distance. While the area is at 1.1 mm^2 4 mm from the capillary end, it increases over 1.3 mm^2 (7 mm) and 2.2 mm^2 (11 mm) to 3.6 mm^2 at a distance of 14 mm. A link between the broadening of the LIF signal and a potential expansion of the gas stream is discussed in the course of the investigation of air entrainment.

With increasing distance, the OH signal decreases rapidly. With regard to the normalised scale, the signal decreases by 76 % from 4 mm to 7 mm (figure 4.2.1b and 4.2.1d). 11 mm from the capillary end, the signal is under 10 % of the maximum measured signal (figure 4.2.1f) reducing further to less than 5 % at 14 mm (figure 4.2.1h). Therefore, only a fraction of the OH produced in the plasma reaches a surface at 14 mm and the detected signal is spread out over a wider area.

The change of the OH distribution in x- and y- direction with increasing distance from the capillary end is visualised in figure 4.2.2 in form of a xz- and yz-map. For better visibility of the signal, the colourmap is set to "inferno" instead of "viridis" in this case. Quantification of the decay and width is performed later. A map of the OH LIF signal in the xz-plane is shown in figure 4.2.2a. One can clearly see that the intensity close to the end of the capillary is the highest and the OH LIF signal is at maximum in the centre of the gas stream. The OH LIF signal then rapidly decreases with increasing distance. The intensity also decreases quickly to the sides. At 4 mm distance from the capillary end, the signal is the strongest. A signal is mainly present between -0.5 mm and 0.5 mm which correlates to the position of the capillary. Therefore, no significant broadening of the signal occurs along the first few millimetres.

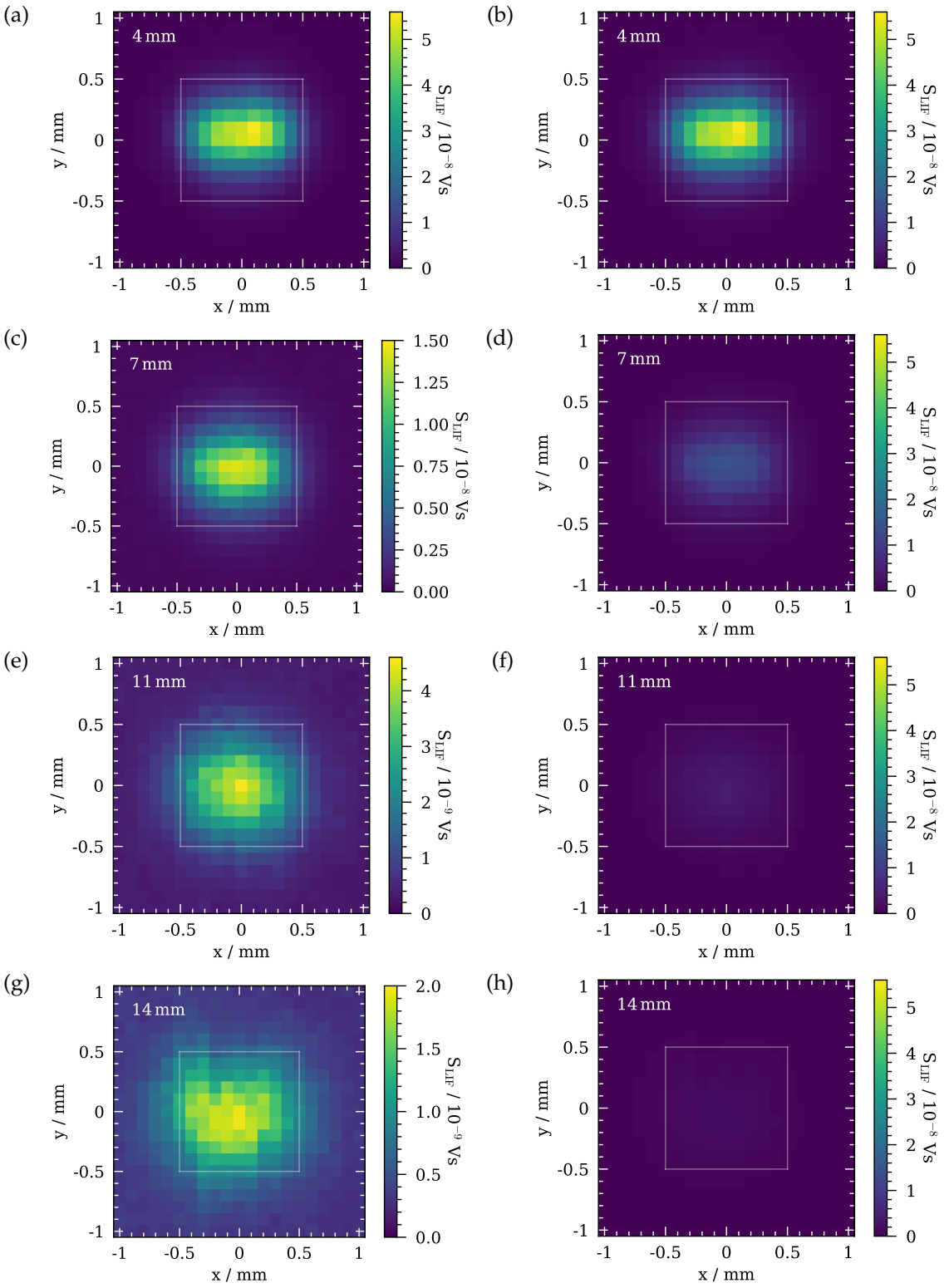

Figure 4.2.1: LIF signal measured in the xy-plane (a) & (b) 4 mm, (c) & (d) 7 mm, (e) & (f) 11 mm and (g) & (h) 14 mm from the capillary end. Left column shows the relative LIF signal scaled to the individual maximum of the map, right column shows the signal normalised to the overall maximum LIF signal. Measurements are shown for a helium plasma at a gas flow rate of 1 slm, 640 ppm feed gas humidity and 6 W plasma power.

The OH LIF signal in the yz-plane is shown in figure 4.2.2b. While the decay towards the sides of the gas stream and in z-direction is similar to the one observed in the xz-plane, the profile is clearly narrower in vicinity of the capillary.

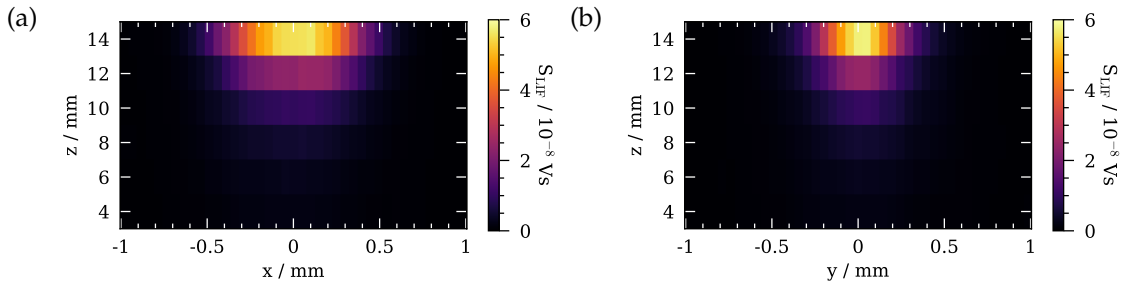

Figure 4.2.2: Maps of OH signal obtained for variation in distance and position in (a) x-direction and (b) y-direction. Measurements are shown for a helium plasma at a gas flow rate of 1 slm, 640 ppm feed gas humidity and 6 W plasma power.

Due to the decay of OH in the effluent, estimation of the width of the gas stream from the maps is not feasible. Therefore, the quantification of the increase in the width of the gas stream is performed by fitting the OH LIF signal at each distance with a Gaussian curve. The fitted spatial profile of OH in the effluent in x- and y-direction at 4 mm distance from the capillary and the full-width half maximum (FWHM) for distances from 4 mm to 14 mm are shown in figure 4.2.3.

The measured LIF signal clearly resembles a Gaussian curve and can be well fitted both in x- and y-direction with R^2 values of 0.994 and 0.997, respectively at 4 mm distance (see figure 4.2.3a). The dimension of the capillary is indicated by vertical grey lines. One can clearly see that the width of the OH LIF signal and therefore spatial distribution of the OH density is determined by the capillary geometry. The asymmetry in x- and y-direction, that is already visible in the maps, accounts to a FWHM of (0.675 ± 0.009) mm in x-direction and (0.447 ± 0.005) mm in y-direction.

Analysis of the broadening effect of the OH LIF signal distribution with increasing distance from the capillary end is shown in figure 4.2.3b. For distances below 14 mm from the capillary end, the width in x-direction is always greater than the width in y-direction. The distribution of the OH LIF signal widens with increasing distance for both directions but this process is faster in y- than in x-direction. The FWHM is then approximately equal at (1.041 ± 0.022) mm (x) and (1.05 ± 0.04) mm (y) 14 mm from the capillary end. Therefore, the asymmetry in the OH distribution, which is observed close to the capillary end, reduces with increasing distance and the OH distribution becomes symmetrical at a distance of 14 mm.

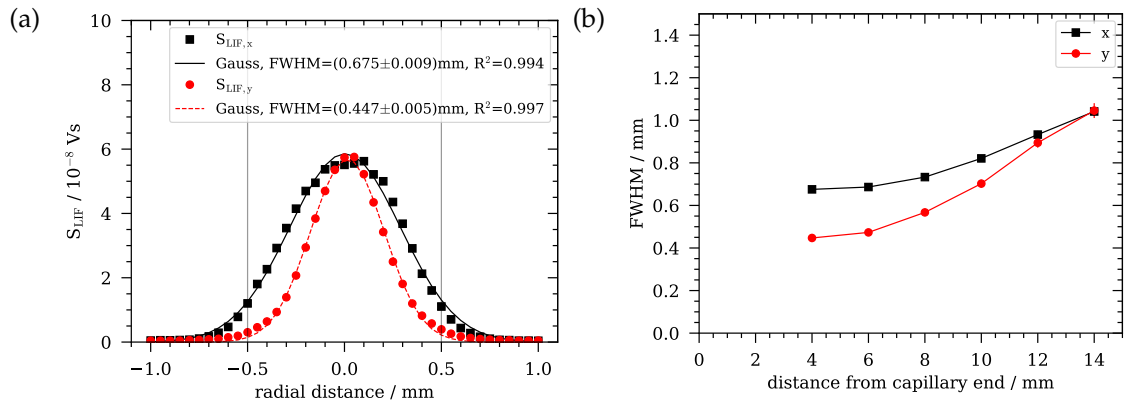

Figure 4.2.3: Spatial profile of the OH LIF signal. (a) Signal at 4 mm distance from the capillary end in x- and y-direction and (b) FWHM of signal derived from Gauss fit at varied distance from 4 mm to 14 mm. Capillary dimensions are shown in as grey lines. Measurements are shown for a helium plasma at a gas flow rate of 1 slm, 640 ppm feed gas humidity and 6 W plasma power.

The rapid decay is already visible on the maps. For better quantification, z-scans were performed at a resolution of 0.05 mm. In figure 4.2.4, the OH LIF signal is shown in the range of 4 mm to 14 mm from the capillary end at the central position in the gas stream. The decay of the signal can be fitted by an exponential decay with high precision (R^2 = 0.997). The signal at 14 mm is already close to zero, therefore only a small fraction of the produced OH is present anymore at that point.

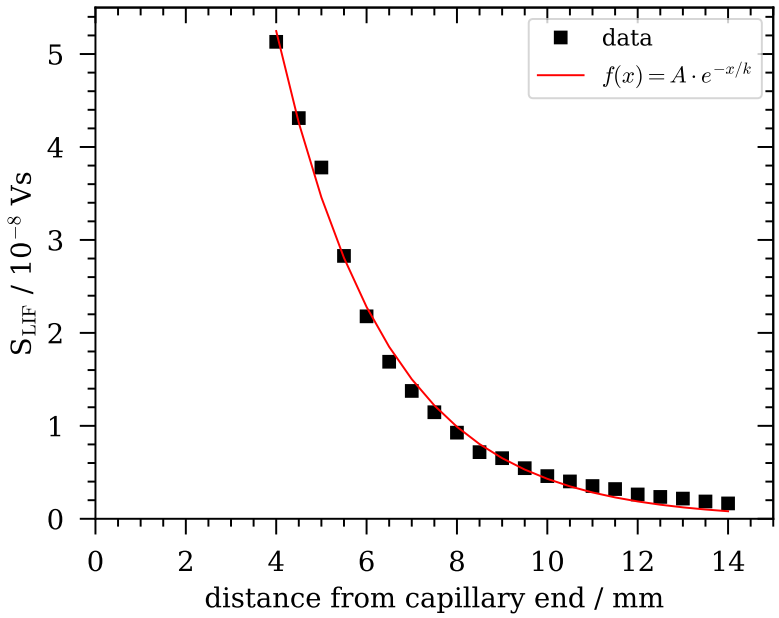

Figure 4.2.4: Decay of OH LIF signal in z-direction in centre of gas stream 4 mm to 14 mm from the capillary end. Measurements are shown for a helium plasma at a gas flow rate of 1 slm, 640 ppm feed gas humidity and 6 W plasma power.

This decay is partly caused by the loss of OH during transport to the point of

observation. Additionally, air entrainment enhances quenching and thus reduced the LIF signal.

In summary, the spatial profile of the OH LIF signal is determined by the dimension of the capillary. It features a strong asymmetry in width as it is broader in x- than in y-direction but is Gaussian shaped in both directions. The asymmetry reduces with increasing distance from the capillary end. Simultaneously, the signal decays exponentially in z-direction.

The asymmetry of the width of the OH LIF signal distribution in the gas stream can be linked to the discharge behaviour of the plasma. The emission is not homogeneous throughout the whole discharge channel but burns more intensely in the sheath region in front of the electrodes. Therefore, the OH production is expected to be more pronounced in the sheath than the bulk which causes the broader OH profile in x- than in y-direction.

PROES measurements performed by Boeddinghaus [37] support this hypothesis. Local emission of OH in the sheath that is nearly constant in time is visible and can be explained by Penning ionisation. Only for low plasma powers under 1 W, the OH emission is mainly present in the bulk and is caused by ionisation due to Ohmic heating. Around 1 W, the discharge switches from Ω- to Penning-mode, therefore the observation of emission is in accordance with the mode.

The asymmetry of the OH distribution in the effluent of the capillary jet is in contrast to the observed profile of NO in the COST-jet [87]. Preissing et al. investigated the NO concentration by LIF measurements in the effluent of the COST-jet at 1 slm helium and varied air admixture. The maps show a homogeneous profile in x- and y-direction close to the nozzle. The measured NO density distribution is circular shaped and becomes irregular with increasing distance from the nozzle, partly due to buoyancy. In contrast to the capillary jet, the investigated range of plasma power is significantly lower. The maps in the xy-plane were taken for 0.6 W plasma power. Operation in Ω-mode is characterised by bulk emission. This difference supports that the transition into Penning-mode causes asymmetric profiles. At the same time, widening of the NO stream was also observed by Preissing et al. [87]. As the gas flow of the capillary jet is vertical while the gas stream of the COST-jet is in horizontal direction, the profile of the capillary jet in the xy-plane is not distorted due to buoyancy as is is for the COST-jet.

So far, the spatial characterisation has only been performed at constant plasma power, feed gas humidity and gas flow rate. Investigation of the influence of these three parameters on the OH distribution is performed via profile scans.

The **feed gas humidity** can influence both the spatial profile in the xy-plane such as the course in z-direction depending on the influence of the humidity of the ambient atmosphere.

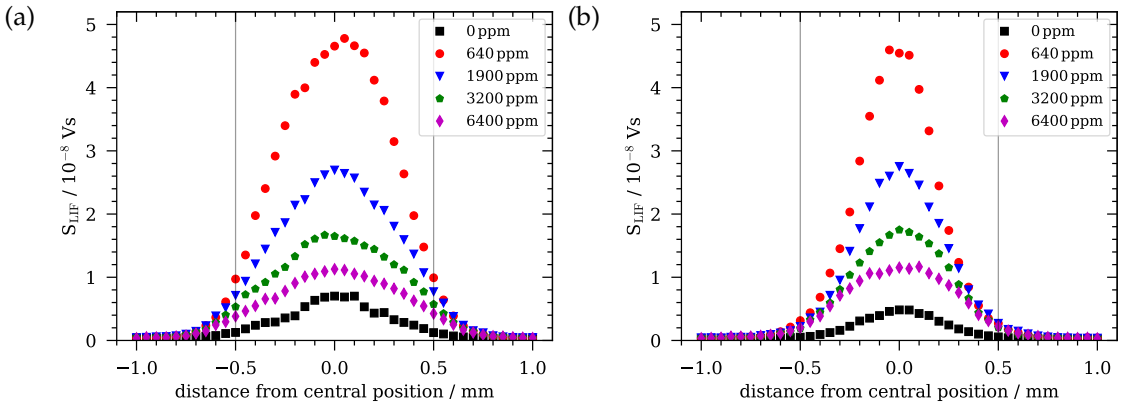

Figure 4.2.5: Spatial profile of the OH LIF signal in (a) x- and (b) y-direction at varied feed gas humidity. Capillary dimensions are shown in as grey lines. Measurements are shown for a helium plasma at a gas flow rate of 1 slm and 6 W plasma power 4 mm from the capillary end.

The OH LIF signal in x- and y-direction is shown in figure 4.2.5. For all feed gas humidity levels, the recorded OH signal is broader in x- than in y-direction. Additionally, the same trend with a maximum in the centre is observed for dry feed gas and feed gas with added humidity. This indicates, that the OH is produced mainly inside the plasma. Thus, a significant amount of impurities is present also for dry helium.

In the case of the production of OH in the effluent, an increase of the measured LIF signal is expected in the first few millimetres of the effluent which is caused by an influx of humid surrounding air into the effluent [26] and would cause a maximum OH LIF signal towards the sides of the effluent instead of the centre [77], which is not visible in the experiments performed here. For dry feed gas, the humidity in the shielding gas becomes dominant for the OH production processes, and therefore the OH production takes place in the effluent, although the produced OH is significantly lower than for a comparable feed gas humidity [26].

The impurities in dry helium may be caused by the setup of the gas supply. The dry and humidified feed gas meet at a T-section from where the gas mixture flows towards the plasma source. When closing the valves of the bubbler and therefore stopping the flow of humidified helium into the feed gas, some rest tubing is open connecting the valve and T-section. In this connecting part, there is still some humidified helium which is then slowly drawn into the gas flow by the dry helium flow. To reduce this issue, a wait time of at least 5 min is ensured between

changing the admixture to dry helium and starting the measurement. As flushing of the tubing is not feasible here though as it would require emptying the bubbler vessel, it is expected that it takes much longer to achieve a fully clean gas supply. A cold trap would account for this issue but is not been implemented in the setup used for the presented measurement.

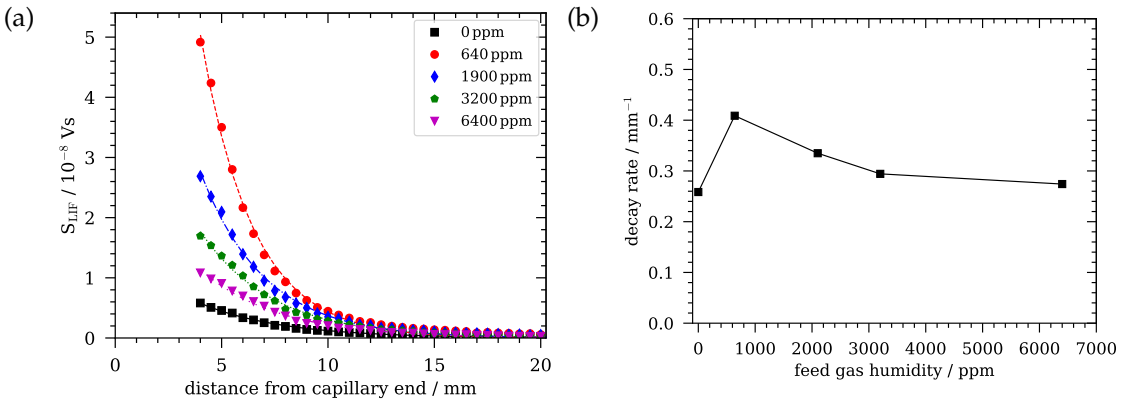

Figure 4.2.6: (a) Decay of the LIF signal in z-direction with exponential fit $f(x) = A \cdot e^{-k \cdot z}$ and (b) decay rate k with lines to guide the eye for varied feed gas humidity. Measurements are taken centrally in the gas stream for a helium plasma at a gas flow rate of 1 slm and 6 W plasma power.

Regarding the decay in z-direction, it follows an exponential decay for the investigated region from 4 mm to 29 mm behind the capillary end for all humidity levels. Figure 4.2.6 shows the distance-dependent OH LIF signal from the capillary end up to 20 mm. At this point, the signal does not change anymore and only Rayleigh signal is detected. Therefore, the region shown in the graph is reduced to the region of interest. The signal was taken at a constant gas flow rate of 1 slm and 6 W plasma power centrally in the gas stream. The exponential fit of the data is shown in figure 4.2.6a. The signal decreases exponentially for each feed gas humidity level with a high coefficient of determination of at least $R^2 = 0.996$. This undermines the above-stated thesis that even for dry helium, the OH is mainly produced inside the plasma and not strongly determined by the ambient humidity. The OH signal is strongest for a feed gas humidity of 640 ppm and weakest for 0 ppm. For feed gas humidity levels above 640 ppm, the OH LIF signal decreases again. This behaviour will be discussed in detail when regarding the absolute OH densities in section 4.2.3.

The decay rate k resulting from the exponential fit $f(x) = Ae^{-kz}$ is shown in figure 4.2.6b. The decay rate increases from 0 ppm to 640 ppm and then decreases monotonously with increasing feed gas humidity. This trend matches the trend of the intensity of the OH signal. While the OH LIF signal is highest for 640 ppm, it also decays the fastest here. With regard to air entrainment into the gas stream, it

is likely that this is partly caused by quenching and is independent of the humidity. In addition, the decay rate may be humidity dependent as OH in the effluent reacts in turn with OH to form H_2O_2. This is an effect that is more pronounced when more OH is present leading to a higher decay rate.

Investigation of the influence of the **plasma power** on the OH decay is shown in figure 4.2.7. As for the varied humidity, the OH signal decreases monotonously in the effluent and follows an exponential trend for investigated plasma powers from 1 W to 8 W (see figure 4.2.7a). The OH LIF signal increases with increasing plasma power. The power-dependent signal decay rate in the effluent is shown in figure 4.2.7b. The decay rate in the effluent is constant for plasma powers over 3 W. It is slightly higher in the case of 1 W plasma power. The difference in the decay rate may be caused by the difference in temperature and number of OH species at 1 W leading to a more pronounced loss of OH.

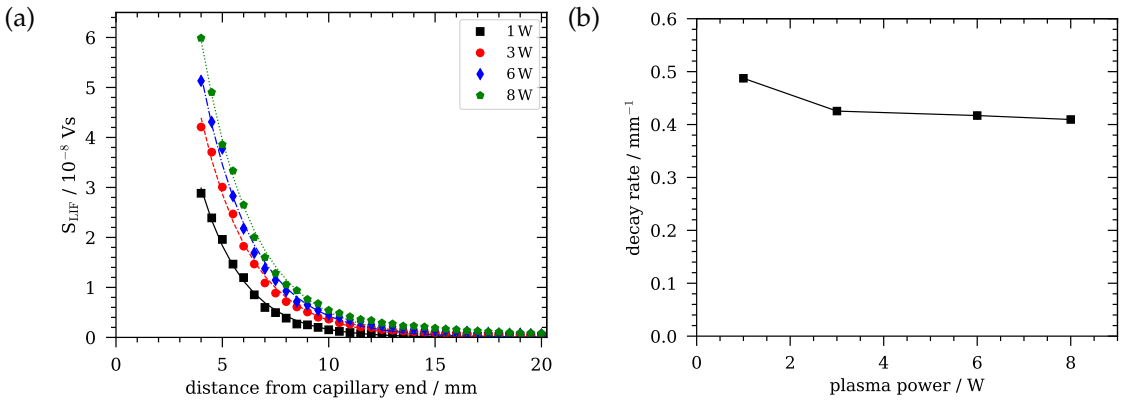

Figure 4.2.7: (a) Decay of the LIF signal in z-direction with exponential fit $f(x) = A \cdot e^{-k \cdot z}$ and (b) decay rate k with lines to guide the eye for varied plasma power. Measurements are taken centrally in the gas stream for a helium plasma with 640 ppm feed gas humidity at 1 slm gas flow rate.

In addition to the variation of power and humidity, the **gas flow rate** is varied in the experiments. As the variation of the gas flow rate changes the transport of the species and velocity of the species in the gas stream, changes in the OH LIF signal are expected mainly in z-direction. The course of the OH LIF signal for a varied gas flow from 0.5 slm to 2 slm is shown in figure 4.2.8.

The OH LIF signal for varied distance up to 30 mm is shown in figure 4.2.8a. At a gas flow rate of 0.5 slm, the OH LIF signal is significantly smaller than for higher gas flow rates. 8 mm from the capillary end, the signal has reduced by one order of magnitude in comparison to the signal at 4 mm. After 10 mm from the capillary end, no major decrease is measured anymore and the signal is close to zero. For higher gas flows, not only the maximum OH signal is higher but OH is also increasingly far detectable. For gas flow rates of 1.5 slm and 2 slm, the OH

LIF signal is constant up to 5 mm and 6 mm respectively. The exponential decay therefore sets in later and species are transported further away from the capillary end.

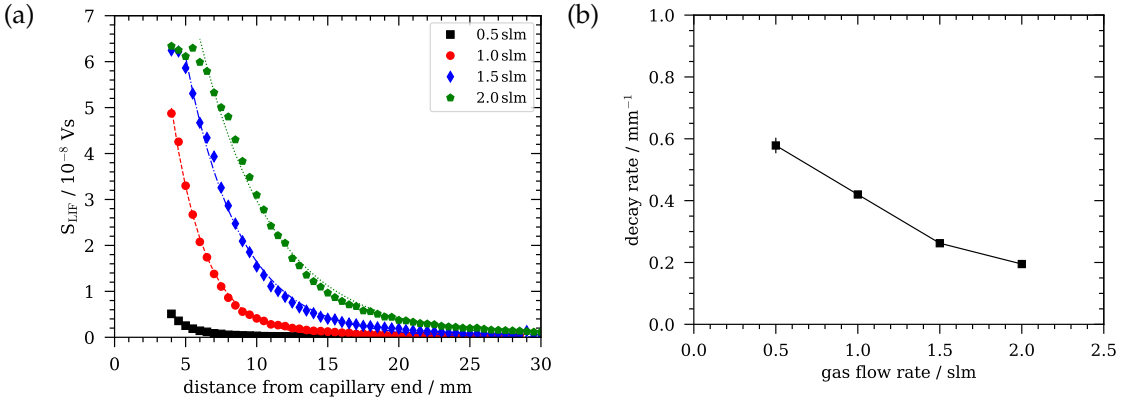

Figure 4.2.8: (a) Decay of the LIF signal in z-direction with exponential fit $f(x) = A \cdot e^{-k \cdot z}$ and (b) decay rate k with lines to guide the eye for varied gas flow rate. Measurements are taken centrally in the gas stream for a helium plasma at with 640 ppm feed gas humidity and 6 W plasma power.

The occurrence of a plateau in the first few millimetres behind the capillary end may be caused by different aspects. First, the OH signal is drastically reduced by quenching due to entrained air. In case of higher gas flows, the air admixture in the gas stream may set in later and due to negligible air admixture close to the capillary end, the signal does not decay instantaneously. Elevated temperature of the background gas leads to additional quenching of the OH species. Increased collisional quenching then leads to a reduction of the OH signal [88]. As no signal could be recorded in the first 4 mm due to a significant scattering signal, it cannot be estimated if the plateau is also present in the first 4 mm behind the capillary end and may even be present for lower gas flow rates than 1.5 slm.

The difference in the decrease is compared by the decay rate k resulting from the exponential fit $f(x) = Ae^{-kz}$ which is shown in figure 4.2.8b. The decay rate decreases with increasing gas flow rate. Up to 1.5 slm the decay rate decreases linearly, then the slope decreases towards 2 slm. This shows, that not only does the higher amplitude of the OH signal cause a longer presence of detectable OH species in the effluent but the OH species have a lower distance-related decay with increasing gas flow rate.

In summary, the relative OH LIF signal is strongest centrally in the gas stream for each investigated feed gas humidity and features a Gaussian shaped distribution in both x- and y-direction. Asymmetry of the signal in the x-y-plane is present close to the capillary end and decreases with increasing distance. The signal decays exponentially, and the decay rate is dependent on the feed gas humidity and

gas flow rate, as these significantly affect quenching. Additionally, the loss of OH by reaction with OH influences the OH LIF signal.

4.2.2 Air entrainment in the effluent

The OH signal is not solely determined by the density of OH at the point of observation but is significantly influenced by quenching processes which reduce the excited species' lifetime. In the effluent, the admixture of air plays a crucial role in quenching the excited species, as collision and reaction partners alter the collisional dynamics. Thus, this section presents an analysis of the intrusion of air into the helium gas flow. The amount of air was quantified based on the decay time of the LIF signal from the model.

Figure 4.2.9 presents xy-plane maps illustrating the air admixture in humidified helium feed gas at varying distances ranging from 4 mm to 14 mm. The colorbar presents the fraction of air in the feed gas, with 100 % corresponding to 100 % humidified helium feed gas and 0 % representing 100 % air. The capillary position at 0 mm is indicated by a white square.

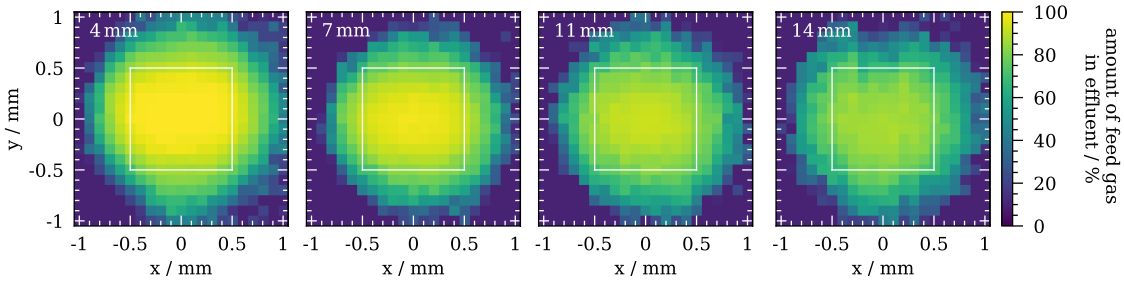

Figure 4.2.9: Spatial distribution of the air admixture in humidified helium feed gas in the xy-plane. The underlying LIF data was obtained for a helium plasma at a gas flow rate of 1 slm, 640 ppm feed gas humidity, and 6 W plasma power.

Near the capillary, the effluent underneath the capillary consists of feed gas only. However, at the edges of the area underneath the capillary, air starts to enter the effluent, while the feed gas still dominates with a share of 80 % of the gas admixture. As the radial distance from the effluent centre increases, the amount of air progressively rises until only air remains.

With increasing distance from the capillary end, air entrainment becomes more prominent. At a distance of 7 mm, the effluent underneath the capillary consists of 98 % feed gas at the central position. Mostly, the amount of air does not exceed 10 % underneath the capillary towards the edges. 11 mm from the capillary end, a substantial amount of air is present throughout the effluent. In the central region

of the gas stream, the fraction of feed gas amounts to 92 %, while the amount of air exceeds 15 % beneath the capillary towards the outer region. At a distance of 14 mm from the capillary end, the amount of feed gas decreases to 87 % centrally within the gas stream.

For higher air admixtures, the fitting routine of the LIF signal decay becomes increasingly uncertain. At approximately 50 % air admixture, the decay due to quenching reaches a timescale similar to the laser pulse's decay time. Hence, accurate evaluation is unattainable.

The width of the gas stream does not exhibit significant changes. Instead, the mixture of helium and air changes as the fraction of air in the effluent increases with increasing distance. This phenomenon becomes particularly apparent in the air intrusion maps presented in the xz- and yz-planes in figure 4.2.10. The scans are shown true to scale and in high resolution in both planes. The width of the gas stream remains constant in both planes. In the xz-plane (figure 4.2.10a), the area with minimal air intrusion is slightly wider compared to the yz-plane (figure 4.2.10b). Also, in the xz-plane, the OH LIF signal is more pronounced. Since the air admixture is deduced from the OH LIF signal, this effect may also be reflected in the admixture. It is anticipated that the gas stream possesses a radial symmetry, and the observed asymmetry mainly arises due to the LIF signal's detectability being limited to regions where OH is present.

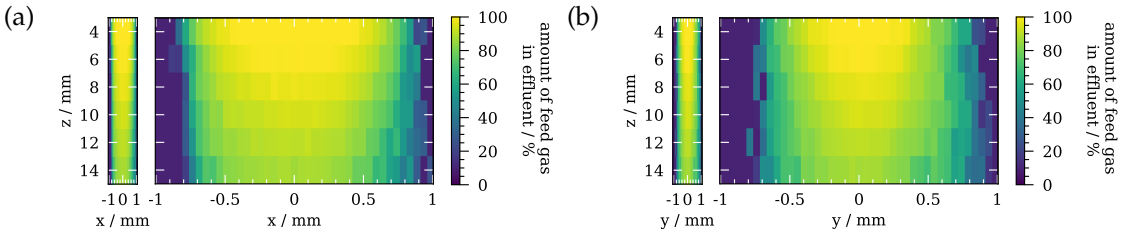

Figure 4.2.10: Maps of air admixture in effluent obtained for variation in distance and a) xz-plane and b) yz-plane adjusted to scale (left) and in high resolution (right). Air admixture is deduced from measurements of a helium plasma at a gas flow rate of 1 slm, 640 ppm feed gas humidity and 6 W plasma power.

These findings align with the spatial distribution of air in a helium effluent reported by Cosimi et al. [78] for an atmospheric pressure plasma jet (APPJ) operating at a gas flow rate of 3 slm. They found that up to 2 mm from the outlet of the plasma jet, only helium is present centrally in the effluent. Towards the sides, the air admixture increases. With increasing distance, the air admixture increases to approximately 20 % in the helium effluent. Fluctuations are observed along the gas stream, but no substantial widening of the gas stream is evident within a 20 mm range.

Similarly, Preissing et al. [87] have investigated the air intrusion into the effluent of the plasma jet in the xz-plane. They found no air intrusion near the nozzle. With increasing distance, the air admixture increases to 30 % centrally in the effluent. The detection of helium is not limited to the width of the plasma channel but extends to a width of 2 mm at an electrode distance of 1 mm. These observations align with the findings presented in this thesis.

Above, air entrainment was regarded for a constant gas flow rate. In this thesis, the gas flow is varied from 0.5 slm to 2 slm. With increasing gas flow rate, the velocity of the particles inside the gas stream increases. The effect on the intrusion of air into the effluent at varied gas flow rate is again determined from maps in the xy-plane 4 mm from the capillary end.

The measured OH densities are displayed in figure 4.2.11. While the diameter of the gas stream does not change significantly, there is no pure air atmosphere in the case of 0.5 slm gas flow rate. The amount of humidified helium still dominates with 97 % contribution to the gas admixture at central position but air holds a share of 3 %. Towards the sides under the capillary, this percentage increases to over 10 %.

In the case of a higher gas flow rate, the area with pure helium increases and the amount of air in the gas mixture underneath the capillary stays below 10 %. Thus, quenching and VET are not only dependent on the feed gas humidity as a determinant for the gas admixture of the feed gas and the distance from the nozzle but also on the gas flow rate. In addition, quenching and VET are also temperature dependent and thus, varying gas temperature will influence the decay time of the LIF signal [40].

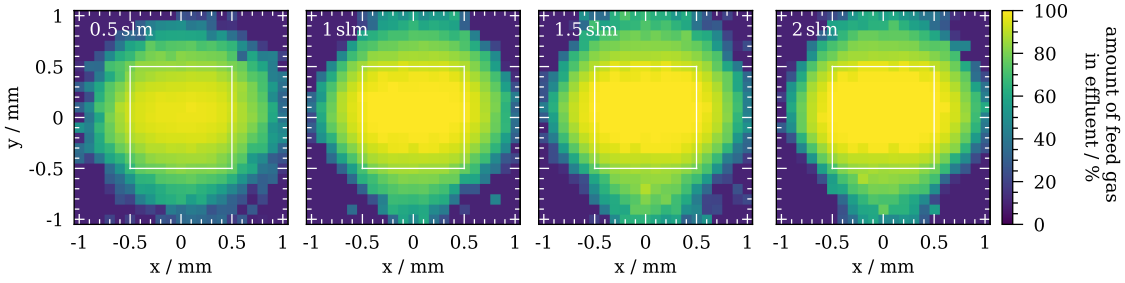

Figure 4.2.11: Spatial distribution of the air admixture in humidified helium feed gas in the xy-plane for varied gas flow rate. The underlying LIF data was obtained for a helium plasma at 640 ppm feed gas humidity and 6 W plasma power 4 mm from the capillary end.

The determination of the air admixture from the LIF decay signal has the advantage that it is precise even for low air admixtures. Raman scattering is also suitable to determine the air admixture but is not as precise for air admixtures

below 1 % [89]. The determination of the admixture is limited by the decay of the OH radicals by spontaneous emission and towards higher gas admixtures by the pulse width and thus decay of the laser beam. The latter one can be improved by using a laser with lower pulse duration which was not possible here. Disadvantages of the diagnostics are that the admixture can only be determined if enough OH radials are present at the point of observation and that the accuracy of the modelled decay is strongly dependent on the precision of the quenching and VET rates [89]. With regard to the good agreement of the obtained spatial distribution of the air-humidified helium mixing ratio found here and the high LIF OH signal, the chosen approach is reasonable here.

In conclusion, no air entrainment is found 4 mm from the capillary end centrally in the gas stream. Towards the sides and with increasing distance, the amount of air in the effluent increases. The width of the gas stream stays constant up to a distance of 14 mm.

4.2.3 OH and H_2O_2 production under parameter variation

In the following, the production of OH and H_2O_2 is investigated. For this, the absolute OH density 4 mm and 14 mm from the capillary and the H_2O_2 density in the far-field are compared for a variation of the feed gas humidity, plasma power, modulation of the plasma power and variation of the gas flow rate.

In the following, the error bars in all figures represent the uncertainty deduced from the reproducibility of the data. The OH densities feature an additional uncertainty resulting from the calibration method. The accuracy of the obtained values is therefore expected to be within a factor of 2. This must be taken into consideration when regarding absolute values. As the uncertainty percentage towards lower densities is not equal to the one towards higher densities [40], no uncertainty is stated with the absolute densities in the text. The H_2O_2 densities are underestimated due to adsorption. As this effect has not been quantified sufficiently in this thesis to account for it in the absolute values, the data is also plotted with the uncertainty resulting from its reproducibility to gain an impression of the uncertainty of the trends. As for OH, no uncertainty is given in the text to avoid a misleading trust interval as the measured density with adsorption is not equal to the density in the effluent.

Feed gas humidity

Feed gas humidity has a significant effect on both production and loss of OH. The presence of water molecules in the feed gas is necessary for the formation of OH. However, high concentrations of water can lead to the production of OH at a level where OH itself becomes an important species in the loss process, as it reacts to form H_2O_2 (section 2.2).

In a first approximation, the yield of H_2O_2 is expected to increase linearly with the feed gas humidity, as the square of OH is known to scale linearly with the humidity in the feed gas [19, 38]. However, at higher feed gas humidity levels, the linear correlation is expected to break down due to the significant role of OH in the destruction of H_2O_2. Additionally, changes in the electron density and temperature at higher feed gas humidity can introduce deviations from the linear trend.

The influence of feed gas and shielding gas humidity on the production of hydrogen peroxide in atmospheric pressure plasmas has been investigated by Reuter et al. [90]. Their results show that the net production rate of H_2O_2 in the gas phase significantly increases with higher feed gas humidity, while the humidity of the shielding gas has only a weak impact on the production. Therefore, they conclude that "humidity-related processes in the feed gas have a greater impact than ambient humidity" [90]. Although measurements of OH and H_2O_2 densities in a liquid after plasma treatment with the capillary jet were conducted in the presence of ambient air as the surrounding gas [35, 36], the FT-IR measurements in this thesis are performed in a closed system, making them unaffected by variations in ambient humidity. The influence of ambient humidity is considered to be negligible based on the existing literature mentioned above, and it is therefore assumed that the observed trends are comparable to those obtained in a system with ambient air.

Selected results obtained on **OH in the effluent** for a varied feed gas concentration are shown in figure 4.2.12. At 1 W plasma power, the relative OH LIF signal increases up to 1900 ppm feed gas humidity. It then gradually decreases with increasing feed gas humidity (not shown here). The relative OH LIF signal for 6 W plasma power is shown in figure 4.2.12a. At higher plasma power, the maximum OH LIF signal is reached rapidly, around 640 ppm feed gas humidity. Subsequently, the signal exhibits a slower decline compared to the initial increase. Similar trends are observed for plasma powers of 3 W and 8 W. Notably, even without additional humidity added to the feed gas, a detectable amount of OH is measured close to the capillary end. This phenomenon may be attributed

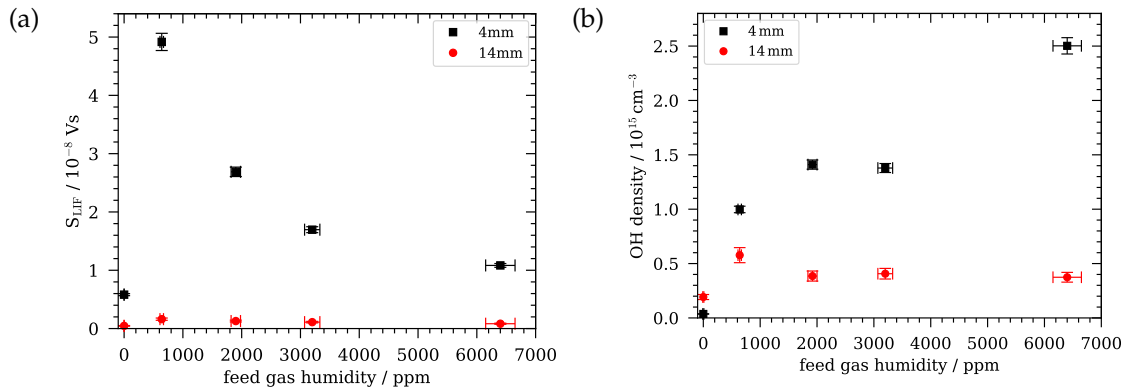

Figure 4.2.12: (a) Relative OH LIF signal and (b) absolute OH density with the assumption of equal humidity in feed gas and effluent for varied feed gas humidity 4 mm and 14 mm from capillary end. Measurements are taken at 6 W plasma power and gas flow rate of 1 slm.

to impurities in the gas pipes that are sufficient to generate a sufficient amount of OH to produce a LIF signal.

The OH production in the plasma is enhanced with increasing feed gas humidity due to increased electron impact dissociation of H_2O [51]. In a lower feed gas humidity regime, the production of OH dominates. At higher feed gas humidity, here above 640 ppm, consumption of OH plays an increasingly significant role in the decline of the observed OH LIF signal. The transition from prevailing production to loss can be attributed to the impact of OH on its loss reaction. The transition has also been attributed to the effect of increasing humidity on electron density and gas temperature. Changes in these two factors influence the reaction rate coefficients and therefore alter the chemistry [51, 91]. As shown in section 4.1, the temperature does not change strongly with varying feed gas humidity and heat conduction is mainly determined by helium. Therefore, this effect is expected to be negligible in the investigated regime. Schröter et al. [30] have found that towards higher water concentrations, the impact of H on the consumption of OH becomes more important and adds to the loss of OH. Additionally, the impact of H and atomic oxygen (O) also contributes to the consumption of OH, especially in the effluent [36]. This aligns with the measured relative OH LIF signal.

Regarding the absolutely calibrated OH densities, this trend does not hold anymore. When a constant feed gas of 0 ppm, 640 ppm, 1900 ppm, 3200 ppm and 6400 ppm is assumed in the model with no air admixture 4 mm from the capillary end, the resulting absolute OH density features an increasing trend (figure 4.2.12b). At 6 W plasma power, the calculated OH density is at $3.7 \times 10^{13}\,cm^{-3}$ for dry helium. At 640 ppm feed gas humidity, a OH density of $1.0 \times 10^{15}\,cm^{-3}$ is

reached which further increases up to $2.5 \times 10^{15}\,\mathrm{cm}^{-3}$ at 6400 ppm.

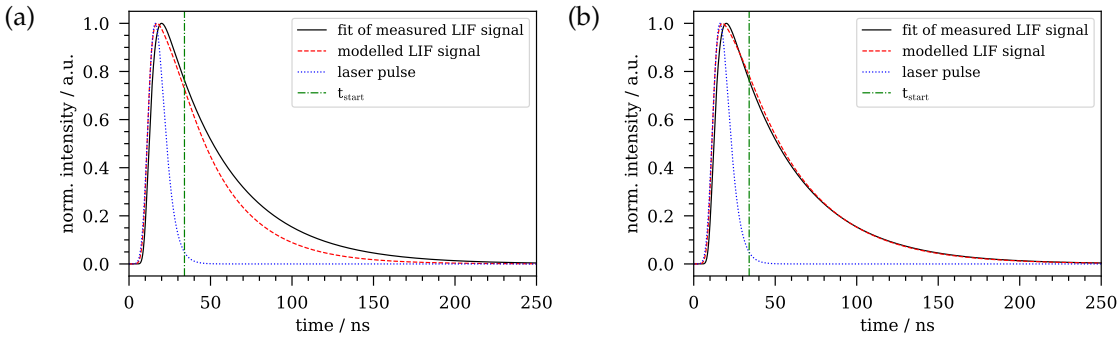

Figure 4.2.13: Fit of measured OH LIF signal and modelled OH LIF signal for (a) equal humidity in feed gas and effluent and (b) reduced humidity in effluent. All data are normalised to unity. Measurements are taken at 1900 ppm feed gas humidity, 6 W plasma power and gas flow rate of 1 slm.

In reality, a part of the water vapour is consumed in the plasma. Consequently, the feed gas humidity is higher than the humidity of the effluent. This effect becomes increasingly prominent for higher feed gas humidity levels and can only be evaluated close to the capillary end with a pure helium-water atmosphere. Further away, air dominates the quenching and therefore, the water concentration at the point of observation cannot be estimated from the data. Instead, slight fluctuations in the amount of air become important. The assumption of a constant feed gas humidity throughout the system causes a significant overestimation of quenching by H_2O in the effluent which can be seen in the deviation of measured and modelled LIF signal decay time, which increases with increasing feed gas humidity. An example of the fitted OH LIF signal at 1900 ppm and 6 W generator power with the modelled LIF signal for a constant water admixture (figure 4.2.13a) and under assumption of water consumption (figure 4.2.13b) is shown in figure 4.2.13. Quenching is overestimated in the case of constant water admixture. Consequently, the OH density is also estimated as too high. Hence, results with adapted humidity in the effluent with regard to water consumption are presented in the following. The consumption of water in the plasma will be discussed later with regard to the plasma power.

In the following, the measurement without added humidity is not considered as here, the humidity cannot be further decreased. When feed gas humidity is decreased until the decay times of measured and modelled LIF signal match, this results in assumed humidity in the effluent of 580 ppm, 1450 ppm, 2550 ppm and 4000 ppm which is significantly lower than the feed gas humidity added by the bubbler.

The resulting OH densities 4 mm and 14 mm from the capillary end are shown in

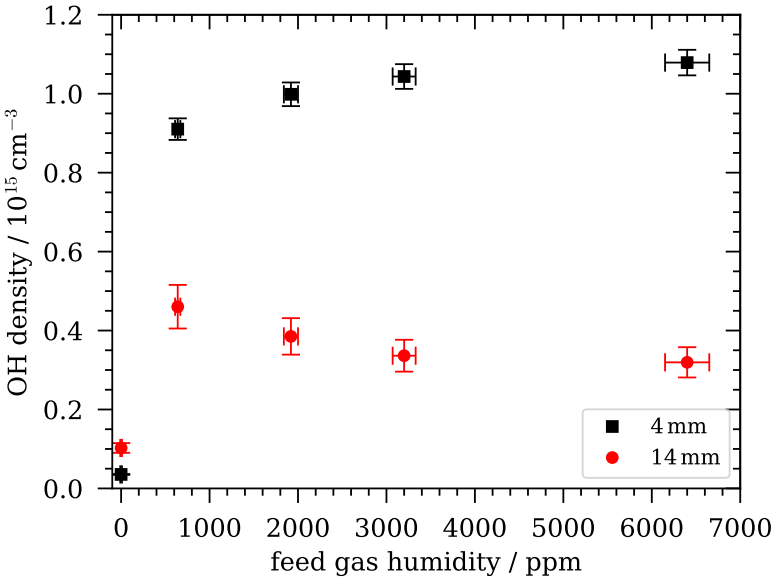

Figure 4.2.14: Absolute OH density 4 mm and 14 mm from the capillary end with consideration of water vapour consumption in the plasma. Measurements are taken at 6 W plasma power and gas flow rate of 1 slm.

figure 4.2.14. The trend for the absolutely calibrated OH densities with consideration of water consumption in the plasma in the model yields a different trend at 4 mm distance than the absolute values under the assumption of equal humidity in feed gas and effluent. Without added feed gas humidity, the OH LIF signal is very weak and the density caused by impurities calculates to $3.5 \times 10^{13}\,\mathrm{cm}^{-3}$. The OH density then rises rapidly and reaches a value of $9.1 \times 10^{14}\,\mathrm{cm}^{-3}$ at 640 ppm feed gas humidity. Above 640 ppm, the OH density only increases weakly and comes to saturation above 6400 ppm where the absolute OH density reaches $1.1 \times 10^{15}\,\mathrm{cm}^{-3}$.

This can again be explained by the reasoning given above. For low feed gas humidity, OH production prevails. At higher feed gas humidity, loss mechanisms intensify and the OH density does not increase further.

Additional reasoning for the flattening of the OH density is related to the electron energy distribution function (EEDF). The EEDF only changes weakly in noble gases with small admixtures of molecules like H_2O [82]. Thus, an increasing admixture of molecules comes with increasing dissociation. When the admixture is sufficiently large, changes in the EEDF occur due to energy losses to attachment as well as rotational and vibrational excitation. Consequently, the amount of energy going into the dissociation of the molecules decreases and causes a reduction in the degree of dissociation [82].

The OH densities 4 mm from the capillary end calculated for lowered humidity

in the effluent are in good agreement with the trends observed by Brisset et al. [51], Verreycken et al. [40] and Benedikt et al. [92]. Brisset et al. [51] studied the production of OH in a helium-driven atmospheric pressure RF-plasma. For humidified helium feed gas, a rapid increase in the OH density was measured up to a few hundred ppm. Afterwards, the OH density further increases in the investigated range of 500 ppm to 10 000 ppm but at a slower pace. Verreycken et al. [40] studied the absolute OH density for varied water concentration 1 mm from the nozzle of an RF-driven plasma jet operated in argon. Here, a steep increase was found for low feed gas humidity levels which then slowly declines. Levelling off is found in the region of 6500 ppm to 26 000 ppm which matches the findings of this work, even though operated in different feed gas. Benedikt et al. [92] have studied the OH density for a setup similar to the COST-jet and have found a rapid increase in the OH density up to 2000 ppm. Afterwards, the OH density levels off and comes to saturation between 6000 ppm and 10 000 ppm.

At a distance of 14 mm from the capillary end, the absolute OH density features a trend that is similar to the relative trend but reveals a weaker decrease after 640 ppm. The OH density increases up to a few hundred ppm feed gas humidity and reaches its maximum at 640 ppm at $4.6 \times 10^{14}\,\mathrm{cm}^{-3}$. The OH density then gradually decreases with increasing feed gas humidity and reaches an absolute value of $3.2 \times 10^{14}\,\mathrm{cm}^{-3}$ at 6400 ppm.

The explanation for the decrease is identical to the one given above for the flattening of the OH density. At higher feed gas humidity, consumption of OH dominates leading to a decrease in the OH density. The more OH, the stronger is the consumption of OH by OH.

The observed trend of the relative OH LIF signal and absolute OH density at 14 mm is consistent with the results of measurements of OH in the liquid and closely resembles the trend obtained from the simulation of the species density in the plasma source by Schüttler et al. presented in [36]. They measured and modelled an initial increase followed by a gradual decline in the OH density 14 mm from the capillary and above 640 ppm feed gas humidity. Measurements of the OH density by Gorbanev et al. [29] conducted in a liquid treated by the COST-jet also feature a similar trend.

The OH density has a direct influence on the H_2O_2 production. The more OH is produced in the plasma, the more H_2O_2 can be formed.

The measured **H_2O_2 densities** are shown exemplary for plasma powers of 1 W and 6 W in figure 4.2.15. Measurements without additional feed gas humidity were also performed, but they are not presented here as the H_2O_2 signal is too

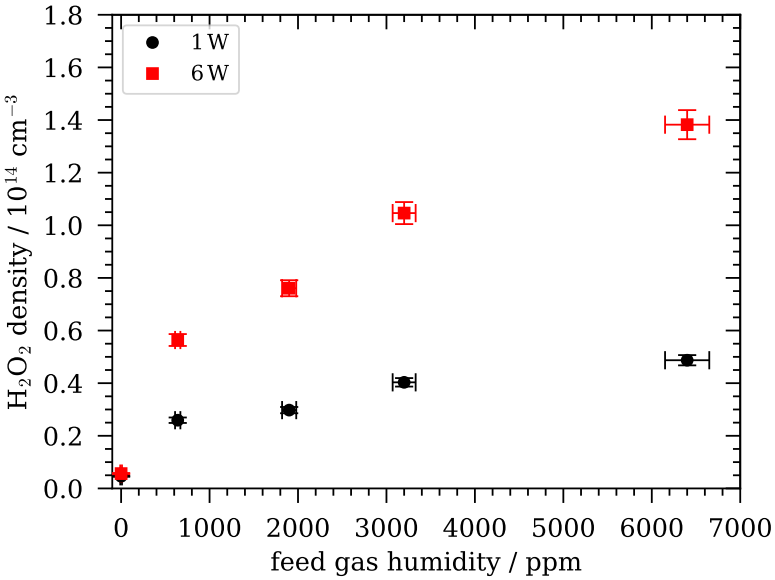

Figure 4.2.15: H_2O_2 density in the far field at 1 W and 6 W for varied feed gas humidity at a gas flow rate of 1 slm.

weak to be accurately fitted. The contribution of feed gas impurities is expected to be the primary source of water content for hydrogen peroxide production at 0 ppm, resulting in detectable traces only. Since the system is sealed, the entry of ambient humidity into the plasma through backflow is prevented. In an open setup exposed to ambient air, additional humidity from the environment could further increase the H_2O_2 concentration.

When humidity is added to the feed gas, H_2O_2 production increases rapidly. At 640 ppm, H_2O_2 densities of 2.59×10^{13} cm^{-3} and 5.64×10^{13} cm^{-3} were measured for plasma powers of 1 W and 6 W, respectively. The measured H_2O_2 density then further increases with increasing feed gas humidity to 4.87×10^{13} cm^{-3} and 1.382×10^{14} cm^{-3}, respectively.

In a simplified model neglecting all other generation and loss processes, one molecule of hydrogen peroxide is formed via OH from two water molecules. Consequently, a linear relationship is anticipated between the concentration of H_2O and the concentration of H_2O_2 [38]. Thus, a doubling of the humidity would result in an increase by a factor of two in the H_2O_2 concentration.

However, this linear trend persists only until the consideration of loss mechanisms. At sufficiently high OH concentrations, OH becomes a significant contributor to the destruction of H_2O_2, causing deviations from the linear trend at higher feed gas humidity levels [19]. Here, it is assumed that losses due to gas temperature are negligible, as the temperature remains well below 500 K (see section 4.1), and thermal dissociation rates within this range are orders of magnitude slower

than other loss mechanisms [19].

The observed increase in the H_2O_2 production holds across the investigated range, up to 6400 ppm, without reaching saturation. Regarding the OH density, the number of OH molecules decreases above a feed gas humidity of 640 ppm. This loss could be attributed to the reaction with the formed H_2O_2 molecules. However, since no change in the gradient above 640 ppm is observed, the loss of OH above 640 ppm is rather contributed to the formation of H_2O_2.

The trends of the H_2O_2 densities align with the findings of various groups such as Vasko et al. [19], who observed an increase up to 10 000 ppm, as well as [90], who reported a non-linear dependency within the investigated range up to 2000 ppm. Schröter [93] investigated the concentration of H_2O_2 in a liquid treated with a modified version of the COST-jet under varied humidity. They observed a rising trend up to approximately 7000 ppm, followed by a saturation effect at higher feed gas humidity.

This saturation trend has also been observed in the case of the capillary jet, where measurements in a plasma-treated liquid using spectrophotometric diagnostics were performed [36]. This deviates from the increase observed across the entire investigated humidity range in this study. In the work of Schüttler et al., saturation was already observed from 2000 ppm feed gas humidity. While the FTIR measurements are performed in the gas phase, the study by Schüttler et al. is carried out in a plasma-treated liquid, indicating that interaction mechanisms with the liquid may further contribute to the loss of H_2O_2 at sufficiently high H_2O_2 densities.

Regarding the absolute values, the obtained densities are significantly lower than the ones expected from the work of Schüttler et al. [36]. This may be attributed to widening of the beam inside the multipass cell and therefore a greater intensity loss than expected for the regarded absorption length. The major reason may be adsorption of H_2O_2 to the walls though. By this, a significant portion of H_2O_2 is not detectable in the multipass cell anymore and thus, the H_2O_2 density appears to be lower than expected from the simulation performed on the setup in [36].

In summary, the OH density increases rapidly up to a few tenths of a percent feed gas humidity. Close to the capillary end, the increase slows down above 640 ppm and reaches a plateau. At greater distances, the OH density decreases after reaching its maximum at 640 ppm. The H_2O_2 density also increases rapidly along the first few hundred ppm feed gas humidity. The increase then slows down but the H_2O_2 density still rises monotonously with feed gas humidity.

Plasma power

The energy needed for the chemical reactions inside the plasma must be provided externally. Thus, the production of reactive species inside the plasma is closely related to the plasma power. Here, the effect of varied plasma power is studied in the range of 1 W to 8 W for feed gas humidity levels from 0 ppm to 6400 ppm.

The fitted humidity in the effluent in comparison with the feed gas humidity added by the bubbler is shown in figure 4.2.16. The estimated water vapour concentration in the effluent deviates increasingly from the feed gas humidity with increasing plasma power. For 640 ppm, the humidity decreases to 550 ppm at 8 W which corresponds to a decrease to 86 % of the input. For 6400 ppm feed gas humidity, the fitted water vapour concentration in the effluent is already lowered to 5500 ppm (86 %) at 1 W plasma power. This deviation further intensifies with increasing power to a water vapour concentration in the effluent of 3900 ppm (60 %).

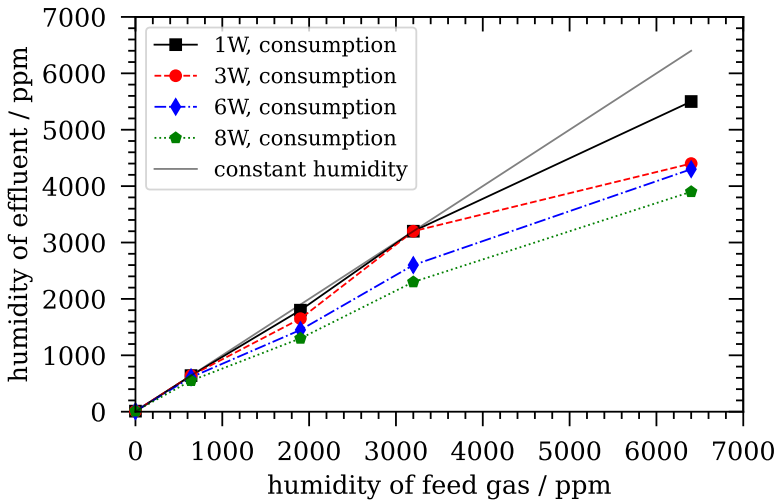

Figure 4.2.16: Fitted humidity in the effluent compared to feed gas humidity 4 mm from the capillary end at varied plasma power. Constant humidity shown as grey line. Data points of estimated humidity in effluent are connected by lines to guide the eye.

The **OH production** under variation of plasma power is shown in figure 4.2.17. A rising trend is observed both for the relative LIF signal (figure 4.2.17a) and the absolute OH density (figure 4.2.17b and 4.2.17c). Fitting of the OH LIF signal without regard to water consumption in the plasma leads to an overestimation of quenching which increases with increasing plasma power. This causes an overestimation of the OH density in the effluent. Hence, results with adapted humidity in the effluent with regard to water consumption are presented in the following.

The absolute OH densities in the effluent are estimated with regard to a lowered

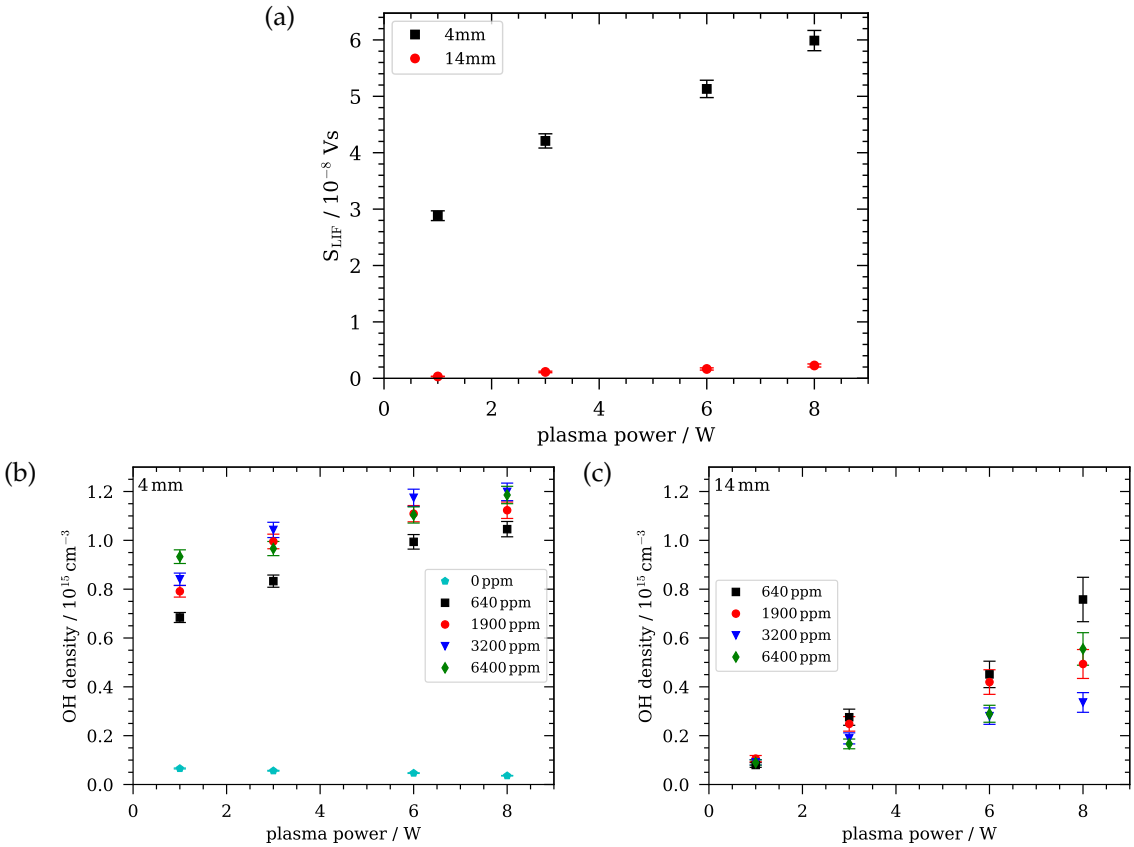

Figure 4.2.17: (a) Relative OH LIF signal 4 mm and 14 mm from the capillary end for 640 ppm feed gas humidity and absolute OH density (b) 4 mm and (c) 14 mm from the capillary end for 640 ppm to 6400 ppm at varied plasma power. Measurements are taken at a gas flow rate of 1 slm.

water vapour concentration in the effluent. While even slight changes in the water concentration have a significant effect on quenching and can therefore alter the trends of the OH density like in the case of varies feed gas humidity. The trend stays consistent here but the increase of the OH density with plasma power is weaker.

For 0 ppm, only a small OH density around $5 \times 10^{13}\,\mathrm{cm}^{-3}$ is obtained for all plasma powers (figure 4.2.17b). With regard to the uncertainty of the diagnostics, no clear trend can be seen here. With added feed gas humidity, the signal gets stronger and increases with the plasma power. 14 mm from the capillary end, only Rayleigh signal is measured. Thus, no OH is detected at this point.

For 640 ppm, the absolute OH density increases from $6.8 \times 10^{14}\,\mathrm{cm}^{-3}$ at 1 W to $1 \times 10^{15}\,\mathrm{cm}^{-3}$ at 8 W. At 6400 ppm feed gas humidity, the rising trend continues. Here, the increase is from $9.3 \times 10^{14}\,\mathrm{cm}^{-3}$ to $1.2 \times 10^{15}\,\mathrm{cm}^{-3}$ from 1 W to 8 W plasma power.

At 14 mm distance (figure 4.2.17c), the OH density has decreased significantly to

$8.0 \times 10^{13}\,\mathrm{cm}^{-3}$ at 1 W and $7.6 \times 10^{14}\,\mathrm{cm}^{-3}$ at 8 W for 640 ppm. For higher feed gas humidity levels, this decrease is even more pronounced. The absolute OH density equates to $9.0 \times 10^{13}\,\mathrm{cm}^{-3}$ for 1 W and $5.6 \times 10^{14}\,\mathrm{cm}^{-3}$ for 8 W. A linear increase is observed 14 mm from the capillary end.

Hence, only a minor amount of OH is left in the effluent when treating liquids at larger distances as it was performed by Schüttler et al. [35]. As the OH density decreases with increasing distance in the effluent, reduction of the interaction of OH with treated liquid samples can easily be achieved by small increases in the distance between the capillary end and the liquid surface.

The linear increase in the OH density with plasma power can be explained by the energy provided. The energy coupled into the plasma through electron heating provides energy for both elastic and inelastic collisions. Whereas the former contributes mostly to heating the plasma, the latter drives dissociation and ionisation inside the plasma. In first approximation, the more energy is provided, the more OH is produced through dissociation.

The observed trend matches the results presented by Schüttler et al. [35, 36] who have also found a linear increase.

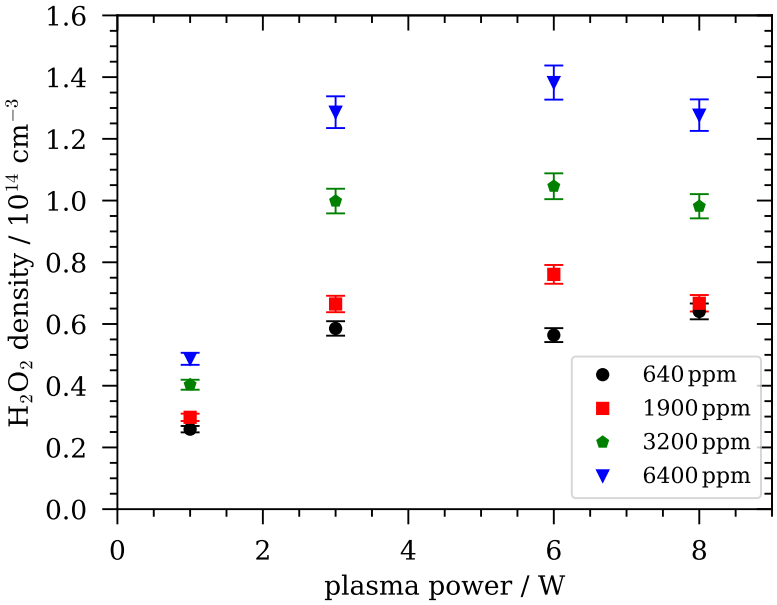

Figure 4.2.18: H_2O_2 density in the far field for varied plasma power at a gas flow rate of 1 slm.

In contrast to the monotonous increase of OH with increasing plasma power, the **H_2O_2 production** (figure 4.2.18) reaches a maximum at 6 W for feed gas humidity levels above 640 ppm. Up to 3 W plasma power, the H_2O_2 density increases with increasing plasma power. At higher plasma powers, the increase levels off.

For 640 ppm, a rather plateau like shape is observed from 3 W to 8 W. The maximum H_2O_2 concentration accounts to 10.46×10^{13} cm^3 at 1900 ppm and 13.82×10^{13} cm^3 at 6400 ppm, both at 6 W. For a feed gas humidity of 640 ppm, the highest H_2O_2 density has not been found to be at 6 W but 8 W with 6.41×10^{13} cm^3. Deviation of the trend here may rather result from the fitting routine than truly be a dip in the density. As the Gaussian background is fitted simultaneously with the spectrum, error minimisation may lead to an overestimation of the Gaussian background and resulting underestimation of the H_2O_2 density especially for spectra with weak H_2O_2 signal and some noise due to water.

Simulations of the H_2O_2 density at a distance of 24 mm from the plasma source presented in [36] revealed a similar trend, albeit at lower power levels. The concentration of H_2O_2 shows a sharp increase up to 2.5 W plasma power, followed by a gradual decline. In contrast, measurements conducted in the liquid phase did not exhibit a decrease but instead show a plateau. It is possible that the accumulation of H_2O_2 in the liquid diminished the slight decrease observed in the gas phase, thereby reducing the overall decline of H_2O_2 concentration at high plasma powers [36].

One potential mechanism influencing this trend is the gas temperature increase with rising plasma power (see section 4.1). As chemical reaction rates are temperature-dependent, temperature variations can have a significant impact on the plasma chemistry. Specifically, for H_2O_2, its concentration is known to decrease with increasing temperature [19]. As mentioned earlier in the discussion of humidity variation, one of the main loss mechanisms for H_2O_2 is OH. As the OH density increases with higher dissipated plasma power, loss via OH becomes more likely.

Additionally, studies have shown that the electron density in the plasma also rises with increasing plasma power [94, 95]. This heightened electron density leads to enhanced electron impact dissociation of water, resulting in the generation of more OH. While this enhanced dissociation may contribute to the formation of H_2O_2 at lower powers, where the OH concentration remains relatively low, it can potentially contribute to the destruction of H_2O_2 at higher plasma powers [36].

In conclusion, the OH density increases with rising plasma power. The H_2O_2 density, however, levels off after an initial increase up to 3 W and then slightly decreases above 6 W plasma power. At low plasma powers, the plasma power enhances the OH production and thus the formation of H_2O_2. As the OH production further intensifies for higher plasma powers, it does not only contribute to the formation but also loss of H_2O_2 leading to a decrease at higher plasma powers.

Power modulation

Regarding energy efficiency, low plasma powers up to 6 W are favourable to higher ones as the cost of energy can be reduced while still reaching desired H_2O_2 production. Energy efficiency can be further improved by pulsing the plasma. While pulsed plasmas are often used to reduce heating, their operation also saves energy compared to permanently operated plasmas. By employing pulsed operation, energy consumption can be optimised while maintaining the necessary production levels of H_2O_2. This approach ensures efficient utilisation of energy resources, contributing to overall cost savings and sustainability in plasma-based processes.

This "power modulated operational mode" [19] is characterised by the ratio of plasma-on and plasma-off time, namely duty cycle and frequency, which determines the length of each on-off cycle. The plasma RF-frequency is then modulated with an overlaying rectangle pulse. An overview of the frequency corresponding to the number of pulses per residence time is given in table A.1.

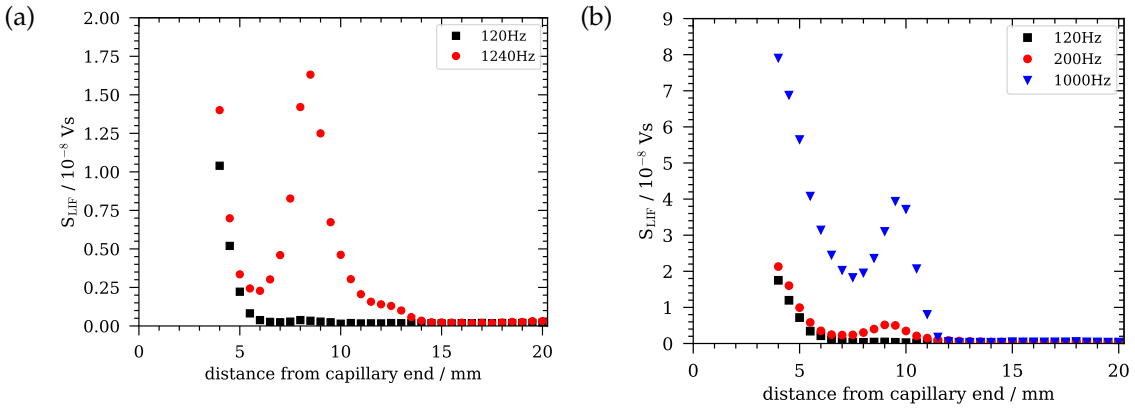

Figure 4.2.19: Relative OH LIF signal for varied distance from capillary end for (a) 10 % and (b) 50 % duty cycle and varied frequency. Measurements taken at 1 slm helium with 6400 ppm feed gas humidity and 6 W unmodulated plasma power.

As there is no constant **OH production** in the power modulated operational mode, a triggering system is used to account for the additional temporal component and fix the temporal point of observation. A scan of the OH LIF signal at varied distance from 0 mm to 20 mm from the capillary end at a fixed time is shown in figure 4.2.19 to determine the dynamics of OH in the effluent in the pulse modulated case. For a frequency of 120 Hz, the signal decays steadily with increasing distance for both 10 % and 50 % duty cycle. For higher frequencies in the contrary, the OH LIF signal first decreases and then increases again up to a maximum around 8.5 mm distance from the capillary end.

The unmodulated mode is characterised by a constant flux of OH radicals in the effluent. When regarding the power modulated operational mode, this shifts towards "packets" that leave the capillary jet and travel through the effluent. The observed maxima correspond to the OH produced during the plasma-on time and transported by the gas flow into the effluent. The transport of these OH packets in the effluent is determined by the gas flow rate. Therefore, the OH density peaks at approximately the same distance from the capillary end regardless of duty cycle and frequency for a constant gas flow rate. While these packets travel, the OH density decreases as it reacts with other particles in the effluent. Therefore, the intensity of the OH LIF signal decreases. In addition, the amount of air increases with increasing distance from the capillary. Therefore, more packets further away from the capillary end may be present but not detectable anymore due to quenching.

In the following, the OH LIF signal and calculated OH density 4 mm from the capillary end are regarded only as there is no OH LIF signal at 14 mm distance anymore. The results depending on the number of pulses per residence time are shown in figure 4.2.20.

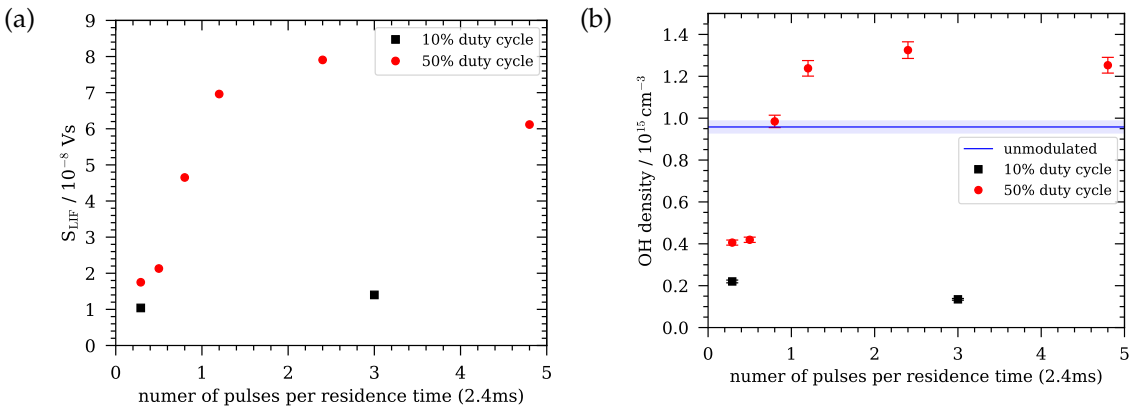

Figure 4.2.20: (a) Relative OH LIF signal and (b) absolute OH density 4 mm from capillary end for varied frequency in power modulated operated mode at 10 % and 50 % duty cycle. Measurements taken at 1 slm helium with 6400 ppm feed gas humidity and 6 W unmodulated plasma power.

The relative OH LIF signal is shown in figure 4.2.20a. For 50 % duty cycle, the OH LIF signal increases with an increasing number of pulses per residence time and levels off above 1 pulse per residence time. Towards 5 pulses per residence time, the OH LIF signal decreases slightly again. At 10 % duty cycle, the OH LIF signal is significantly lower and increases only slightly with an increasing number of pulses per residence time.

The calculated absolute OH density is in figure 4.2.20b. For better comparison,

the mean absolute value obtained for the same plasma parameters without power modulation is displayed. The absolute values show a similar trend to the relative ones. The only difference is that the OH density does not decrease as significantly towards a higher number of pulses per residence time at 50 % duty cycle and that the absolute OH density for 10 % increases quite significantly. For the determination of the absolute values, it was assumed that no air intrusion is present. For 10 % duty cycle, the humidity is constant at 640 ppm. For 50 % duty cycle and a higher number of pulses per residence time, there is a significant increase in the OH production and a decrease in the humidity is deduced from the evaluation of quenching. The fitted humidity then accounts to 640 ppm, 640 ppm, 640 ppm, 530 ppm, 480 ppm and 620 ppm. For the highest OH densities, the deviation between feed gas humidity and estimated humidity in the effluent is the largest which is consistent with the assumption that the water vapour concentration must decrease with increasing production of species that are formed from dissociation of water.

The absolute number density accounts to $2.6 \times 10^{14}\,\mathrm{cm}^{-3}$ at 0.2 and $8.3 \times 10^{14}\,\mathrm{cm}^{-3}$ at 3 pulses per residence time for a duty cycle of 10 %. At 50 % duty cycle, the OH density increases from $4.5 \times 10^{14}\,\mathrm{cm}^{-3}$ at 0.2 to a maximum of $1.3 \times 10^{15}\,\mathrm{cm}^{-3}$ at 2.4 pulses per residence time. The determined OH density may be higher than the one obtained without power modulation because the loss via OH is less pronounced as the species towards the edges of the packets face pure helium which does not contribute to the loss of OH as other molecules do. Time-resolved LIF would offer a deeper insight into the phenomenon and allow for spatial and temporal tracing of the motion and density decrease inside the OH packets.

The measured **H_2O_2 densities** are shown in figure 4.2.21. For a duty cycle of 10 %, the plasma produced H_2O_2 concentration is around a factor 5 lower than for the unmodulated operational mode. It rises slightly up to 2 pulses per residence time and then decreases again. For a duty cycle of 50 % on the contrary, the H_2O_2 density is slightly higher in comparison to the unmodulated mode and therefore rather unaffected by the applied modulation. It first increases from $1.39 \times 10^{14}\,\mathrm{cm}^{-3}$ at 0.5 pulses per residence time up to $1.49\,\mathrm{cm}^{-3}$ at 0.8 pulses per residence time and stays constant nearly constant for higher pulse numbers. At 5.8 pulses per residence time, a density of $1.56 \times 10^{14}\,\mathrm{cm}^{-3}$ is reached.

Regarding the gas temperatures, pulsed operation of a plasma jet is accompanied by lower temperatures [96]. Both components and gas temperature do not heat as strongly as in continuous operation. Temperature measurements at 6 W and 1 slm gas flow rate for the power modulated operational mode (not shown in this work) yield approximately $(89 \pm 4)\,^{\circ}\mathrm{C}$ for 50 % duty cycle and frequency varied

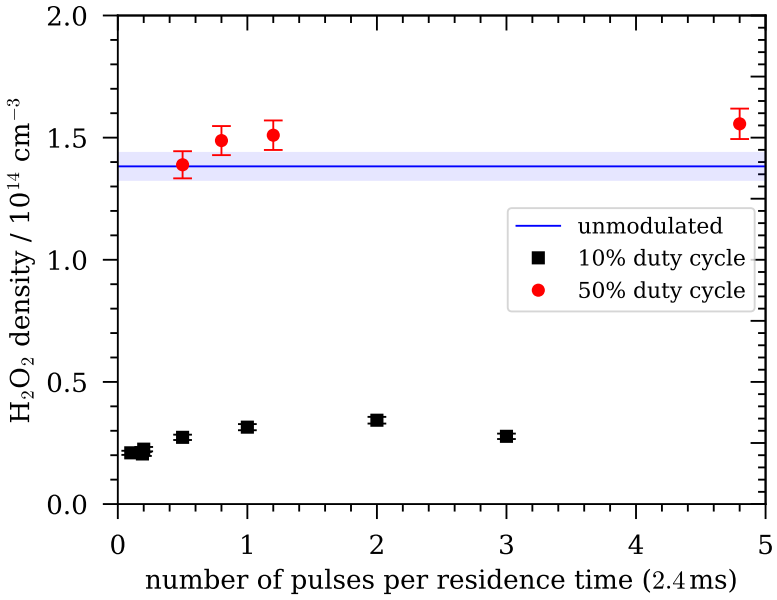

Figure 4.2.21: Absolute gas phase H_2O_2 density derived from FTIR measurements in a multipass cell in power modulated operational mode. Measurements taken at 1 slm helium with 6400 ppm feed gas humidity and 6 W unmodulated plasma power.

between 208 Hz and 2000 Hz. For a duty cycle of 10 % and frequencies of 42 Hz to 1250 Hz, the temperature is even lower around (42.3 ± 1.3) °C. In comparison to the values obtained for the continuous case (figure 4.1.3), these prove to be indeed significantly lower.

Lower temperatures both enhance the production and lower the destruction of H_2O_2 and are therefore favourable to higher temperatures. In addition, OH production is the dominant factor for the production of H_2O_2. OH is mainly formed in the plasma and rises to its maximum density after 0.36 ms (6 mm) in continuous mode where it then saturates [36]. Comparing this to the plasma-on time and number of pulses per residence time, we see that in the case of a duty cycle of 50 %, the OH density can rise to its maximum. Therefore, the effect on the H_2O_2 production is minimal. Lower gas temperatures can even enhance the OH and therefore H_2O_2 production.

Regarding lower duty cycles and higher frequencies, this assumption does not hold anymore. The plasma-off time is long enough for significant loss of the OH molecules as they are known to be highly reactive. In addition, plasma-on time is not sufficient to reach the maximum production and therefore the initial OH density is already reduced which then also results in a decreased H_2O_2 production as it mainly relies on three-body recombination of OH.

Vasko et al. [19] present a chemical model adapted to the power modulated operational mode. In experimental studies, they have also found for their parameters

that power modulation yields the same H_2O_2 concentration as operation in continuous mode. Similar results as presented here have been found by Schüttler et al. in measurements of H_2O_2 in the liquid [36]. For low duty cycles, the H_2O_2 concentration in the liquid is significantly lower than in the unmodulated case. For a duty cycle of 50 %, the H_2O_2 concentration increases for low pulse numbers and then comes to saturation around the value obtained in the unmodulated case.

In conclusion, similar trends have been found for the OH and H_2O_2 densities in the power modulated operational mode. The density of both species is significantly lowered in comparison to the unmodulated case for a duty cycle of 10 %. For a duty cycle of 50 %, the density obtained for both species is in the range of the unmodulated case and is even slightly elevated in comparison to the unmodulated mean value. Thus, power modulation is an effective strategy to decrease the energy input without affecting the H_2O_2 production significantly.

Gas flow rate

In the power modulated case, the excitation time inside the plasma is adapted by applying an overlaying pulse. Additionally, also the residence time inside the plasma can be alternated. For this, alternation of the gas flow rate is studied. Next to the theoretical point of view, from which studying the effect of varied residence time is interesting to improve the understanding of the plasma behaviour, gas is one of the main consumables. Therefore, the effect of the gas flow and corresponding residence time in the plasma on the achieved H_2O_2 concentration is desired.

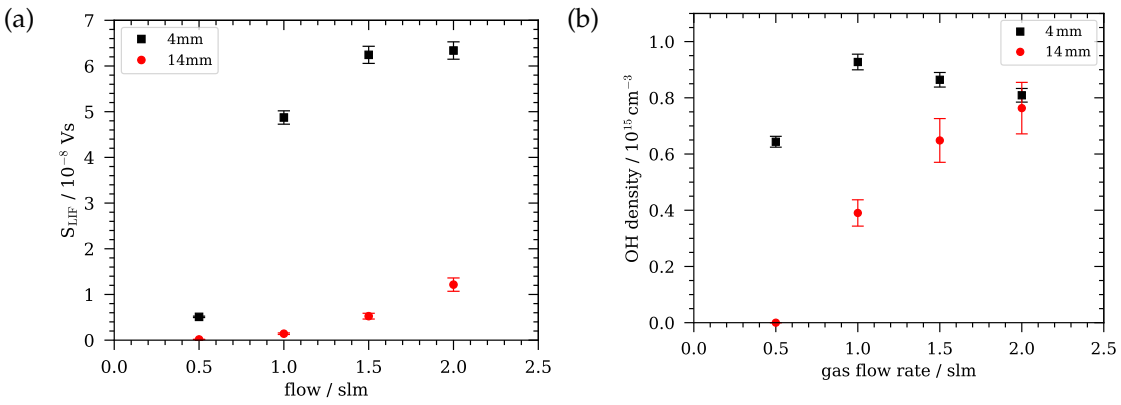

Figure 4.2.22: (a) Relative OH LIF signal and (b) absolute OH density at 4 mm and 14 mm from capillary end with regard to varied air admixture and for humidity around 640 ppm for varied gas flow rate. Measurements taken at 640 ppm feed gas humidity and 6 W plasma power.

The results on the **OH production** in the effluent for all gas flow rates are shown

in figure 4.2.22. The obtained relative LIF signal is shown in 4.2.22a. 4 mm from the capillary end, the OH LIF signal increases with increasing gas flow rate up to 1.5 slm. For higher gas flows, the OH LIF signal reaches a plateau from 1.5 slm to 2 slm and no significant increase in the LIF signal can be detected anymore. 14 mm from the capillary end, the trend of the relative OH LIF signal is opposite to the one close to the capillary end. Here, the observed OH LIF signal increases monotonously with increasing gas flow rate and rather follows an exponential increase.

This deviation is related to quenching in the relative values. With varying gas flow rate, the ratio of helium and air at the point of observation changes. Therefore, the conditions are not the same and thus, the trend is distorted as shared conditions are needed for comparability but are only given close to the capillary end where there is mainly a humidified helium atmosphere. Hence, air admixtures of 40 %, 18 %, 8 % and 3 % for 0.5 slm to 2 slm are used for the calculation of the density. The amount of air is deduced from the decay time of the signal with the estimation that the water vapour concentration is around 640 ppm and minor deviations do not influence the density greatly as quenching by air dominates because the fraction of water vapour from the feed gas is only a fraction of the air at the point of observation.

The absolutely calibrated results with regard to water consumption and changes of the gas admixture depending on the gas flow rate are shown in figure 4.2.22b. Assuming a pure helium atmosphere 4 mm from the nozzle for 1 slm to 2 slm and 2.3 % air admixture for 0.5 slm as shown in section 4.2.2, OH densities in the order of $10 \times 10^{15}\,\mathrm{cm}^{-3}$ are obtained. For these, water consumption is also regarded and the fitted water vapour concentration in the effluent accounts to 640 ppm, 610 ppm, 400 ppm and 320 ppm. The obtained trend is similar to the relative OH LIF signal, but the density rather follows a rapid increase that comes to saturation above 1 slm gas flow rate. By regarding quenching for 0.5 slm, the modelled reference signal becomes smaller and thus, the calculated density increases compared to the relative trend. 4 mm from the capillary end, the OH density first increases from $6.4 \times 10^{14}\,\mathrm{cm}^{-3}$ at 0.5 slm to $9.3 \times 10^{14}\,\mathrm{cm}^{-3}$ at 1 slm gas flow rate. Above, the OH density gradually decreases to $8.1 \times 10^{14}\,\mathrm{cm}^{-3}$ at 2 slm gas flow rate. The decrease at high gas flow rates may be caused due to the fitting routine. The LIF signal at a gas flow rate of 2 slm features a slightly noisy decay, therefore the fit of the signal without noise slightly differs from the integration over the full signal.

14 mm from the capillary end, a monotonous increase in the OH density is observed in the examined regime. For 0.5 slm gas flow rate, only Rayleigh signal is detected, therefore the OH density is below the detection limit here. At

1 slm gas flow rate, the OH density is at $3.9 \times 10^{14}\,\mathrm{cm}^{-3}$ and further increases to $7.6 \times 10^{14}\,\mathrm{cm}^{-3}$ at 2 slm gas flow rate. The increase levels off above 1.5 slm.

OH is formed on a very fast time scale and reaches its maximum density within a few hundred nanoseconds inside the plasma [36]. Thus, the residence time in the plasma at 2 slm is still sufficient to reach the maximum OH production. The OH density in the effluent would then be expected to be close to constant.

At 0.5 slm gas flow rate, the transport time up to the point of observation is sufficiently large for a significant loss of OH. Hence, the measured OH density is lower. The decay above 1 slm close to the capillary end may be linked to the loss of OH via reaction with OH to H_2O_2 before being measured in the effluent. This effect especially sets in for higher OH levels. In addition, uncertainty in the fitting routine becomes more pronounced here.

The trend at 14 mm is likely a result of several factors including air intrusion and transport time. A higher air admixture offers several collision partners for OH and enhances the loss. This is especially prominent for 0.5 slm where the amount of air is so high that no LIF signal is measured anymore which is likely caused by a combination of quenching and a very low OH density. If the OH density was high and only quenching caused the small signal, the amplitude of the signal would be higher as it is the case closer to the capillary. Here, the amplitude of the recorded signal is close to the amplitude of the Rayleigh signal. Additionally, the time of the species that have passed since leaving the plasma differs when regarding the same point in space. For 2 slm, the period between leaving the plasma and reaching the observation point is four times smaller than for 0.5 slm. Thus, the timescale for OH to react with other species is longer for lower gas flows.

The trend of the absolute OH density observed 14 mm from the capillary end is in good agreement with the measurements by Schüttler et al. [36] in the liquid. They have found that for 0.5 slm, the OH density is very low. With increasing gas flow, the OH density gradually increases until the increase slows above 1.5 slm. Also, the order of magnitude of the calculated OH density matches the results which lay in the order of $1 \times 10^{14}\,\mathrm{cm}^{-3}$ to $1 \times 10^{15}\,\mathrm{cm}^{-3}$ for 640 ppm.

For the determination of **H_2O_2 density** in the effluent, the transport time of the species from the plasma to the multipass cell must be considered. While a variation of the gas flow changes the residence time of the particles in the plasma, also the transport time of the particles in the system is altered. Therefore, a steady state in the multipass cell is reached at a later point for low gas flow rates. To account for this, the wait time for the spectra is adapted and all H_2O_2 spectra are

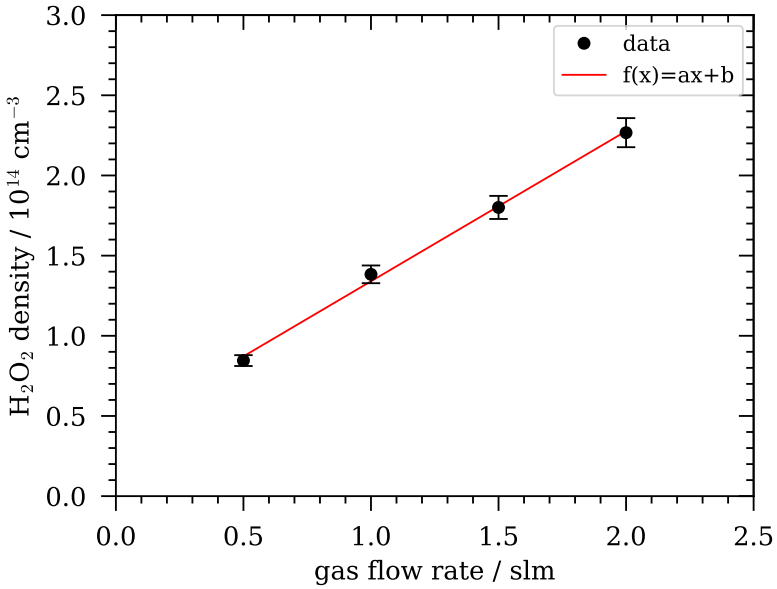

Figure 4.2.23: H_2O_2 density in the far field for varied gas flow rate with applied linear fit. Measurements taken for 6400 ppm feed gas humidity and 6 W plasma power.

taken when the gas admixture in the multipass cell is at equilibrium. Additionally, higher transport time in the system may influence the surface losses of H_2O_2 in the tubes. Due to the choice of the material, these are assumed to be relatively low.

In the case of a closed system, the travel time of the species in the effluent with air admixture is not regarded. This deviation from an open system is expected to have a minor effect though as Jeß [34] has shown in his bachelor's thesis, that the residence time is the main determinant for the H_2O_2 production and the travel time in the atmosphere has only a minor effect.

The gas flow was varied between 0.5 slm to 2 slm for 6400 ppm humidity concentration at 6 W dissipated plasma power. The experimental results (figure 4.2.23) show, that the measured H_2O_2 density increases linearly with the gas flow.

The absolute number H_2O_2 density accounts to $8.45 \times 10^{13}\,\mathrm{cm}^{-3}$ at 0.5 slm and increases to $2.27 \times 10^{14}\,\mathrm{cm}^{-3}$ at 2 slm. A linear fit of the data in the range of 0.5 slm to 2 slm then yields the relation $\rho_{H_2O_2}(Q) = (9.4 \pm 0.4)10^{13}\mathrm{cm}^{-3}\,\mathrm{slm}^{-1} \cdot Q + (4.0 \pm 0.5)10^{13}\mathrm{cm}^{-3}$ for the H_2O_2 density depending on the gas flow rate Q with an R^2 value of 0.9978.

While the linear trend holds for lower gas flow rates, it would be expected that the H_2O_2 density is nearly constant in the regarded regime as the OH density does not change drastically and the measured variation is rather linked to the transport than production. In addition, the residence time in the plasma is sufficient to reach the maximum H_2O_2 density for higher gas flow rates. If the gas flow rate

was increased even further, the resulting decrease of the residence time would eventually lead to a decrease in the H_2O_2 production because the residence time inside the plasma is not sufficient anymore to produce the same amount of H_2O_2.

Vasko et al. [19] measured H_2O_2 in a plasma treated liquid. They report, that the H_2O_2 concentration increases with increasing gas flow rate and decreasing residence time respectively. A linear trend has also been observed by Schüttler et al. [36]. Measurements of the H_2O_2 concentration in a plasma-treated liquid show a linear increase with the gas flow rate. For the gas phase, it is deduced that the H_2O_2 density is constant here, as the increase is an effect of the larger number of particles reaching the liquid surface in a fixed amount of time for higher gas flow rates.

This is in contrast to the densities observed here. The contradiction between the results is attributed to the diagnostics. In case of the FT-IR measurements, adsorption of H_2O_2 to the walls becomes a main loss channel for H_2O_2 in the gas phase. The lowered densities were already contributed to this. The measurements here show, that this is likely the explanation as for higher gas flow rates, the flux to the walls is reduced and thus, a larger amount of the H_2O_2 species stays inside the gas phase. In the future, heating of the multipass cell should be increased further to reduce adsorption to the walls. In this case, potential losses due to additional heating of the gas inside the multipass cell must also be reconsidered though.

In conclusion, variation of the gas flow rate is used to vary the residence time of the particles inside the plasma. The OH density increases up to 1 slm gas flow rate 4 mm from the capillary and comes to a slight decrease for higher gas flow rates. 14 mm from the capillary end, the OH density increases monotonously with increasing gas flow rate but levels off above 1.5 slm. The H_2O_2 density increases linearly with increasing gas flow rate across the whole investigated range which is attributed to adsorption of H_2O_2 to the walls. With gas flow rate, the OH density increases where the liquid sample is positioned. Increasing the distance between plasma and sample to treat can be used to decrease the density of the highly reactive OH, which is damaging to the enzymes, while H_2O_2 is known to be a rather stable species and is therefore rather unaffected by small changes in the distance.

4.3 Adaption of the experiment to meet future needs

While "green" hydrogen peroxide production is desirable from an environmental point of view, technology also needs to meet economic needs. Here, financial

calculations demand comparability with existing technologies. For this reason, the cost of material resources like gas and energy costs have to be reduced as far as possible while still keeping a sufficient output for biocatalysis. First approaches for optimisation have already been tested, like reduction of the energy input by power modulation and reduction of gas consumption.

Cost of material can be reduced by means of choice of setup components and choice of feed gas among others. The first option becomes of special interest when scaling comes into action. While research is performed on a single device, mass production uses very different technical facilities. One cost factor is the choice of pipes. As rubber stores humidity and can intensify surface reactions and deposition, stainless steel is recommended for the piping, even though it is more cost-intensive [26].

The latter option, which is of higher interest from a research point of view, is the use of a feed gas other than helium. While atmospheric pressure plasmas operated with helium have been studied extensively over the past decades [32, 97, 98], helium is a limited resource facing growing demand from various industries [99]. While the use of helium is not environmentally damaging, it is not a long-term solution either. Therefore, early investigation of alternatives is a key factor in search for green production of hydrogen peroxide. The limitation of helium on the market causes high prices of the gas which is expected to increase even further in the upcoming years [100, 101].

One possible alternative to the use of helium is argon. Argon has already proven to be a suitable feed gas for the production of OH and H_2O_2 in the plasma [19, 27, 40]. Therefore, argon is a promising candidate as an alternative feed gas. As it features very different discharge behaviour though, measurements should be selectively repeated for argon to fully understand the characteristics of the argon discharge.

Jeß [34] performed first experiments on the capillary jet operating in argon feed gas during his Bachelor's thesis. Here, it was shown that the discharge behaviour of argon differs significantly from the one of helium. During first preliminary experiments performed during this work, this difference could also be identified.

Stable operation of the argon plasma is only possible at higher plasma power. This further aggravates with increased feed gas humidity. Feed gas humidity levels over 640 ppm cannot be realised under 12 W at stable discharge operation. In addition, ignition is only possible using external support like a high-frequency spark tester. This adds additional needs for automation of the setup as the plasma can only be turned on manually and not by the power supply. The discharge

dimensions further deviate from the ones of a helium plasma. While the helium plasma burns homogeneously between the electrodes, the argon plasma is either not fully developed along the whole discharge channel between the electrodes in the case of lower plasma power or further extends into the capillary behind the electrode in the case of higher plasma powers. Thus, analysis of the plasma under defined parameters is more complicated.

In terms of temperature, the gas temperature is heavily elevated for operation with argon. This is caused by both the higher plasma power which is necessary for stable operation and the different thermal conductivity and behaviour of argon. First measurements of the OH and H_2O_2 density showed that the OH LIF signal increases in the first few millimetres behind the capillary end for 1 slm gas flow rate and then decreases. For a gas flow of 2 slm, the signal decreases quickly without an initial increase. Absolute number densities were not calculated in this work as the model was optimised for helium and rate coefficients for argon are not included yet but can be found in literature [82]. Measurements of H_2O_2 for argon as a feed gas are not possible for the setup used here as the plasma cannot be ignited or runs extremely unstable. Instead, electrodes and a capillary with a width of 4 mm at identical distance of the electrodes were used. Here, only traces of H_2O_2 could be measured.

This shows, that argon requires more intensive work to understand its behaviour. Especially the temperature is expected to be a crucial factor when examining the OH and H_2O_2 production as the production and loss rates are temperature dependent. In addition, the setup must be adapted accordingly to withstand higher temperatures over a long period of time.

During the investigation of argon as a feed gas, the energy consumption and stability should be carefully regarded in terms of competitiveness with other solutions for hydrogen peroxide production. Until now, argon seems to be disadvantageous in terms of H_2O_2 production, energy consumption and stability. In favour of argon is its availability and cost. These factors must be weighed against each other in the future.

Additionally, the above-mentioned use of a wider capillary enables the first steps towards scaling up the structure. First measurements of the H_2O_2 density in the effluent of the setup with a 4 mm wide capillary show that the trends are comparable with the ones found for the 1 mm capillary. The absolute densities are lower though. For 1 slm gas flow rate and 3200 ppm feed gas humidity at 6 W plasma power for example, the obtained H_2O_2 density is a factor of two lower in case of the wider capillary. Consequently, the assessment of energy efficiency and costs will become even more important when scaling is considered.

5. Conclusion and Outlook

This thesis focused on expanding the knowledge on the capillary plasma jet from the liquid system to the effluent and the densities of OH and H_2O_2 there. For this, temperature measurements were conducted, the spatially resolved gas mixture in the effluent was analysed and densities of OH and H_2O_2 were calculated.

The temperature measurements have revealed that the temperature of the effluent and plasma are nearly the same for a feed gas humidity up to 6400 ppm. The temperature of the effluent and therefore the temperature of the plasma, as well as the temperature of the plasma source's components, increase linearly with plasma power. Comparison of extrapolated thermocouple measurements and rotational temperature from optical emission spectroscopy show good agreement for feed gas humidity levels up to 640 ppm.

Laser-induced fluorescence was used to determine the air intrusion in the effluent and measure absolutely calibrated OH densities close to the capillary and at the position where a liquid sample is typically positioned. For this, the 4-level model presented by Verreycken et al. was adapted to account for quenching by water and air. Spatially resolved maps of the OH LIF signal show a more pronounced signal along the electrodes. The asymmetry decreases with increasing distance. Additionally, the signal decreases exponentially with increasing distance. Maps of the air admixture were derived from the fluorescence lifetime of the OH species. A uniform atmosphere of humidified helium was found centrally beneath the capillary end for higher gas flow rates. For low gas flow rates, air intrusion is already measurable close to the capillary end. With increasing distance, the air admixture increases along the z-axis. The width of the gas stream stays constant along the whole investigated range up to 14 mm.

In summary, OH densities in the order of $1 \times 10^{15}\,\mathrm{cm}^{-3}$ were found close to the capillary end. These decrease by more than half an order of magnitude at the sample position. H_2O_2 densities in the order of $1 \times 10^{14}\,\mathrm{cm}^{-3}$ were found. The H_2O_2 density rises with humidity after an initial rapid increase while the OH density levels off above a few hundred ppm feed gas humidity. The trends for varied power are reversed to the ones for varied humidity. The OH density increases linearly with power, and the H_2O_2 density levels off above 3 W. Both OH and H_2O_2 densities are in the same order as for the unmodulated case for a duty cycle of 50 % and multiple pulses per residence time. For lower duty cycles, both

densities are significantly lowered. With increasing gas flow rate, the OH density increases when measured further away from the capillary end. The H_2O_2 density increases linearly with increasing gas flow rate in the multipass cell which is attributed to adsorption and not increased production of H_2O_2 in the plasma.

Except for H_2O_2 under the variation of the gas flow, the trends of the density of OH and H_2O_2 in the gas phase show a high degree of agreement with previous measurements in the project performed on the species densities in a plasma treated liquid. This highlights the close linking of the individual subsystems of plasma, effluent and liquid and indicate a high transfer of species from the gas phase to the liquid.

This work shows that it is possible to obtain trends for the OH density in the effluent for several parameter variations if close care is taken to correctly determine the influence of the air admixture and humidity on quenching and VET. Values in an order of magnitude were obtained that match the range expected from other studies. Therefore, LIF has proven to be a promising diagnostical method for further investigation of the source. Evaluation of the obtained densities must be performed carefully with regard to the high uncertainty resulting from the calculation of the laser spectral irradiance and quenching and VET.

With regard to optimisation of the setup, it was found that plasma power should not exceed 6 W in the case of helium to obtain a maximum yield of H_2O_2 while keeping the OH density to a minimum and reducing the energy costs. Additionally, the plasma should be operated in pulsed mode as similar OH and H_2O_2 densities can be achieved here at significantly reduced energy input. The feed gas humidity can be used as a tool to scale the yield of H_2O_2 without increasing the OH density at the position of a liquid sample surface. Increasing the gas flow rate increases the OH density at the sample position and must therefore be weighed in terms of time savings, cost of resource and inhibition of enzymes due to contact with OH.

First attempts at optimising the setup and scaling the plasma volume have revealed the need for more detailed work on the dynamics of different feed gases and capillary geometries.

Future investigation of OH with LIF should focus on the spectral laser linewidth in detail which could not be performed during this thesis anymore due to defective laser pumps. In addition, the setup for time-resolved LIF was developed during this thesis and has proven to work during the measurements in power modulated operational mode. Further investigation offers a deeper insight into the transport dynamics of OH in the effluent and the development of a deeper

understanding of the mode. As this mode has been found to yield promising OH and H_2O_2 production with simultaneous improvement of energy efficiency, it is a propitious approach that is likely to contribute to the goal of project B11.

Finally, it can be concluded that the work in this thesis did not only contribute to the expansion of the knowledge of the plasma source to the effluent but also revealed information on the behaviour of both OH and H_2O_2 to parameter variation as well as information on the temperatures of the system and gas mixture in the effluent. The knowledge gained on the diagnostics helps to improve its application on atmospheric pressure plasma jets in ambient air and opens new fields of investigation for future works.

A. Appendix

Calculation of feed gas humidity

The calculation of the water vapour concentration in the feed gas is based on the pressure p_{vapour} of the vapour over water (hPa) depending on the water temperature T (K). According to the Antoine equation [86], this is

$$p_{\text{vapour}} = 1000 \cdot 10^{4.6543 - \frac{1435.264}{T - 64.848}}. \tag{A.1}$$

Taking into account, that only a fraction of the feed gas passes the bubbler, the water vapour concentration in the feed gas (ppm) computes to

$$c_{\text{H}_2\text{O, feed gas}} = 10^6 \cdot \frac{\phi_{\text{bubbler}}}{\phi_{\text{total}}} \cdot \frac{p_{\text{vapour}}(T)}{p_{\text{total}}} \tag{A.2}$$

where ϕ_{bubbler} is the gas flow through the bubbler, ϕ_{total} the total gas flow and p_{total} the total pressure in the system. As the jet is operated at atmospheric pressure, the total pressure is assumed to be close to atmospheric pressure. A mean value of (1013 ± 20) hPa is used for calculations.

Regarding the Gaussian maximum error $\Delta c_{\text{H}_2\text{O, feed gas}}$, this results in an error of

$$\Delta c_{\text{H}_2\text{O, feed gas}} = 10^6 \cdot \frac{\phi_{\text{bubbler}}}{\phi_{\text{total}}} \cdot \frac{p_{\text{vapour}}(T)}{p_{\text{total}}} \cdot \frac{1000 \cdot \log(10) \cdot 4.6543}{(T - 64.848)^2} \cdot \Delta T \tag{A.3}$$

assuming the contribution of the error of the gas flow through the MFC and the error of the total pressure to be negligible.

Parameters in power modulated operational mode

Table A.1: Parameters in power modulated operational mode. Table adapted from [36].

duty cycle / %	frequency / Hz	plasma-on time / ms	plasma-off time / ms	number of pulses per residence time
10	47	2.4	21.4	0.1
	67	1.5	13.4	0.2
	100	1.0	9.0	0.25
	200	0.5	4.5	0.5
	400	0.3	2.3	1
	833	0.1	1.1	2
	1250	0.1	0.7	3
50	208	2.4	2.4	0.5
	333	1.5	1.5	0.8
	500	1.0	1.0	1.2
	1000	0.5	0.5	2.4
	2000	0.3	0.3	4.8

Extrapolation of temperature from effluent to plasma

Table A.2: Parameters obtained from linear fit of temperature measurements in the effluent.

power / W	c_{H_2O} / ppm	a / °C mm^{-1}	b / °C	R^2	f
1	0	(-0.32 ± 0.05)	(57.9 ± 0.4)	0.93	(1.059 ± 0.019)
1	6400	(-0.341 ± 0.018)	(57.78 ± 0.14)	0.99	(1.064 ± 0.009)
6	0	(-1.49 ± 0.22)	(123 ± 3)	0.95	(1.13 ± 0.04)
6	6400	(-1.46 ± 0.09)	(136.0 ± 1.1)	0.99	(1.119 ± 0.012)
12	0	(-3.08 ± 0.21)	(209.1 ± 1.7)	0.98	(1.162 ± 0.029)
12	6400	(-3.96 ± 0.23)	(218.7 ± 1.8)	0.98	(1.199 ± 0.030)

Uncertainty estimation of rotational temperature

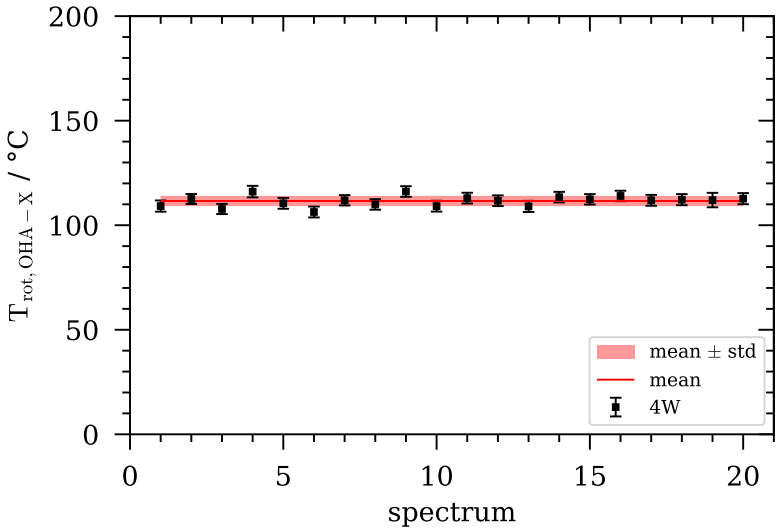

Figure A.0.1: Example for error estimation of rotational temperature from fit of series of 20 spectra. Measurement taken at gas flow rate 1 slm with 670 ppm feed gas humidity at 4 W plasma power.

Parameters for OH LIF model

Table A.3: Experimental parameters of laser and laser-induced fluorescence measurements. Layout adapted from [43].

Parameter	Description	Value
λ_L	Laser wavelength	282.58 nm
$\Delta\lambda_L$	Linewidth of laser	0.7 pm
$\Delta\nu$	Bandwidth of laser	$(8.9 \pm 2.6)\ \mathrm{m}^{-1}$
Γ	Overlap integral	0.17
A_L	Area of the laser beam	$(11\,300 \pm 3000)\ \mu\mathrm{m}^2$
E_L	Laser energy per pulse	$(7.4 \pm 0.4)\ \mu\mathrm{J}$
τ_L	temporal FWHM of laser pulse	(11.5 ± 2.2) ns
Δx	Length of detection volume	$(200 \pm 4)\ \mu\mathrm{m}$
Δy	Width of detection volume	$(200 \pm 4)\ \mu\mathrm{m}$
Δs	Spatial FWHM of the laser beam at the observation point	$(60 \pm 10)\ \mu\mathrm{m}$
η	calibration factor	$(12\,000 \pm 500)\ \mathrm{V\,sr\,J}^{-1}$

Table A.4: Total quenching (electronic and vibrational relaxation, Q) and vibrational relaxation (V) rates for inelastic collisions of OH with He, H_2O, N_2 and O_2 given in $10 \times 10^{17}\,\mathrm{m^3/s}$ for OH A ($\nu' = 0,1$).

Collider	Q_{00}	Q_{11}	V_A	Ref.
He	0	0.0040±0.0015	0.002	[102]
H_2O	69.1±5.0	66±4	7.3±0.5	[103–106]
N_2	2.8±1.2	23.6±1.5	23.3±1.5	[103, 104]
O_2	9.6	20.6	2.1	[103, 104]

Table A.5: Coefficients used in the 4-level model. Table adapted from [40].

Parameter	Value	Ref.
$\lambda_{A_{00}}$	308.9 nm	[56]
$\lambda_{A_{11}}$	314.535 nm	[56]
$\lambda_{A_{10}}$	282.792 nm	[56]
A_{00}	$1.451 \times 10^{-6}\,\mathrm{s^{-1}}$	[56]
A_{11}	$8.678 \times 10^{-6}\,\mathrm{s^{-1}}$	[56]
A_{10}	$4.606 \times 10^{-6}\,\mathrm{s^{-1}}$	[56]
B_{12}	$1.8\,\mathrm{mJ^{-1}}$	[56]
B_{21}	$2.8\,\mathrm{mJ^{-1}}$	[56]
$2f_B^{\nu''=0,J''=2.5}$	0.153	[40, 78]
$2f_B^{\nu'=1,J'=1.5}$	0.1	[40, 78]
V_X	$1.1 \times 10^5\,\mathrm{s^{-1}}$	[40]

Bibliography

[1] M. Laroussi: Nonthermal decontamination of biological media by atmospheric-pressure plasmas: review, analysis, and prospects. *IEEE Transactions on Plasma Science* 30.4, 2002. DOI: 10.1109/TPS.2002.804220.

[2] G. Daeschlein et al.: Antibacterial Activity of an Atmospheric Pressure Plasma Jet Against Relevant Wound Pathogens in vitro on a Simulated Wound Environment. *Plasma Processes and Polymers* 7.3, 2010. DOI: 10.1002/ppap.200900059.

[3] G. Daeschlein et al.: Skin decontamination by low-temperature atmospheric pressure plasma jet and dielectric barrier discharge plasma. *Journal of Hospital Infection* 81.3, 2012. DOI: 10.1016/j.jhin.2012.02.012.

[4] T. Bernhardt et al.: Plasma Medicine: Applications of Cold Atmospheric Pressure Plasma in Dermatology. *Oxidative Medicine and Cellular Longevity* 2019, 2019. DOI: 10.1155/2019/3873928.

[5] A. Khlyustova et al.: Important parameters in plasma jets for the production of RONS in liquids for plasma medicine: A brief review. *Frontiers of Chemical Science and Engineering* 13.2, 2019. DOI: 10.1007/s11705-019-1801-8.

[6] K. D. Weltmann et al.: Atmospheric-pressure plasma sources: Prospective tools for plasma medicine. *Pure and Applied Chemistry* 82.6, 2010. DOI: 10.1351/PAC-CON-09-10-35.

[7] C. Sarra-Bournet et al.: A study of atmospheric pressure plasma discharges for surface functionalization of PTFE used in biomedical applications. *Journal of Physics D: Applied Physics* 39.16, 2006. DOI: 10.1088/0022-3727/39/16/S03.

[8] K. Fricke et al.: Investigation of Surface Etching of Poly(Ether Ether Ketone) by Atmospheric-Pressure Plasmas. *IEEE Transactions on Plasma Science* 40.11, 2012. DOI: 10.1109/TPS.2012.2212463.

[9] O. V. Penkov et al.: A review of recent applications of atmospheric pressure plasma jets for materials processing. *Journal of Coatings Technology and Research* 12.2, 2015. DOI: 10.1007/s11998-014-9638-z.

[10] K.G. Kostov et al.: Surface modification of polymeric materials by cold atmospheric plasma jet. *Applied Surface Science* 314, 2014. DOI: 10.1016/j.apsusc.2014.07.009.

[11] C. Cheng, Z. Liye, and R.-J. Zhan: Surface modification of polymer fibre by the new atmospheric pressure cold plasma jet. *Surface and Coatings Technology* 200.24, 2006. DOI: 10.1016/j.surfcoat.2005.09.033.

[12] J. Van Durme et al.: Combining non-thermal plasma with heterogeneous catalysis in waste gas treatment: A review. *Applied Catalysis B: Environmental* 78.3, 2008. DOI: 10.1016/j.apcatb.2007.09.035.

[13] A. Mizuno: Industrial applications of atmospheric non-thermal plasma in environmental remediation. *Plasma Physics and Controlled Fusion* 49.5, 2007. DOI: 10.1088/0741-3335/49/5A/S01.

[14] L.A. Rosocha: Nonthermal plasma applications to the environment: gaseous electronics and power conditioning. *IEEE Transactions on Plasma Science* 33.1, 2005. DOI: 10.1109/TPS.2004.841800.

[15] A. Yayci et al.: Microscale Atmospheric Pressure Plasma Jet as a Source for Plasma-Driven Biocatalysis. *ChemCatChem* 12.23, 2020. DOI: 10.1002/cctc.202001225.

[16] A. Yayci et al.: Plasma-Driven in Situ Production of Hydrogen Peroxide for Biocatalysis. *ChemSusChem* 13.8, 2020. DOI: 10.1002/cssc.201903438.

[17] H. L. Wapshott-Stehli et al.: Plasma-driven biocatalysis: In situ hydrogen peroxide production with an atmospheric pressure plasma jet increases the performance of OleT $_{JE}$ when compared to adding the same molar amount of hydrogen peroxide in bolus. *Plasma Processes and Polymers* 19.5, 2022. DOI: 10.1002/ppap.202100160.

[18] B. R. Locke and K.-Y. Shih: Review of the methods to form hydrogen peroxide in electrical discharge plasma with liquid water. *Plasma Sources Science and Technology* 20.3, 2011. DOI: 10.1088/0963-0252/20/3/034006.

[19] C. A. Vasko et al.: Hydrogen Peroxide Production in an Atmospheric Pressure RF Glow Discharge: Comparison of Models and Experiments. *Plasma Chemistry and Plasma Processing* 34.5, 2014. DOI: 10.1007/s11090-014-9559-8.

[20] Y. Du et al.: Effect of water vapor on plasma morphology, OH and H_2O_2 production in He and Ar atmospheric pressure dielectric barrier discharges. *Journal of Physics D: Applied Physics* 50.14, 2017. DOI: 10.1088/1361-6463/aa5e7d.

[21] P. Bruggeman and C. Leys: Non-thermal plasmas in and in contact with liquids. *Journal of Physics D: Applied Physics* 42.5, 2009. DOI: 10.1088/0022-3727/42/5/053001.

[22] G. Goor: "Hydrogen Peroxide: Manufacture and Industrial Use for Production of Organic Chemicals". *Catalytic Oxidations with Hydrogen Peroxide as Oxidant*. Ed. by Giorgio Strukul. Red. by R. Ugo and B. R. James. Vol. 9. Series Title: Catalysis by Metal Complexes. Dordrecht: Springer Netherlands, 1992. DOI: 10.1007/978-94-017-0984-2_2.

[23] P. Anastas and N. Eghbali: Green Chemistry: Principles and Practice. *Chem. Soc. Rev.* 39.1, 2010. DOI: 10.1039/B918763B.

[24] D. X. Liu et al.: Global model of low-temperature atmospheric-pressure He + H_2O plasmas. *Plasma Sources Science and Technology* 19.2, 2010. DOI: 10.1088/0963-0252/19/2/025018.

[25] S. Schröter et al.: Numerical study of the influence of surface reaction probabilities on reactive species in an rf atmospheric pressure plasma containing humidity. *Plasma Physics and Controlled Fusion* 60.1, 2018. DOI: 10.1088/1361-6587/aa8fe9.

[26] J. Winter et al.: Feed gas humidity: a vital parameter affecting a cold atmospheric-pressure plasma jet and plasma-treated human skin cells. *Journal of Physics D: Applied Physics* 46.29, 2013. DOI: 10.1088/0022-3727/46/29/295401.

[27] J. Winter et al.: Tracking plasma generated H_2O_2 from gas into liquid phase and revealing its dominant impact on human skin cells. *Journal of Physics D: Applied Physics* 47.28, 2014. DOI: 10.1088/0022-3727/47/28/285401.

[28] M. M. Hefny et al.: Atmospheric plasma generates oxygen atoms as oxidizing species in aqueous solutions. *Journal of Physics D: Applied Physics* 49.40, 2016. DOI: 10.1088/0022-3727/49/40/404002.

[29] Y. Gorbanev et al.: Combining experimental and modelling approaches to study the sources of reactive species induced in water by the COST RF plasma jet. *Physical Chemistry Chemical Physics* 20.4, 2018. DOI: 10.1039/C7CP07616A.

[30] S. Schröter et al.: Chemical kinetics in an atmospheric pressure helium plasma containing humidity. *Physical Chemistry Chemical Physics* 20.37, 2018. DOI: 10.1039/C8CP02473A.

[31] S. Schröter et al.: The formation of atomic oxygen and hydrogen in atmospheric pressure plasmas containing humidity: picosecond two-photon absorption laser induced fluorescence and numerical simulations. *Plasma Sources Science and Technology* 29.10, 2020. DOI: 10.1088/1361-6595/abab55.

[32] J. Golda et al.: Concepts and characteristics of the 'COST Reference Microplasma Jet'. *Journal of Physics D: Applied Physics* 49.8, 2016. DOI: 10.1088/0022-3727/49/8/084003.

[33] T. Winzer et al.: RF-driven atmospheric-pressure capillary plasma jet in a He/O_2 gas mixture: Multi-diagnostic approach to energy transport. *Journal of Applied Physics* 132.18, 2022. DOI: 10.1063/5.0110252.

[34] E. Jeß: "Diagnostics of Plasma-Produced Hydrogen Peroxide in Liquids". Bachelor's Thesis. Bochum: Ruhr-Universität Bochum, 2022.

[35] S. Schüttler et al.: Validation of in situ diagnostics for the detection of OH and H_2O_2 in liquids treated by a humid atmospheric pressure plasma jet. *Plasma Processes and Polymers*, 2023. DOI: 10.1002/ppap.202300079.

[36] S. Schüttler et al.: Production and transport of plasma-generated hydrogen peroxide from gas to liquid. *submitted in Physical Chemistry Chemical Phyics*, 2023.

[37] L. Boeddinghaus: "Diagnostik der Anregungsdynamik in einem Atmosphärendruckplasmajet mittels phasenaufgelöster optischer Emissionsspektroskopie". Bachelor's Thesis. Bochum: Ruhr-Universität Bochum, 2023.

[38] P. Bruggeman, G. Cunge, and N. Sadeghi: Absolute OH density measurements by broadband UV absorption in diffuse atmospheric-pressure He–-H_2O RF glow discharges. *Plasma Sources Science and Technology* 21.3, 2012. DOI: 10.1088/0963-0252/21/3/035019.

[39] N. Srivastava and C. Wang: Effects of water addition on OH radical generation and plasma properties in an atmospheric argon microwave plasma jet. *Journal of Applied Physics* 110.5, 2011. DOI: 10.1063/1.3632970.

[40] T. Verreycken et al.: Absolute calibration of OH density in a nanosecond pulsed plasma filament in atmospheric pressure He–H2O: comparison of independent calibration methods. *Journal of Physics D: Applied Physics* 46.46, 2013. Publisher: IOP Publishing. DOI: 10.1088/0022-3727/46/46/464004.

[41] J. L. Walsh et al.: Three distinct modes in a cold atmospheric pressure plasma jet. *Journal of Physics D: Applied Physics* 43.7, 2010. DOI: 10.1088/0022-3727/43/7/075201.

[42] Francis F. Chen: "Plasma Applications". F. F. Chen. *Introduction to Plasma Physics and Controlled Fusion*. Cham: Springer International Publishing, 2016. DOI: 10.1007/978-3-319-22309-4_10.

[43] Y. Morabit et al.: Turbulence and entrainment in an atmospheric pressure dielectric barrier plasma jet. *Plasma Processes and Polymers* 17.6, 2020. DOI: 10.1002/ppap.201900217.

[44] J. Golda, J. Held, and V. Schulz-von Der Gathen: Comparison of electron heating and energy loss mechanisms in an RF plasma jet operated in argon and helium. *Plasma Sources Science and Technology* 29.2, 2020. DOI: 10.1088/1361-6595/ab6c81.

[45] V. Schulz-von der Gathen et al.: Spatially resolved diagnostics on a microscale atmospheric pressure plasma jet. *Journal of Physics D: Applied Physics* 41.19, 2008. DOI: 10.1088/0022-3727/41/19/194004.

[46] L. Schaper et al.: Electron Dynamics in a Radio-Frequency-Driven Microatmospheric Pressure Plasma Jet. *IEEE Transactions on Plasma Science* 39.11, 2011. DOI: 10.1109/TPS.2011.2160408.

[47] T. Hemke et al.: Ionization by bulk heating of electrons in capacitive radio frequency atmospheric pressure microplasmas. *Plasma Sources Science and Technology* 22.1, 2012. DOI: 10.1088/0963-0252/22/1/015012.

[48] L. Bischoff et al.: Experimental and computational investigations of electron dynamics in micro atmospheric pressure radio-frequency plasma jets operated in He/N_2 mixtures. *Plasma Sources Science and Technology* 27.12, 2018. DOI: 10.1088/1361-6595/aaf35d.

[49] H. Morgner and A. Niehaus: Experimental and theoretical study of the Penning ionisation of H atoms by He metastables. *Journal of Physics B: Atomic and Molecular Physics* 12.11, 1979. DOI: 10.1088/0022-3700/12/11/008.

[50] M. A. Lieberman and Allan J. Lichtenberg: *Principles of plasma discharges and materials processing*. 2nd ed. OCLC: ocm56752658. Hoboken, N.J: Wiley-Interscience, 2005. 757 pp.

[51] A. Brisset et al.: Chemical kinetics and density measurements of OH in an atmospheric pressure He + O_2 + H_2O radiofrequency plasma. *Journal of Physics D: Applied Physics* 54.28, 2021. DOI: 10.1088/1361-6463/abefec.

[52] U. Fantz: Basics of plasma spectroscopy. *Plasma Sources Science and Technology* 15.4, 2006. DOI: 10.1088/0963-0252/15/4/S01.

[53] P. J. Bruggeman et al.: Gas temperature determination from rotational lines in non-equilibrium plasmas: a review. *Plasma Sources Science and Technology* 23.2, 2014. DOI: 10.1088/0963-0252/23/2/023001.

[54] J. Voráč, L. Kusýn, and P. Synek: Deducing rotational quantum-state distributions from overlapping molecular spectra. *Review of Scientific Instruments* 90.12, 2019. DOI: 10.1063/1.5128455.

[55] S. Hofmann et al.: Power dissipation, gas temperatures and electron densities of cold atmospheric pressure helium and argon RF plasma jets. *Plasma Sources Science and Technology* 20.6, 2011. DOI: 10.1088/0963-0252/20/6/065010.

[56] J. Luque and D.R. Crosley: *LIFBASE: Database and spectral simulation for diatomic molecules*. Version 2.1.1. 1999.

[57] J. Voráč et al.: Batch processing of overlapping molecular spectra as a tool for spatio-temporal diagnostics of power modulated microwave plasma jet. *Plasma Sources Science and Technology* 26.2, 2017. DOI: 10.1088/1361-6595/aa51f0.

[58] J. Voráč et al.: State-by-state emission spectra fitting for non-equilibrium plasmas: OH spectra of surface barrier discharge at argon/water interface. *Journal of Physics D: Applied Physics* 50.29, 2017. DOI: 10.1088/1361-6463/aa7570.

[59] M. Bazavan, M. Teodorescu, and G. Dinescu: Confirmation of OH as good thermometric species for gas temperature determination in an atmospheric pressure argon plasma jet. *Plasma Sources Science and Technology* 26.7, 2017. DOI: 10.1088/1361-6595/aa723c.

[60] I. H. Hutchinson: *Principles of Plasma Diagnostics*. 2nd ed. Cambridge University Press, 2002. DOI: 10.1017/CBO9780511613630.

[61] J. L. Kinsey: Laser-Induced Fluorescence. *Annual Review of Physical Chemistry* 28.1, 1977. DOI: 10.1146/annurev.pc.28.100177.002025.

[62] A. Blohm et al.: "Detection of gas molecules by means of spectrometric and spectroscopic methods". *Advanced Nanostructures for Environmental Health*. Elsevier, 2020. DOI: 10.1016/B978-0-12-815882-1.00006-9.

[63] G. Dilecce et al.: Laser induced fluorescence in atmospheric pressure discharges. *Plasma Sources Science and Technology* 24.3, 2015. DOI: 10.1088/0963-0252/24/3/034007.

[64] B. D. Guenther and D. G. Steel, eds.: *Encyclopedia of modern optics*. Second edition. OCLC: 1027706598. Amsterdam, the Netherlands: Elsevier, 2018.

[65] D. L. Andrews: "Rayleigh Scattering and Raman Effect, Theory". *Encyclopedia of Spectroscopy and Spectrometry*. Elsevier, 2017. DOI: 10.1016/B978-0-12-409547-2.11337-X.

[66] A. Bräuer: *In situ spectroscopic techniques at high pressure*. Supercritical fluid science and technology volume 7. Amsterdam Boston Heidelberg: Elsevier, 2015. 376 pp.

[67] "Quenching of Fluorescence". *Principles of Fluorescence Spectroscopy*. Ed. by Joseph R. Lakowicz. Boston, MA: Springer US, 2006. DOI: 10.1007/978-0-387-46312-4_8.

[68] W. Demtröder: *Atome, Moleküle und Festkörper*. 5., neu bearbeitete und aktualisierte Auflage. Experimentalphysik / Wolfgang Demtröder 3. Berlin Heidelberg: Springer Spektrum, 2016. 586 pp. DOI: 10.1007/978-3-662-49094-5.

[69] John Michael Hollas: *Moderne Methoden der Spektroskopie*. 2. Aufl. Braunschweig: Vieweg, 1995. 403 pp.

[70] G. Gauglitz and David Steven Moore, eds.: *Handbook of spectroscopy*. Second, completely revised and enlarged edition. OCLC: ocn881368785. Weinheim, Germany: Wiley-VCH Verlag GmbH & Co. KGaA, 2014. 4 pp.

[71] J. Held: *mimurrayy/COST-power-monitor: v1.2.1*. Version v1.2.1. 2023. DOI: 10.5281/ZENODO.7812494.

[72] V. A. Godyak and R. B. Piejak: In situ simultaneous radio frequency discharge power measurements. *Journal of Vacuum Science & Technology A: Vacuum, Surfaces, and Films* 8.5, 1990. DOI: 10.1116/1.576457.

[73] P. Bruggeman et al.: Electronic quenching of OH(A) by water in atmospheric pressure plasmas and its influence on the gas temperature determination by OH(A–X) emission. *Plasma Sources Science and Technology* 19.1, 2010. DOI: 10.1088/0963-0252/19/1/015016.

[74] W. P. Partridge and N. M. Laurendeau: Formulation of a dimensionless overlap fraction to account for spectrally distributed interactions in fluorescence studies. *Applied Optics* 34.15, 1995. DOI: 10.1364/AO.34.002645.

[75] N. Sadeghi: 6. Molecular Spectroscopy Techniques Applied for Processing Plasma Diagnostics. *Journal of Plasma and Fusion Research* 80.9, 2004. DOI: 10.1585/jspf.80.767.

[76] V. L. Kasyutich: Pressure broadening parameters of the hydroxyl radical $A^2\Sigma^+(\nu' = 0) \leftarrow X^2\Sigma_{3/2}(\nu = 0)$ transitions at ca. 308 nm. *The European Physical Journal D* 33.1, 2005. DOI: 10.1140/epjd/e2005-00022-0.

[77] P. Pottkämper: "Optische Diagnostik am Hydroxyl Radikal in einem Atmosphärendruckplasma". Master's Thesis. Bochum: TU Dortmund, 2022.

[78] J. Cosimi et al.: Laser-induced fluorescence measurements of spatially resolved OH densities in a helium plasma jet interacting with three different targets in the open air. *Plasma Sources Science and Technology* 32.6, 2023. DOI: 10.1088/1361-6595/acdbe6.

[79] J. T. Salmon and N. M. Laurendeau: Calibration of laser-saturated fluorescence measurements using Rayleigh scattering. *Applied Optics* 24.1, 1985. DOI: 10.1364/AO.24.000065.

[80] T. Verreycken, N. Sadeghi, and P. J. Bruggeman: Time-resolved absolute OH density of a nanosecond pulsed discharge in atmospheric pressure He–H $_2$ O: absolute calibration, collisional quenching and the importance of charged species in OH production. *Plasma Sources Science and Technology* 23.4, 2014. DOI: 10.1088/0963-0252/23/4/045005.

[81] J. Voráč, P. Dvořák, and M. Mrkvičková: "Laser-Induced Fluorescence of Hydroxyl (OH) Radical in Cold Atmospheric Discharges". *Photon Counting - Fundamentals and Applications*. Ed. by N. Britun and A. Nikiforov. InTech, 2018. DOI: 10.5772/intechopen.72274.

[82] T. Verreycken et al.: Absolute OH density measurements in the effluent of a cold atmospheric-pressure Ar–H_2O RF plasma jet in air. *Plasma Sources Science and Technology* 22.5, 2013. DOI: 10.1088/0963-0252/22/5/055014.

[83] Bruker Optik: *Vertex 70 User Manual*. 2013.

[84] I.E. Gordon et al.: The HITRAN2020 molecular spectroscopic database. *Journal of Quantitative Spectroscopy and Radiative Transfer* 277, 2022. DOI: 10.1016/j.jqsrt.2021.107949.

[85] S. Kelly et al.: Gas and heat dynamics of a micro-scaled atmospheric pressure plasma reference jet. *Journal of Physics D: Applied Physics* 48.44, 2015. DOI: 10.1088/0022-3727/48/44/444002.

[86] P. Linstrom: *NIST Chemistry WebBook, NIST Standard Reference Database 69*. 1997. DOI: 10.18434/T4D303.

[87] P. Preissing et al.: Three-dimensional density distributions of NO in the effluent of the COST reference microplasma jet operated in $He/N_2/O_2$. *Plasma Sources Science and Technology* 29.12, 2020. DOI: 10.1088/1361-6595/abbd86.

[88] K. Stapelmann et al.: Following O and OH in He/O_2 and He/H_2O gas mixtures—from the gas phase through the liquid phase to modifications on a biological sample. *Journal of Physics D: Applied Physics* 54.43, 2021. DOI: 10.1088/1361-6463/ac18ec.

[89] S. Yonemori et al.: Measurement of OH density and air–helium mixture ratio in an atmospheric-pressure helium plasma jet. *Journal of Physics D: Applied Physics* 45.22, 2012. DOI: 10.1088/0022-3727/45/22/225202.

[90] S. Reuter et al.: The Influence of Feed Gas Humidity Versus Ambient Humidity on Atmospheric Pressure Plasma Jet-Effluent Chemistry and Skin Cell Viability. *IEEE Transactions on Plasma Science* 43.9, 2015. DOI: 10.1109/TPS.2014.2361921.

[91] P. Bruggeman and D.C. Schram: On OH production in water containing atmospheric pressure plasmas. *Plasma Sources Science and Technology* 19.4, 2010. DOI: 10.1088/0963-0252/19/4/045025.

[92] J. Benedikt et al.: Absolute OH and O radical densities in effluent of a He/H_2O micro-scaled atmospheric pressure plasma jet. *Plasma Sources Science and Technology* 25.4, 2016. DOI: 10.1088/0963-0252/25/4/045013.

[93] S. Schröter: "Reactive oxygen and hydrogen species generation in radio-frequency atmospheric pressure plasmas - Experimental and numerical investigations". PhD thesis. University of York, 2017.

[94] Y. He et al.: Zero-dimensional and pseudo-one-dimensional models of atmospheric-pressure plasma jets in binary and ternary mixtures of oxygen and nitrogen with helium background. *Plasma Sources Science and Technology* 30.10, 2021. DOI: 10.1088/1361-6595/ac278d.

[95] C. Lazzaroni et al.: Analytical–numerical global model of atmospheric-pressure radio-frequency capacitive discharges. *Plasma Sources Science and Technology* 21.3, 2012. DOI: 10.1088/0963-0252/21/3/035013.

[96] G. V. P. Mahreen et al.: Influence of pulse modulation frequency on helium RF atmospheric pressure plasma jet characteristics. *Contributions to Plasma Physics* 62.7, 2022. DOI: 10.1002/ctpp.202200007.

[97] J. Park et al.: An atmospheric pressure plasma source. *Applied Physics Letters* 76.3, 2000. DOI: 10.1063/1.125724.

[98] S. Wang, V. Schulz-von Der Gathen, and H. F. Döbele: Discharge comparison of nonequilibrium atmospheric pressure Ar/O_2 and He/O_2 plasma jets. *Applied Physics Letters* 83.16, 2003. DOI: 10.1063/1.1615674.

[99] W. J. Nuttall, ed.: *The Future of Helium as a natural resource*. 1. iss. in paperb. London New York: Routledge, 2014. 330 pp.

[100] S. T. Anderson: Economics, Helium, and the U.S. Federal Helium Reserve: Summary and Outlook. *Natural Resources Research* 27.4, 2018. DOI: 10.1007/s11053-017-9359-y.

[101] W. J. Nuttall, R. H. Clarke, and B. A. Glowacki: Stop squandering helium. *Nature* 485.7400, 2012. DOI: 10.1038/485573a.

[102] G. Dilecce and S. De Benedictis: Laser diagnostics of high-pressure discharges: laser induced fluorescence detection of OH in He/Ar–H_2O dielectric barrier discharges. *Plasma Physics and Controlled Fusion* 53.12, 2011. DOI: 10.1088/0741-3335/53/12/124006.

[103] S. Yonemori and R. Ono: Flux of OH and O radicals onto a surface by an atmospheric-pressure helium plasma jet measured by laser-induced fluorescence. *Journal of Physics D: Applied Physics* 47.12, 2014. DOI: 10.1088/0022-3727/47/12/125401.

[104] L. R. Williams and D. R. Crosley: Collisional vibrational energy transfer of OH($A^2\Sigma^+, \nu' = 1$). *The Journal of Chemical Physics* 104.17, 1996. DOI: 10.1063/1.471371.

[105] A.E. Bailey et al.: Collisional quenching of OH($A^2\Sigma^+, \nu' = 0$) by H_2O between 211 and 294 K and the development of a unified model for quenching. *Chemical Physics Letters* 302.1, 1999. DOI: 10.1016/S0009-2614(99)00076-7.

[106] R. A. Copeland, M. L. Wise, and D. R. Crosley: Vibrational energy transfer and quenching of OH($A^2\Sigma^+, \nu' = 1$). *The Journal of Physical Chemistry* 92.20, 1988. DOI: 10.1021/j100331a033.

Danksagung

Abschließend möchte ich die Möglichkeit nutzen, meine Dankbarkeit an alle Menschen auszudrücken, die mich auf dem Weg der Erarbeitung und Erstellung dieser Arbeit unterstützt haben. Ein besonderer Dank geht hierbei an

- Jun.-Prof. Dr. Judith Golda, die mir die Möglichkeit gegeben hat, in der AG Plasma Interface Physics zu arbeiten, diese Arbeit zu erstellen und die mir über die Arbeitsphase stets mit einem offenen Ohr zur Seite stand.
- Prof. Dr. Achim von Keudell für die Übernahme der Zweitkorrektur.
- Steffen Schüttler für die Betreuung der Arbeit, die intensive Unterstützung bei der Erstellung und Korrektur sowie wundervolle Büronachbarschaft. Danke, dass du es gewagt hast, die Herausforderung der Betreuung neben der Freundschaft anzunehmen.
- Marina Prenzel, die für mich über die letzen Jahre eine wundervolle Kollegin war und mir unglaublich viele Tage mit langen Gesprächen und kurzen Plauschen versüßt hat.
- Sebastian Burhenn für seine tatkräftige Unterstützung an Laser, Pumpen und LIF-Aufbau und seinen Enthusiasmus für das Thema, der mich immer wieder angesteckt und motiviert hat.
- Alle weiteren Mitarbeiterinnen, Mitarbeiter und Techniker des Lehrstuhls für die Unterstützung und vielen Ratschläge.
- Alexander Lategahn, der mir immer den Rücken freihält, mich bestärkt, meinen Weg zu gehen, und mir das Vertrauen schenkt, jede Situation bewältigen zu können.
- Martina Kai, für die unzähligen aufmunternden Anrufe, ihre immerwährende Fürsorge und tatkräftige kulinarische Versorgung.
  Thomas Frings, für die vielen Stunden der Korrekturarbeit, die Anekdoten zur Aufmunterung und die Bestärkung. Danke, dass ihr mir dieses Studium ermöglicht und alle Wege offengehalten habt.
- Frauke Kai, die mir immer wieder ein Lächeln auf die Lippen zaubert und auf deren Beistand ich mich immer verlassen kann.
- Tim Schwabe und Jan Hendrik Löwer für den Support beim Programmieren und die wundervolle Freundschaft, die nicht nur während dieser Arbeit eine große Kraft- und Motivationsquelle war.